Exploring Phenotypes of a Promising Industrial Methanotroph: An Experimental and Computational Study

by

Kyle Alexander Stone

A dissertation submitted to the Graduate Faculty of
Auburn University
in partial fulfillment of the
requirements for the Degree of
Doctor of Philosophy

Auburn, Alabama
May 5, 2018

Keywords: *Methylomicrobium buryatense*, methane bioconversion, carbon balance, metabolic modeling, phenotypes

Approved by

Jin Wang, Chair, Walt and Virginia Woltosz Endowed Professor of Chemical Engineering
Q. Peter He, Co-chair, Associate Professor of Chemical Engineering
Allan David, John W. Brown Assistant Professor of Chemical Engineering
Bruce Tatarchuk, Charles E. Gavin III Professor of Chemical Engineering
Marina Kalyuzhnaya, Assistant Professor of Biology, San Diego State University

Abstract

Methanotrophs are bacteria that directly convert methane under ambient conditions. In doing so, renewed research interest in their bioconversion capabilities have grown with the current abundance of methane and the global climate impact the gas has. Of the many different strains of methanotrophs, *Methylomicrobium buryatense* 5GB1 has gathered recent attention as a haloalkaliphilic strain that grows rapidly in medium that is naturally selective. Despite this peak in scientific study with methanotrophs and 5GB1, many unknowns remain. Specifically, this study strives to systematically investigate: (1) The effect of methane and oxygen concentrations on the growth rates and carbon distribution in small batch cultures; (2) Experimentally evaluate the effect of carbon distribution and growth on an “oxygen deprived” and “methane deprived” headspace with different dilution rates; (3) Conduct *in silico* analysis with experimental results to evaluate energy requirements and overall predictive performance with a constrained reduced genome scale metabolic model.

From this work, creative, analytical methods and careful control procedures allowed for quantification of carbon distribution in under-pressurized vials or in continuous benchtop chemostats. With accurate experimental data, an initial phenotype characterization brings forth new insights on metabolic shifts within cells and raises fundamental biological questions during substrate deprived states. Overall, this study contributes to the necessary knowledge base to design processes for improved conversions with this promising biocatalyst.

Acknowledgments

First and foremost, I would like to express my deepest gratitude to Dr. Jin Wang for her support, guidance, patience, and dedication throughout this whole project. Thank you to my co-advisor Dr. Qinghua (Peter) He for his time and effort in providing sound advice and discussions. I would like to give a special thank you to Dr. Marina Kalyzuhnaya, Dr. Mary Lidstrom, and both of their groups for answering all my questions for methanotrophs. Also thank you to my other committee members Dr. Allan David, Dr. Bruce Tatarchuk, and Dr. Yi Wang for their assistance in completing this work. Thank you to the countless scientists and students, who shoulders I stand on while I completed this project.

My group members (past and current) have been incredible to me and I greatly appreciate all our conversations (even if they weren't work related). I would like to give a special thanks to Dr. Min Hea Kim who gave day to day advice on anything and everything I asked about. Simply put, I could not have done this without her assistance and guidance. I would also to thank my friends and family who made sure that I was social, regardless of how much I didn't want to be. This special group of people always helped me cope when the going got tough. Thank you guys.

I would like to thank my parents, Melissa Whittier and Kenneth Stone, for their immeasurable support throughout my time at Auburn. Their ability to listen to all my thoughts, doubts, complaints, and aspirations is an accomplishment in itself. A special thank you goes to Kasaundra and Kayla Stone for their love and support. Our time together is what I hold near and dear to my heart. I cannot thank you enough for all the treasured memories I have. My drive and strength to continue on through challenging days come from Beatrice Hebert. I love you now and forever Nana. Finally, all the hope that I ingrained in this work for a more sustainable and healthier planet is dedicated to my baby niece, Olivia Rose Pabon. I love you and will always try to make this world a better place for your future.

Table of Contents

List of Tables

List of Figures

Chapter 1 : Introduction to Bioconversion of Methane and Process Considerations

1.1 Methane: An Abundant Carbon Source and Prominent Greenhouse Gas

Methane is an abundant organic gas that is considered a rich source of carbon and energy. There are two main sources of methane: non-renewable natural gas and renewable biogas. For natural gas, which contains ~80%-95% CH_4, there is 6800 trillion cubic feet of proven reserves globally recorded, of which the US has claims to 2,355 trillion cubic feet. Additionally, elevated levels of natural gas production in the U.S. is expected to continue based on datasets from the U.S. Energy Information Administration (EIA) (see Figure 1) [1,2].

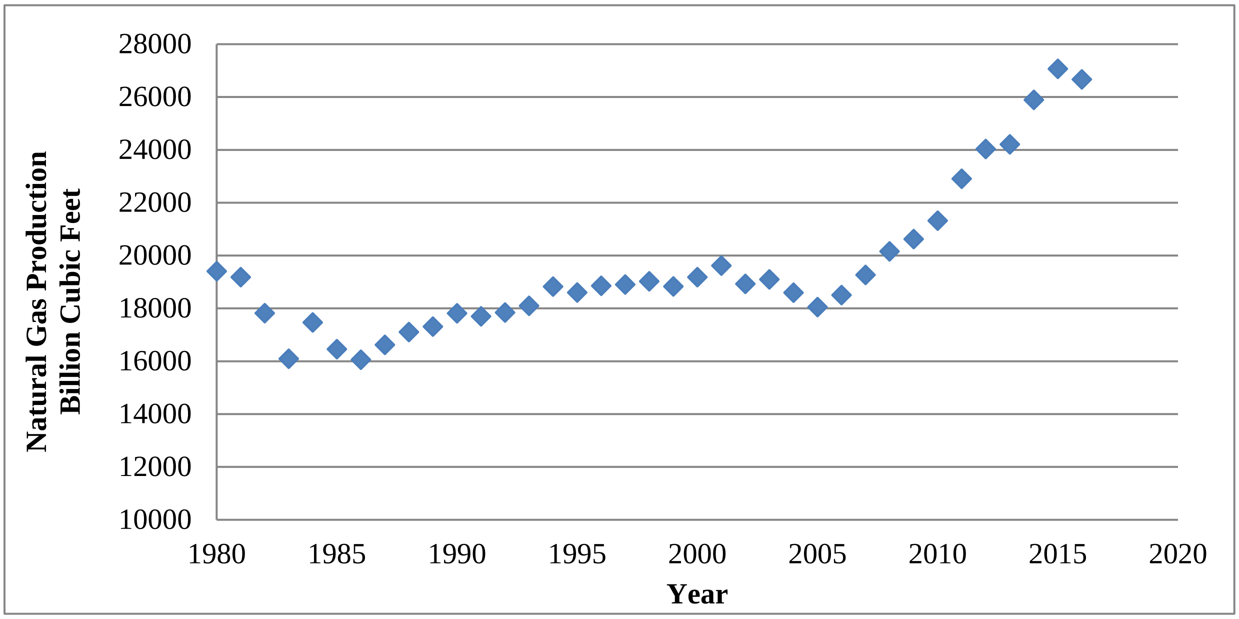

Figure 1: U.S. dry natural gas production

On the other hand, biogas, which contains ~50%-70% CH_4 and ~30%-40% CO_2, is generated rapidly from anaerobic digestion of organic matter. The primary sources for digestion are livestock manure, food waste, landfill gas, water treatment facilities, and food production residuals. Collectively, these numerous sources could provide 41 billion kWh/ year of electricity that would satisfactorily power more than 3 million U.S. homes for one year or produce the equivalent of 2.5 billion gallons of gasoline for vehicles. Similarly, captured biogas could feed into bioprocesses to make additional substantial energy and bio-based products. Of the possible 13,000 sites in the U.S., only about 2,000 are operational and thus, providing untapped potential for sustainable processes. [3].

With clear abundance for both sources, common processes regularly release methane into the atmosphere via ventilation or flaring when the sources cannot be completely converted due to technical or economic limitations. If released in the atmosphere, methane will add to the climate change effect currently observed. Methane is the second most abundant greenhouse gas (behind CO_2) with a global warming potential that is >25 times that of CO_2 in a 100-year period [4]. Specifically, over 100 billion cubic feet of natural gas is vented or flared per year since 2006 (see Figure 2) [5]. Meanwhile, any unused biogas sites simply ventilate effluent streams to the atmosphere. Additionally, more than half of the anthropogenic methane emissions are below 3% in concentration that leads to unfavorable economic conditions for most chemical conversion technologies. These diluted emissions come from old landfills, coal mines, or liquid manure storage areas [6].

Hence new technology to directly convert methane is highly sought after. Ideally the system must be able to balance challenges associated with the methane source (e.g. presence of nitrate and sulfate based contaminants), while also increasing conversion rates or selectivity in an effort to reduce methane emissions.

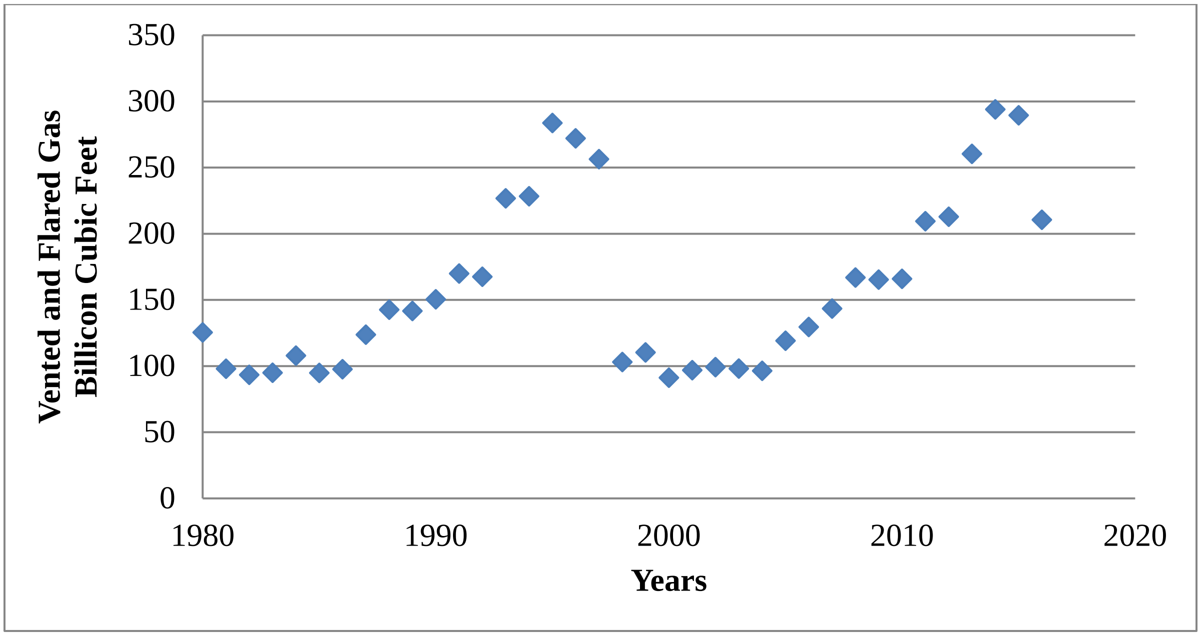

Figure 2: U.S. vented and flared natural gas

1.2 Brief Introduction to Methanotrophs

Over the past 30 years methanotrophs have moved from a “black box” organism to being on the cusp of becoming the next biocatalyst in a promising biotechnical world. To quickly summarize, methanotrophs are bacteria that assimilate methane (largely through aerobic processes) for their sole source of carbon and energy. Publications on methanotrophs have grown significantly in the recent decades [7] with topics covering natural history [8,9], ecology [9–12], medium preparation [13,14], molecular biochemistry [8,9,11,12,15–19], metabolic engineering [20], and the application of methanotrophs for bioremediation [21,22], fuels, and valuable chemicals [14,15,23–27]. As a result, methanotrophs have started to gain a foothold in bioindustries with great progress seen in aquaculture and energy production [24]. However, their industrial applications and developments are limited compared to the conversion of biomass to ethanol through industrial microorganisms [28].

The oxidation of methane to methanol is the first step in carbon assimilation and is completed with the particulate and/or soluble form of methane monooxygenase (MMO) in an environmentally benign fashion [11,17,19]. The equation for this reaction is shown below.

$$CH_4 + O_2 + 2e^- + 2H^+ \rightarrow CH_3OH + H_2O \qquad \textbf{(1)}$$

The soluble form, sMMO, is found in the cytoplasm of the cell and is associated with a large substrate range including1-8 carbon chained alkanes, cyclic alkanes, and aromatic hydrocarbons [11]. Electrons for methane oxidation by sMMO would be provided by intracellular NADH. The particulate form, pMMO, is found on intracytoplasmic membranes (ICMs) and has a far narrower range of substrates. These ICMs are of growing interest because they are composed of fatty acids that could potentially be used to create biodiesel [29]. Elections could be provided to the particulate form, pMMO, by a number of ways and is discussed in detail in later sections [20]. Several excellent reviews of the MMOs have been published [8,9,11,15,16,30] and additional details regarding their structure and kinetics are covered elsewhere [11,31].   Table 1 lists the basic properties of the two types of MMOs [8,10,11,16,22,31].

	pMMO	sMMO
Location	Inner Membrane Bound	Cytoplasm
Specific Activity	Low K_m (8.3-92 µM)	High K_m (92 µM)
Substrate Specificity	Alkanes and alkenes (C1-C5), chlorinated aliphatics, and ammonia	Aromatics, heterocyclics, alicyclics, alkanes and alkenes (C1-C8), ethers, halogenated aliphatics,

		chlorinated aliphatics, carbon monoxide, and ammonia
Electron Donor	Not clear	NADH
Active site cofactor	Iron	Copper

Table 1: Comparison of pMMO and sMMO properties

Methanotrophs that possess genes for both enzymes, regulate their expression by a “copper switch”. At higher copper concentrations, the pMMO is upregulated and becomes the predominant methane oxidizer. The regulation and transcriptomics of this copper switch is an active area of research and is again, covered elsewhere [32–35].

Methanol created by the MMO is then directed towards two main metabolic routes. The first entails further oxidation of methanol to regenerate the reducing power required for methane conversion via MMO (see Figure 3). The other pathway, assembles the molecule into process that create multi-carbon building blocks used to make lipids, proteins, and nucleic acids. How the carbon is assimilated in aerobic organisms defines the groups their organized by. For example, Type I organisms use the RuMP cycle and Type II utilizes the serine cycle. A third type, type X utilizes a combination of both assimilation routes with the CBB cycle [8]. In this work, the central carbon network is of main interest. This reduced network pays strictly attention to the basic metabolism (i.e. EMP, TCA cycle, RuMP cycle, etc.) of the organism, *Methylomicrobium buryatense* 5GB1. Specifics of the metabolic model and biochemistry involved are covered in later sections.

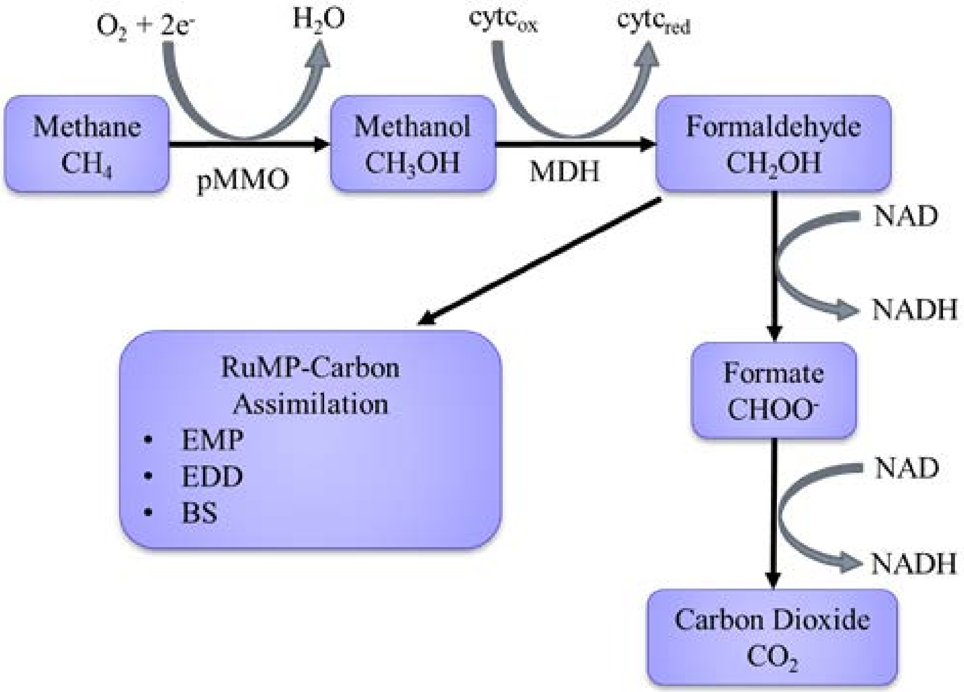

Figure 3: General biochemistry of methanotrophs. pMMO is particulate methane monooxygenase and MDH is methanol dehydrogenase. [36]

1.3 Examples of Methanotrophs as a Biocatalyst for Fuels and Chemicals

In recent years, methanotrophs have gained considerable attention as biocatalysts for processes that create biomass, fuels and chemicals [7,23,24]. For fuels, methanol and biodiesel are of interest capitalizing on the central carbon network and generation of intercellular membranes. Meanwhile for chemical production, PHB, ectoine, and lactate are making headway as components that naturally accumulate under controlled stress conditions.

Among various products, single cell protein (SCP) is the closest example of commercially successful methanotroph-based biotechnology. For example, Norferm Danmarks A/S, reportedly could produce 8000 tons per year of BioProtein and had potential to significantly increase to

40,000 tons per year [11]. The company was latter bought out by Calysta who rebranded the process to make FeedKind™ protein [37]. Calysta has since sought further application of methanotrophs technology in the aqua/mariculture and livestock feed industries. The protein has been approved recently by the European Union for use in nutritional feeds for salmon and livestock (e.g. pigs, poultry and cattle).

In the past few years, the U.S. government has devoted millions of dollars into research that utilizes methanotrophs to make liquid fuels through the Advanced Research Projects Agency-Energy [14]. One topic of interest is biodiesel production from the lipid content of the cells, especially from the ICMs when pMMO is expressed. The fatty acids in lipids accumulated by methanotrophs are usually saturated or mono-unsaturated C14-C18 chain lengths, which are considered ideal for diesel production [14]. However, many of the lipids associated with methanotrophs are phospholipids which can be problematic for upgrading hydrocarbons. NREL has worked towards alleviating this challenge and developed a two-stage pretreatment method followed by hexane extraction with upgrading of lipids through advanced catalyst design. In doing so, lipid conversion was in excess of 99% with the final hydrocarbon mixture dominated by 88% pentadecane [29]. To be competitive with other biofuel production, high lipid content of about 35% from engineered strains would be a key target [14]. Currently with the use of *Methylomicrobium buryatense* 5GB1, the lipid content ranges between 9-11%, indicating more genetic work is needed to reach this goal [38].

Methanol is another fuel of interest because it is far simpler to transport and handle compared to methane. It would especially be lucrative if methanotrophs can convert methane directly to methanol in an ambient one-step process, a feat that currently utilizes much harsher conditions in a chemical conversion systems [27]. This bioprocess is usually accomplished via inhibition of the second enzyme in the biological pathway, MDH that allows for an accumulation of methanol (see Figure 3). Commonly used MDH inhibitors include concentrated phosphate, cyclopropanol, NaCl, NH_4Cl, chelating agents, and CO_2. However, when inhibiting an important part of the central carbon pathway, cell growth and methane oxidation pattern are affected due to the loss of reducing power usually generated via downstream oxidation of methanol. Current solutions include the addition of formate to the system to regenerate this lost source of electrons, but the cost for this ingredient is economically challenging [27]. The production capabilities of methanotrophs vary drastically pending on the chemical agent of inhibition and the specific strain. It is worth noting that because most MDH inhibitors also partially inhibit pMMO activity, overly high concentration of MDH inhibitors usually results in reduced methanol production [27,39–46]. The reported range alter in between 0.0006-1.12 g/L of methanol concentration, where higher ends prove toxic to the cells [27]. Despite these challenges, methanol production from methanotrophs is an active area of current research with different substrates, reactors, and consortiums being considered [27,47–49].

Poly-β-hydroxybutyrate (PHB) is a polyester of butyric acid with similar tensile and thermal properties to industrial plastics such as polypropylene and polyethylene [50–52]. PHB serves as storage of excess carbon that exists in cells as distinct inclusions or granules [53,54]. Being biodegradable, PHB has found use in many industries including medicine, food packaging, and agriculture [55–57]. Limiting factors that could trigger PHB accumulation in methanotrophs include both macrocomponents, such as phosphorous or nitrogen, and microcomponents, such as magnesium, potassium, copper, or cobalt [57–60]. Only Type II methanotrophs have the ability to build PHB as they solely express the complete genetic code for polymer synthesis [61]. PHB production with methanotrophs is often carried out in a two-stage process: the first stage is a continuous/batch growth phase that maximizes cell density; the second stage is a batch PHB production phase where cells are introduced to medium with limited nutrients (usually nitrogen) to initiate PHB polymerization [57,62] . For methanotrophs, PHB can make up anywhere from 10-68% of cellular biomass and lead to a concentrations as high as 30 g/L [50,52,58,62]. Advancements to increase yields and economic feasibility are still being sought after as research for biodegradable plastic production with methane abatement [63–65] .

In 2013, it was discovered that methanotrophs could use their metabolic pathways to channel assimilated carbon to formate, lactate, and acetate under oxygen limitation conditions [66]. The production of these acids was small (in µmol gDCW^{-1}), but remain an important metabolic finding as this proves that methanotrophs can undergo a fermentation mode. Of these acids, lactate is of key interest as it serves as a precursor to biodegradable polylactide (PLA) polymer for plastics. Utilizing new genetic engineering tools, a team at NREL modified the strain *Methylomicrobium buryatense,* so it could produce 0.8 g/L of lactate which was a 13 fold improvement compared to the wild strain [67]. Such work encourages further genetic modification, while also potentially providing another source of revenue with methanotroph bioprocess.

Ectoine is a cyclic amino acid that acts as a microbial osmo-protectant against osmotic dehydration and thus, is another compound of interest for methane bioconversion technologies. Under high salinity stress, accumulation of ectoine can reduce loss of water and adjust the turgor of the cells without negatively impacting cellular metabolism. As a result, ectoine is a highly valuable compound ($1300/kg), and has found uses in biotechnology, cosmetics, and medicine as a multifunctional bioprotectant [26,68,69]. Production is often considered a two-stage process where one stage promotes growth, while the other generates ectoine excretion via hypoosmotic shock by adjusting the salinity in the liquid medium [70]. Though ectoine production from various methanotroph strains have been known for years, research into process design and production rates are still in its infancy [70–72].

1.4 Process Considerations for Bioconversion of Methane

Challenges in process design for bioconversion of methane have been reviewed intensively in the last few years [14,24,73,74]. At the heart of these challenges lie the inefficient transfer of the insoluble gas substrates, methane and oxygen. To deal with this fundamental obstacle, reactor design and the use of promoting agents must be considered carefully. Evaluation of transfer is further complicated by the costly direct measurement of dissolved methane.

The mass transfer rate of gasses is usually characterized by the volumetric mass transfer coefficient, k_La, of the substrate. In this short review, k_La is used as one of the major metrics to evaluate the performance of different bioreactor configurations and mass transfer enhancement approaches. However, it is worth noting that k_La is not a direct measure of a process performance. In addition, it is highly sensitive to cell density and broth properties [75].

Among the many approaches to measure k_La, the most common, such as dynamic method and its variations, require the measurement of dissolved gas concentration. For methanotrophs this would require the measurement of both dissolved oxygen and dissolved methane. Dissolved oxygen probes are commonly used and are commercially available; however, very few probes for measuring dissolved methane are as feasible. In fact, much of the dissolved methane sensor technology has been developed for geochemical studies and can be prohibitively expensive [76].

To address this challenge, a couple of in-house developed methane probes with permeable membranes have been reported [77,78]. Another approach strips the dissolved components in the liquid into the gas phase to establish equilibrium and apply Henry's Law for proper quantification. The gas phase methane concentration can be measured through methane detectors or standard analytical techniques such as gas chromatography [79].

Besides these approaches, the k_La of methane can also be estimated through the k_La of oxygen. For the applications of methane bioconversion, since the gas phase consists of mixed methane and oxygen, both gases share the same specific interfacial area and their volumetric mass transfer coefficients are only differentiated by their corresponding mass transfer coefficient k_L. Both the penetration theory and the surface renewal theory of mass transfer suggest a linear relationship between the gas component's mass transfer coefficient, k_L, and the square root of its diffusion coefficient, D [80]. For methane and oxygen, their diffusion coefficients are 1.49×10^{-5} cm^2/s and 2.1×10^{-5} cm^2/s [80], respectively, which suggests that $k_La_{CH4} = 0.842\ k_La_{O2}$. This relationship is similar to what Yu et al. [81] have reported: $k_La_{CH4} = 0.855 k_La_{O2}$. Because dissolved oxygen probes are widely available, using the measured k_La of oxygen to estimate the k_La of methane creates an easy way to quantify the mass transfer rate of methane from gas to liquid for bioconversion applications.

Bioreactor configurations are dependent on the concentration of the gas feed, whether methane is in high concentration, such as natural gas or biogas, or diluted within in waste stream such as with old landfills or coal ventilation streams [73]. For high concentrations the tubular loop reactor (e.g. U-loop, vertical or horizontal loop) is of particular interest because of long gas residence times and break up of bubbles via static mixers [73]. In this work and in many others, a stir tank reactor was used where broth and cells are mechanically agitated by an impeller while gas substrate is fed through a sparger located at the bottom of the reactor. For this configuration, over-agitation could cause negative effects on gas transfer, because of poor dispersal of bubbles and multiple collisions leading to larger bubbles inhibiting gas transfer [73]. This is illustrated in

Figure 4 below, where oxygen transfer was tested with three different spargers at various agitation speeds in typical NMS medium.

For more diluted influents, such as those with less than 3% methane, the biofilters and biotrickle filters are used primarily for gas abatement. Biotrickle filters (BTFs) are similar to conventional biofilters in the sense that they contain solid packing material, although cells can be immobilized or free floating. The key difference is that in BTFs the liquid phase is continuously pumped to the top of the reactor and allowed to trickle down over the solid packing. This characteristic contributes to higher methane removal efficiency in BTFs on average for similar residence times. BTFs have been used for methane abatement with removal efficiencies as high as 78% [6,82–84]. Further comparison for both concentrated and diluted feeds with other reactors is covered elsewhere [73,85].

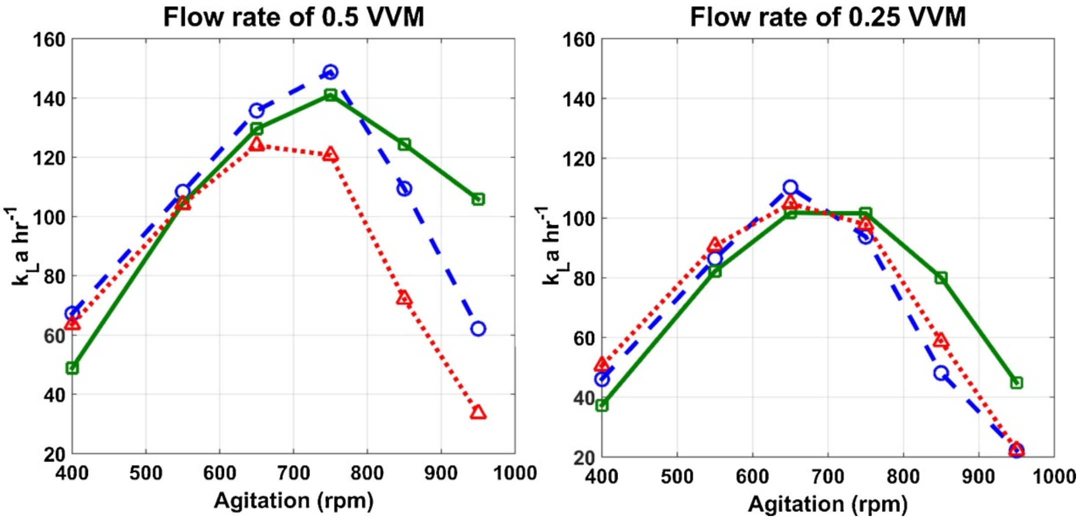

Figure 4: Evaluation of k_La with different agitation speeds and sparger types**.** Green solid line with squares: the conventional stainless steel sparger equipped in Eppendorf Bioflo 115 reactors; Blue dashed line with circles: Alita's silicone tube punctured throughout with 1 mm slits; Red dotted line with triangles: Eppendorf microsparger.

In addition to research on reactor design, studies have been conducted on the use of promoting agents with higher affinity to methane and oxygen to enhance mass transfer. Examples of these components include vectors and polymers (covered below), while less utilized nanoparticles, electrolytes, and non-ionic surfactants are being evaluated

Vectors are non-aqueous, non-toxic, non-volatile, and non-biodegradable organic phases added to the fermentation broth that can induce significant increases in gas to liquid mass transfer [86–89]. In some cases the k_La experienced increases over 90% [90] and between 31-72% increase in methane removal rates [91]. Polymer particles with high affinity and specificity towards gases can be used as solid vectors. These polymers are non-biodegradable, inexpensive (unlike their liquid vector counterparts), and can be tailored on shape, size, and gas target [92]. Also, studies have demonstrated that polymers can be specifically designed so that little to no cell adhesion would occur that reduces cellular loss while simultaneously recovering the polymers themselves [93]. It has been suggested that the increased specific interfacial area observed by bubble distribution caused by the addition of polymer, is the most influential factor for the mass transfer enhancement [94–96]. Oxygen transfer rate with the addition of polymers has been shown to increase from anywhere between 20-255% [88].

The addition of nanoparticles, electrolytes, and non-ionic surfactants are less utilized than the previous agents. However, they do enhance gas transfer and consumption rates via stabilization of bubbles due to repulsion or hydrophobic/hydrophilic properties. Additionally there is a lack of studies with the use of these agents with biomass and challenges remain on how separation of the agents from products could occur with downstream process [73].

1.5 Safety Concerns with Bioconversion of Methane

Methane is a highly flammable gas and with the right amount of oxygen it can easily create an explosive mixture. Therefore, the bioconversion of methane via methanotrophs poses serious safety concerns that must be addressed. The combustible range of methane/air mixtures is 5–15% volume of methane. Although most methane fermentation process are outside of this range, the following safety considerations and practices are very important to ensure the safety of operation. The reactor should be designed in a manner that prevents the accumulation of un-utilized substrate gases [14]. This can be achieved via gas recycling [6,90], full utilization of substrate gas [91], as well as proper venting. This also stresses the need for in-line measurement of oxygen and methane in the reactor [97].

For lab scale methanotroph fermentations, four safety practices are recommended ([98] and personal communications with Dr. Mary Lidstrom, University of Washington and Dr. Christopher Roberts, Auburn University). 1) Proper gas ventilation of any unused/non-recycled methane and oxygen by placing the fermentation system in a fume hood or under proper metal snorkel tubes, so effluent gases can be removed safely. 2) A fail-safe, auto shut off gas system should be implemented to handle possible exhaust failure or gas leaks. The system should consist of a flammable gas detector with a relay that is connected to electronic mass flow controllers and solenoid valves in the gas lines. If the power fails or if there is a detectable flammable gas, the system will automatically shut off the flow controllers and valves. 3) Static mixers should be utilized to mix methane and oxygen to avoid any frictional discharge. 4) Finally, both the equipment system and the researchers should be properly grounded. This can be achieved by using an anti-static mat for the equipment system and having the researcher wear an anti-static wrist band.

1.6 Objectives of this Study

With increasing interest in methane bioconversion for abatement and production processes, a growing need for research on phenotype behavior is required. Thus, the overall objective of this study is to characterize the various phenotypes of a promising methanotroph *Methylomicrobium buryatense* 5GB1 via experimental and computational means. Specifically, the following content focuses on:

1) Systematically investigating the effect of methane and oxygen concentrations on the growth rates and carbon distribution in small batch cultures.

2) Evaluating the effect of carbon distribution and growth as measurable physical responses to an “oxygen deprived” and “methane deprived” headspace with different dilution rates in a continuous chemostat.

3) Performing *in silico* analysis with the results from objective 2 to evaluate the intercellular network pathways and their accompanying ATP requirements within a constrained reduced genome scale metabolic model.

Chapter 2 : Introduction to Genome Scale Metabolic Modeling and Tools

2.1 Genome Scale Metabolic Models, Flux Balance Analysis, and Phenotype Phase Plane Analysis

With continuous progress of omics technology, mathematical model representations of cellular metabolisms have grown in complexity and popularity. In doing so, *in silico* experimentation can provide insight on the effects of designed mutation and synthetic carbon flux through the metabolic network These models are called genome scale metabolic models (GEMs) which as the name suggests, are constructed based from the cell's genome to provide a map of the possible enzymes and their corresponding reaction pathways. As such, these models build a bridge to relate organism's genotype and phenotype by incorporating genomics and experimentally observed data into model building and establishing constraints [99,100].

Specifically, GEMS enable researchers to examine how a system (i.e., cellular metabolism) comprised of many individual components (i.e. reactions) interact to achieve a common objective. Models are created via a system of equations in a stoichiometric matrix that represents the reactions and metabolites that comprise an organism's metabolism via knowledge of the annotated genome. The rows represent the reaction taking place and the columns represent the metabolites in the model. Each entry represents the stoichiometric coefficient of each metabolite. A negative entry accounts for metabolite consumption and a positive entry for metabolite production in all reactions. Metabolites that are not involved in the reaction simply receive a zero value. Since the matrix developed is based from the complete stoichiometry of reactions, it is inherently mass balanced at steady state. It is important to note that most genome sequences are only partially characterized; therefore, modifications are made for improvement [99].

Models consist of hundreds or even thousands of reactions and metabolite. Universally, reactions far outnumber the metabolites in GEMs creating a stoichiometric matrix in the model that in turn, generates an underdetermined system of equations. Therefore, the most common technique for quantitative evaluation of GEMs is through constraint based optimization. These constraints may be physicochemical, environmental, thermodynamic, or experimentally derived so that the solution space is logically reduced [101].

There are many ways to solve this underdetermined system of equations. For this research, flux balance analysis (FBA) is used. FBA is a powerful technique that treats the complex cellular metabolism as a linear programming problem. An objective function is defined and is used to calculate an optimal solution[102]. In this study, the objective function is set to maximize the predicted growth rate of the methanotroph. Reversibility data for reactions are used for the lower and upper bounds to constrain the possible reaction fluxes through each pathway and evaluated to achieve the objective function (e.g. maximize growth). Constraints commonly applied to the model are uptake rates of the substrates and production rates from extracellular metabolites. For model analysis, methane and oxygen are the substrates, while formate or carbon dioxide could be constrained for production rates if desired.

It is important to note that FBA does not require kinetic parameters, but uses defined constraints based on mass balances and bounds set by experimental data. This method does not incorporate regulatory effects of genes or enzyme activity [103]. Since FBA is a steady state approached, it only uses time-invariant substrate (mmol g DCW^{-1} hr^{-1}) consumption rates and thus, used for predictions from continuous experiments.

A basic overview of GEMs and the FBA process is shown in Figure 5 [104]. Using the genome model to understand the placement and stoichiometry of known reactions, a stoichiometric matrix, S, can be produced. For example, the first reaction is the consumption of metabolite A to metabolite B. Thus, reaction (rxn 1) will have a value of -1 for the consumption of A in the S table and a value of +1 for production of B. From this table, the concentration flux (dx/dt) over time is defined. FBA's key steady state assumption removes the derivative term and leaves Sv =0. The v matrix is the fluxes of individual reactions and is what is being solved by FBA. Using define bounds (α and β) of the metabolites and substrates, an optimal solution is found for the defined objective function (often the flux through the biomass equation called the growth rate).

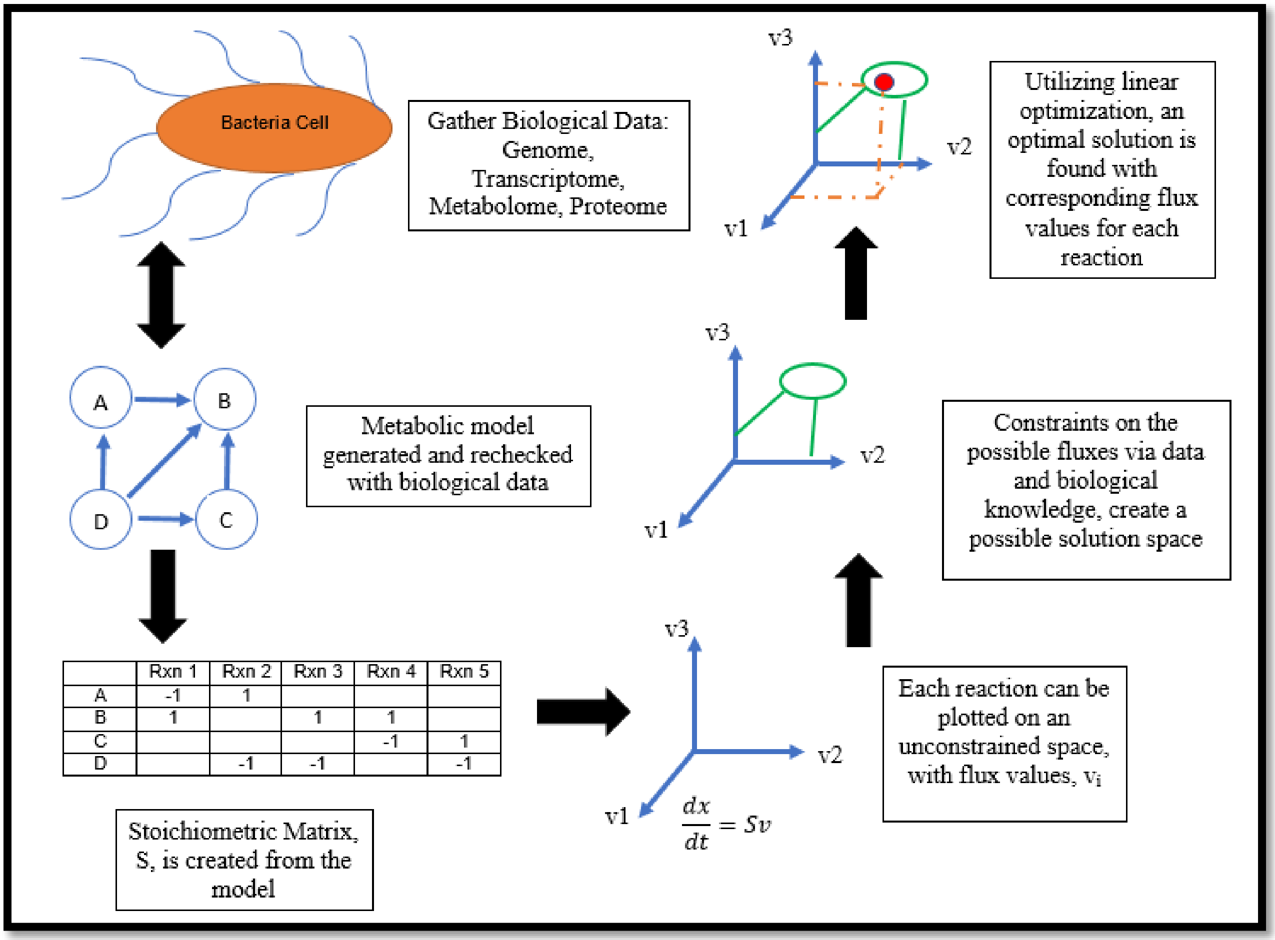

	Rxn 1	Rxn 2	Rxn 3	Rxn 4	Rxn 5
A	-1	1			
B	1		1	1	
C				-1	1
D		-1	-1		-1

Figure 5: Summary of genome metabolic models and flux balance analysis. This was adapted from [104].

A complete phenotype phase plane (PhPP) can be created *in silico* with over a hundred step changes of substrate (oxygen, carbon, or both), as illustrated in Figure 6. Each change perturbs the system and the reaction fluxes evaluated via FBA. The corresponding results of each perturbation can be compared to see if the change lies within the same phenotype plane. For physical experiments, phenotypes are characterized by carbon distribution, pickup and production rates. For *in silico* experimentation, the phenotype is characterized by the shadow price as calculated by FBA. The shadow price is defined as the effect of the metabolite concentration on the objective function. Thus, in each phenotype plane, each metabolite is supposed to contribute the same way to the objective function. In addition to traditional PhPP, a systems identification enhanced phenotype phase plane analysis (SID-PhPP) was developed which utilizes multivariate analysis, more specifically principal component analysis (PCA), to identify phenotype phases. PCA and SID-PhPP is described in further detail elsewhere [104,105] Figure 6 consists of a 3D plot of the exchange reactions of methane and oxygen uptake to predicted growth rate. The line of optimality is shown in black, while the different colors distinguish the other phenotype planes. The 3D plot can then be summarized into a 2D plot where the expected methane and oxygen uptake display again, the phases and the line of optimality.

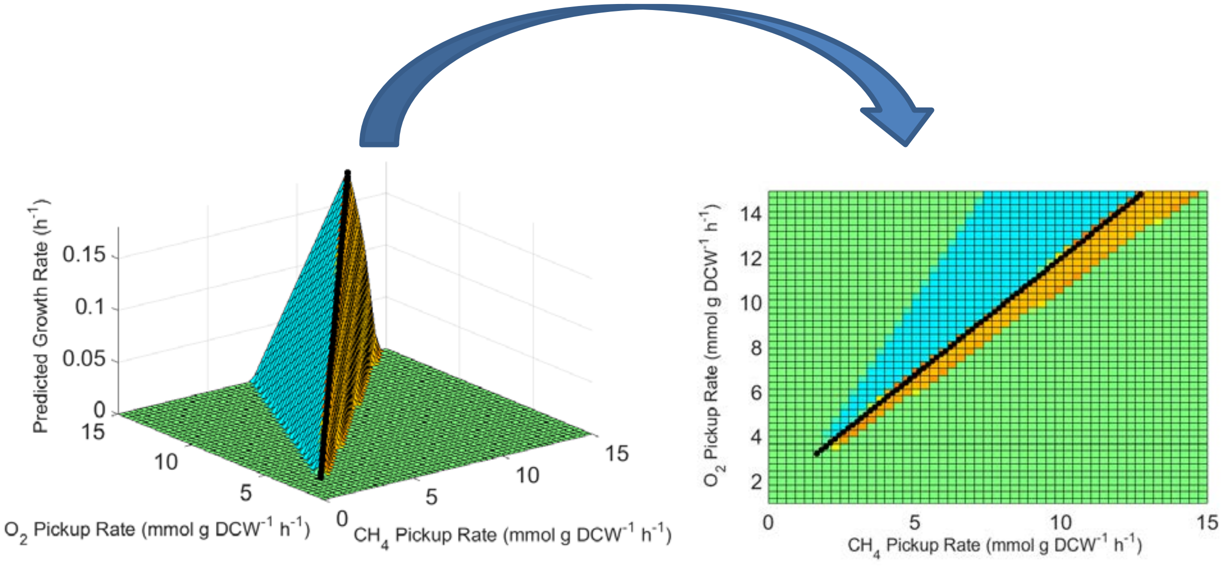

Figure 6: 3D and 2D plots of the different phenotypes for *M. buryatense 5GB1*

2.2 Current Models for *Methylomicrobium buryatense* 5GB1

In 2015, a full metabolic model from the genome of 5GB1 was reconstructed [106]. The composition of the biomass flux (which represents growth rate) was designed from direct measurement of metabolites (i.e. amino acids, fatty acids, phospholipids, etc.), primary literature, and assumed values from well-studied organisms including *M. alcaliphilum* 20z and *E. coli.* The stoichiometric matrix for the model was further reduced by efforts of Dr. Marina Kalyuzhnaya's group, removing futile cycles and non- expressed reactions. This simplified model was kindly provided for the completion of this work. It is important to note for the research of this project, the initial model is referred to as the "full model", while the trimmed down model is referred to as the "reduced model".

For both models a few key assumptions and summarizations are made. The first is the grouping of the reactions involved in the electron transport chain where the cells produced the energetic unit ATP via aerobic respiration. Instead of accounting for the hydrogens pumped across the intercellular membranes for ATP generation, the overall reactions are summarized below assuming oxygen as the electron acceptor and NADH as the main electron donor.

$$2NADH/H^{+} + O_2 + 6\,ADP + 6\,Pi + 8\,H^{+} \leftrightarrow 2\,NAD + 8H_2O + 6\,ATP \qquad \textbf{(2)}$$

The general equation for ETC above has been further broken down to the individual complexes [107,108]. The number of hydrogen ions pumped by these enzymes is of interest and thus are labeled specifically in these models. These labeled hydrogen ions are then used by the ATP synthase with a set ratio of hydrogen to ATP production. The process is called oxidative phosphorylation and it is assumed that 1 ATP is produced per 3 H+ ions translocated across the membrane. For this particular study, the summarized form is maintained but this assumed ratio of ATP/H pumped is of interest, as discussed in later sections.

It is also important to note that the above equation assumes a 3 mol ATP per 1 mol NADH yield. In other cases, 2.7 and 2.5 ATP/NADH yield is plausible, but not considered for this study as these yields suggest an inefficient transport chain not traditionally observed with this methanotroph [106]. The produced ATP can be used for metabolic reactions, non-growth associated maintenance, and growth associated maintenance. Non-growth associated maintenance is typical energy requirements by the cells to stay viable but is separate from the energy needed for reproduction. Growth associated maintenance is the energy utilized for cell duplication and growing biomass. In the model, non-growth associated maintenance is accounted for via a reaction directing ATP to ADP at an initially assumed flux of 8.39 mmol ATP $gDCW^{-1}$ h^{-1}, while growth associated maintenance was set via as a coefficient in the biomass flux at a “low”, “normal”, or “high” setting which were 23, 54, and 59.81 mmol ATP $gDCW^{-1}$.

Furthermore, formate, acetate, and lactate are removed from the biomass equation. Formate and acetate have especially been known to be produced by 5GB1 under both methane and oxygen limited conditions [36,67]. However, the production in this particular methanotroph is not solely owed to a “fermentation mode” as seen in the fellow methanotroph strain, *Methylomicrobium alcaliphilum* 20z [66]. Recent research indicates a redox balance and nutrient limitation (nitrate and trace elements such as copper) may play a larger role [32].

2.3 Electron Pathways and Energy Usage in Metabolic Modeling of *M. buryatense* 5GB1

Despite the high quality of research that has elucidated the metabolism of methanotrophs over the past 30 years, the electron donor to the main enzyme pMMO remains elusive. However, three main mechanisms have been proposed and evaluated with both experimental and computational studies with the closely related, *M. alcaliphilum* 20Z strain [106,108]. The three mechanisms currently considered include re-dox arm, direct coupling, and uphill “reverse” electron transfer. All three mechanisms are illustrated in Figure 7.

Redox arm is known in most methylotrophs (organisms that can consume one carbon substrates including methanol) as the common electron donation pathway. For this mechanism, electrons are retrieved by the series of reactions that oxidize formaldehyde to carbon dioxide. Specifically, the electrons are passed from the cofactor, NADH, to ubiquinone via the NADH dehydrogenase. The electrons from ubiquinone are then subsequently transferred to pMMO for methane conversion. The methanol generated is oxidized to formaldehyde via methanol dehydrogenase and the electrons are transferred down the ETC via cytochrome c to the eventual electron acceptor, oxygen. This mechanism essentially ties methane oxidation to aerobic respiration with the active roles of complex I (NADH dehydrogenase) and complex IV (cytochrome aa/o).

For direct coupling, the electrons for methane conversion come from the oxidation of methanol directly and is transported via cytochrome c to pMMO. Formaldehyde then is free to enter the assimilation pathways for biomass via the RuMP pathway. It is important to note the independence of methane oxidation from aerobic respiration in this electron pathway, where neither complex I nor IV are involved.

Uphill “reverse” electron transfer is a mixture of both direct coupling and re-dox arm methods. A fraction of electrons comes directly from methanol oxidation while the rest are provided by further metabolite reactions as seen in the redox arm mechanism. The proportion of electrons from both sources is defined in the model but less so experimentally. The mixture of both sources is then given to ubiquinone that is then used for methane oxidation from pMMO.

a)

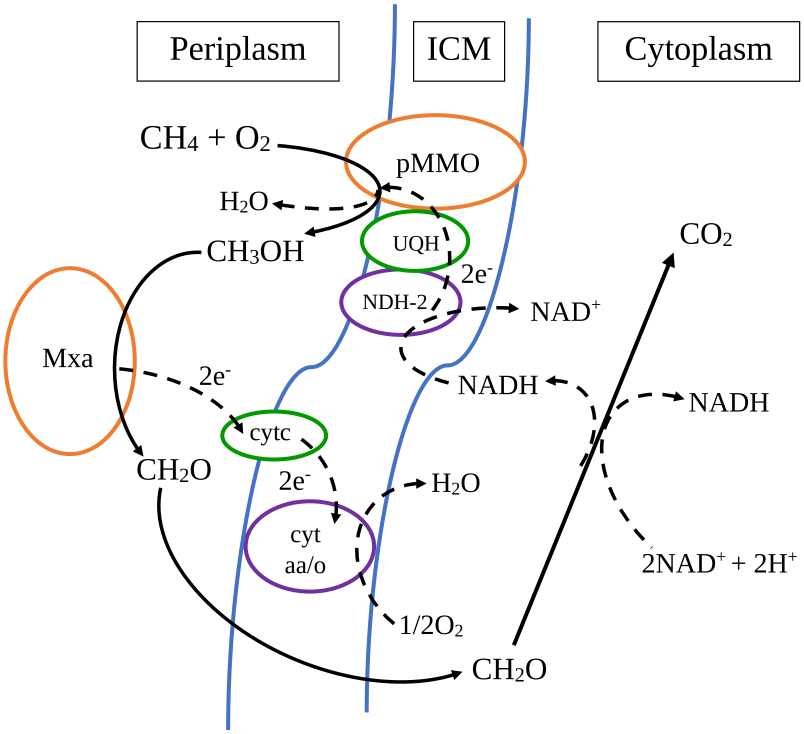

b)

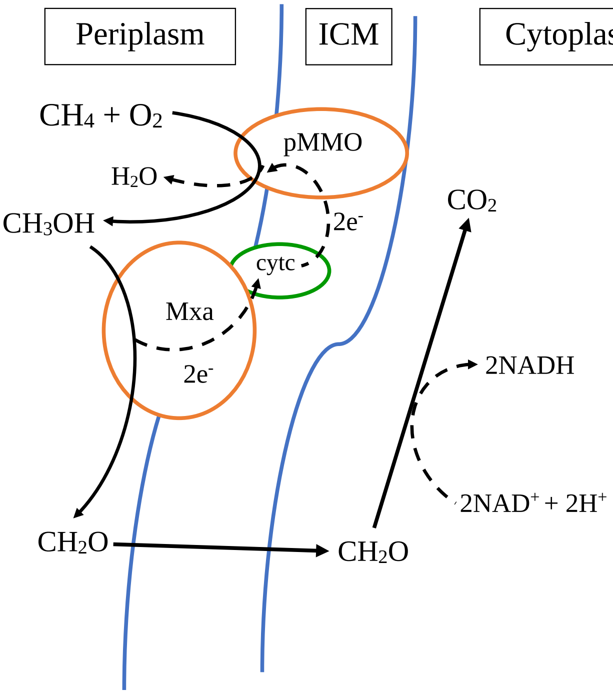

c)

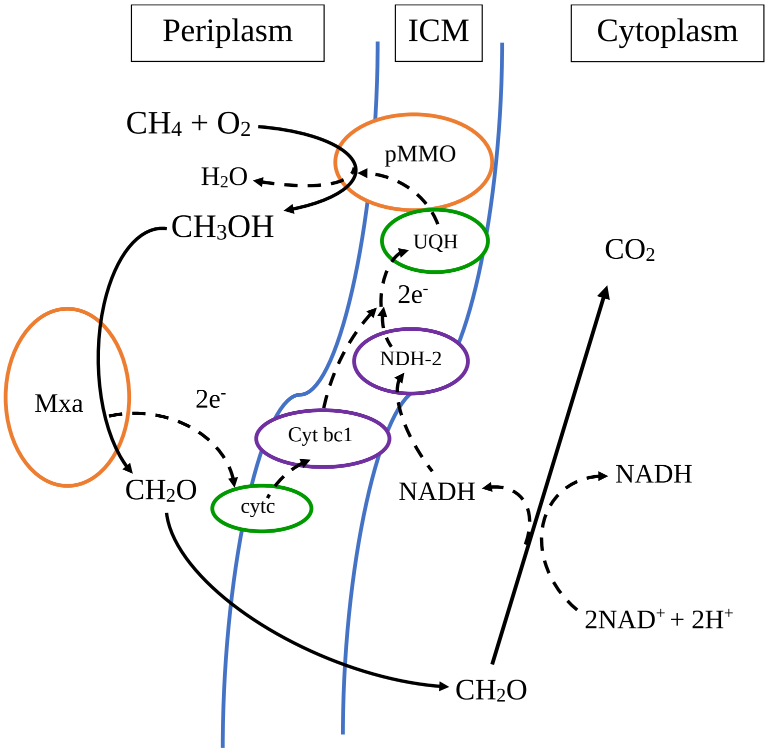

Figure 7: Various electron donor configurations for methane oxidation a) re-dox arm b) direct coupling, and c) uphill transfer. ICM stands for intercellular membrane. Orange circles are proteins involved with the main carbon pathways for methanotrophs. Green circles are carrier proteins that carry electrons from cofactors or other enzymes. Purple circles are proteins typically involved in aerobic respiration. This figure was recreated and adapted from de la Torre et. al. [106]

In the same study that constructed the full genome scale model, these routes were evaluated based off chemostat measurements of 5GB1. Of the three, the unconstrained network selected direct coupling as the most optimal solution for methane oxidation as its predicted growth rate and carbon conversion efficiency values correlated well with experimental data. For this study here, direct coupling is only considered due to the model’s ability to capitalize on efficient electron transfer as it attempts to maximize carbon distribution to the biomass flux.

Chapter 3 : Methanotroph Strain, Gas Mixing Development, and Analytical Protocol

3.1 *M. buryatense* 5GB1: A Promising Industrial Strain

M. buryatense 5GB1 is a fast growing methanotroph from a parent strain that was originally isolated from an Eastern Russia soda lake [109]. Due to its origins the strain is considered haloalkaliphilic with the ability to grow in higher salt (NaCl) concentrations up to 5% w/v and pH conditions from 6-10 [109]. These harsh conditions make it less susceptible to contamination from mesophilic organisms, but turn lead to eventual corrosion to metal reactor vessels and pumps [24].

In unrestricted growth, where the strain is not inhibited by methane or oxygen depletion, peak specific growth rates range are between 0.224-0.239 h^{-1} [36]. Compared to other strains, these growth rates are attractive to many methane bioconversion processes with the promise of shorter cultivation times. Additionally, product capabilities have been progressively researched to include biodiesel, ectoine, and lactate [24,29,67].

Due to the unorthodox nature of methanotrophs, the development of genetic tools have just recently developed in the last few years to increase production and manipulate metabolic pathways [38,67,110–112]. Such tools have been readily available to common organisms such as *E. coli* for the past two decades. Additionally, the full genome for 5GB1 has been mapped and in doing so, a genome scale metabolic model was constructed. This allows for *in silico* experimentation in an attempt to thoroughly understand how the metabolism of the cells behave and explore possible genetic mutations routes [106,107].

3.2 Gas Mixing System Development

One important, controllable factor for methane fermentation with 5GB1 is the transfer and subsequent uptake of methane and oxygen. These two gaseous substrates influence the phenotypes of methanotrophs that in turn affects growth rate, final cell density, and metabolite production [36]. However, limited studies have been done due to the availability of these mixtures and concerns regarding their explosive nature.

In this work, a safe gas mixing system is utilized to create various custom mixtures of oxygen, methane, nitrogen, and helium (Figure 8a and b). By assigning different mass flow controllers (MFCs) for each component of the gas stream and funneling the pure gasses to static mixers, any headspace composition can be created. Upstream of the MFCs are ball valves to isolate the gas from the mixing system and immediately downstream are check valves to prevent backflow to the controllers. The static gas mixers are 24 inches in length, to allow for the turbulent mixture to become uniform before entering the gas inlet for the vials or continuous reactors.

To ensure the safety of those conducting the research, several safety mechanisms were put in place as discussed in Chapter 1 Section 5. The failsafe, auto shut off gas system previously mentioned consists of a flammable gas detector with a relay that is connected to the electronic mass flow controllers and solenoid valves in the gas lines (Figure 9). If the power fails or if there is a detectable flammable gas, the system will automatically shut off the methane flow.

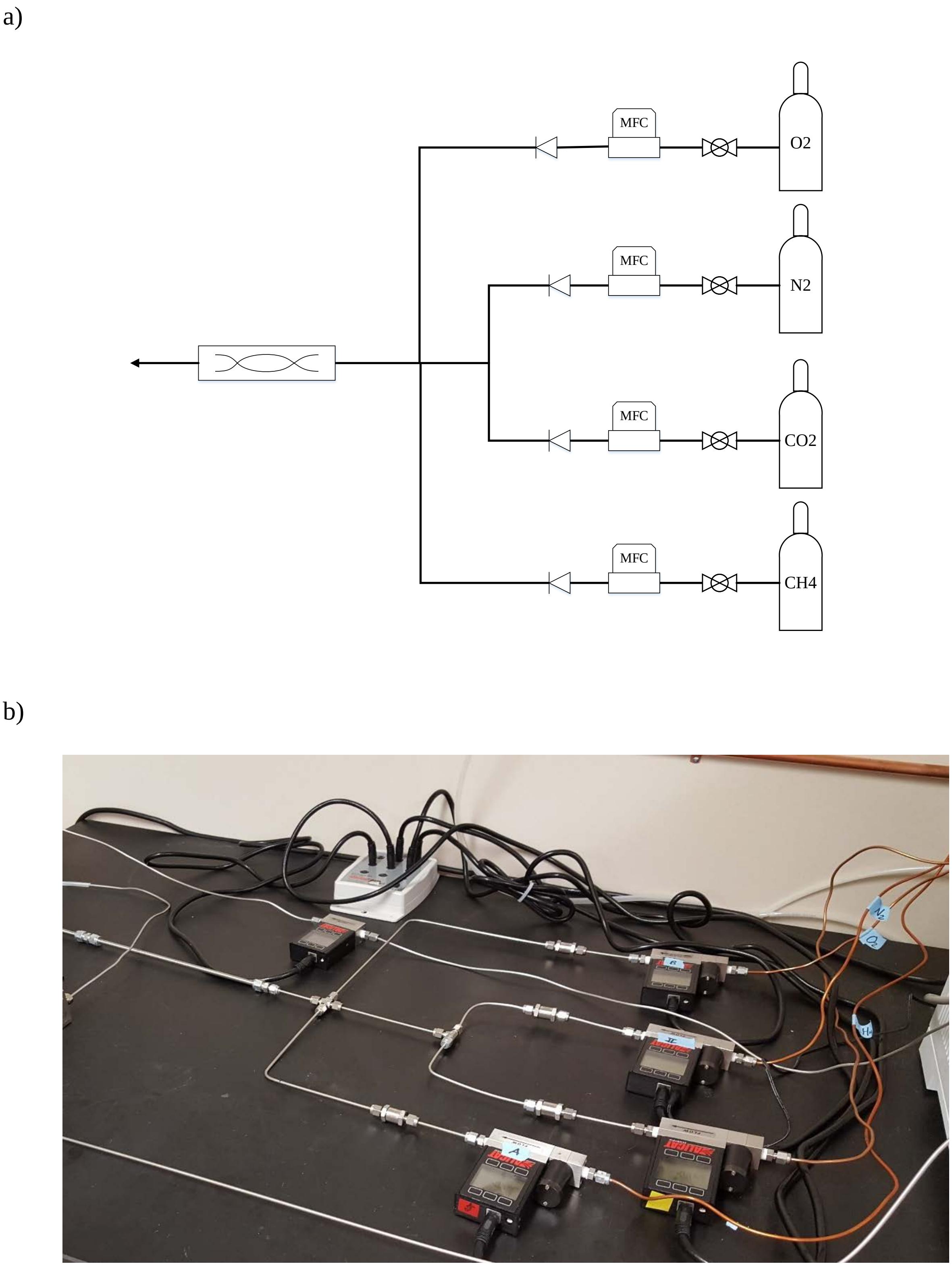

Figure 8: Gas mixing system developed for systemic studies. a) Schematic of mixing system b) Actual mixing system.

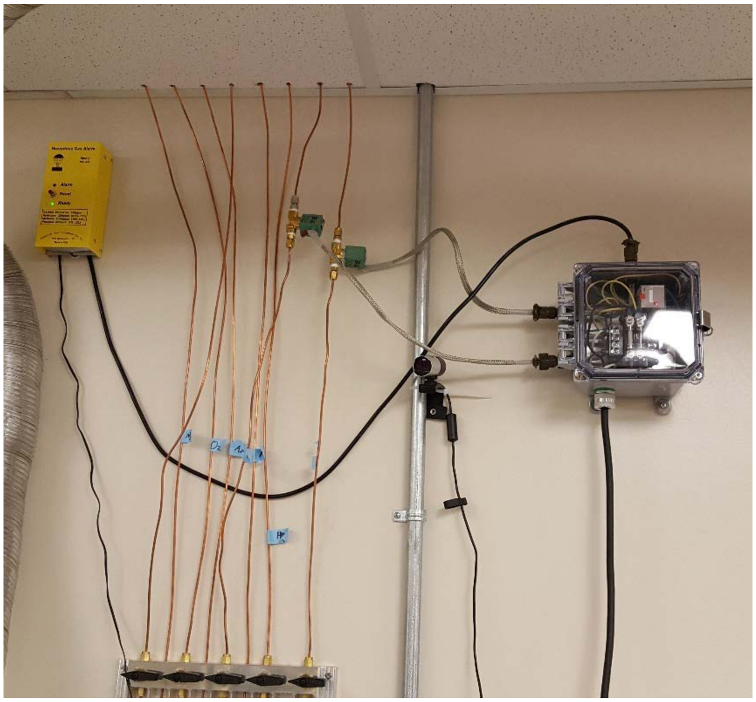

Figure 9: Gas safety system. The yellow box is the gas alarm connected to the relay box (grey and to the far right) that in turn controls the brass solenoid valves on the flow lines of methane.

3.3 CO_2 Solubility and Why It Matters

Alkaline medium is a considerably large sink for CO_2 because of basic water-carbon dioxide chemistry. Unlike many other gasses, when carbon dioxide in the headspace is in equilibrium with a liquid, there is also a chemical equilibrium that must be accounted for. Dissolved carbon dioxide in water is found predominantly in the same chemical form (CO_2) with a much smaller percentage (<1%) converted to carbonic acid (H_2CO_3). However, it is common practice to group both of these compounds into a synthetic carbonic acid form ($H_2CO_3^*$) [113].

The synthetic carbonic acid is then influenced by acidic equilibria to form bicarbonate (HCO_3^-) and carbonate (CO_3^{2-}), as shown in the following equations [113].

$$H_2CO_3(aq) \rightleftharpoons H^+(aq) + HCO_3^-(aq) \tag{3}$$

$$HCO_3^-(aq) \rightleftharpoons H^+(aq) + CO_3^{2-}(aq) \tag{4}$$

Due to the high pH conditions utilized (>9) in 5GB1 cultures, any produced carbon dioxide would dissociate accordingly to chemical equilibria and attempt to raise the hydrogen concentration that in turn, slowly decrease the pH of the solution. During initial growth and in the controlled chemostat cultures, carbon dioxide is present as stable ions in the liquid phase because of the carbonate buffer in typical NMS2 medium. For vial cultures with uncontrolled pH levels, the pH drops close to 8 in the late growth/stationary phase of the cell cultures and hydrogen becomes abundant in the liquid medium to the point where association would reoccur through Equations 2 and 3. This causes carbon dioxide to be released into the headspace via typical gas-liquid equilibrium, though a great amount of inorganic carbon remains as carbonate and bicarbonate.

Traditional Henry's law cannot be used for this complex equilibrium above, as it only accounts for one form of aqueous carbon dioxide (H_2CO_3) and gaseous carbon dioxide. It does not account for any aqueous carbon dioxide that disassociates to carbonate and bicarbonate. However, using common equilibrium constants, an effective Henry's law constant can be calculated (assuming the ionic strength is constant) via the following equation [114].

$$H_{CO2}^{*} = H_{CO2}\left(1 + \frac{K_{c1}}{[H^+]} + \frac{K_{c1}K_{c2}}{[H^+]^2}\right) \tag{5}$$

Where H_{CO2} is the typical Henry's constant and K_{c1} and K_{c2} equilibrium constants for the dissociation equations above. Thus, to calculate the effective Henry's law constant, all that is needed is an accurate measurement of the hydrogen ion concentration. Typically, this is done by using a pH probe that in turn measures the following:

$$pH = -\log A_H^+ = -\log[H^+]\gamma_{H^+} \qquad \textbf{(6)}$$

Where, A_H^+ is the activity of the hydrogen ions defined as the product of the hydrogen concentration and the activity coefficient, γ_{H^+}. In normal medium, this coefficient is assumed to be one and thus the measured pH is the amount of hydrogen ions. However, in NMS2 medium, the ionic strength of the high salt concentration is too large to ignore and the activity coefficient is not one. Though thermodynamic relations are available to calculate the activity coefficient, the ionic strength of the medium is far higher than allowed for these standard methods. Thus, using a standard Henry's constant is not entirely suitable to predict inorganic carbon content.

However, to illustrate the increased solubility of carbon dioxide, effective Henry's constants from Equation 5 across different pH regions were calculated. Various amounts of carbon dioxide and nitrogen were introduced to vials with 50 mL of NMS2 medium. In doing so, the ionic strength should remain relatively constant as no consumption or production from cells is occurring with an abiotic system. There was no initial carbon in the headspace and the original carbonate in the medium was measured via TC analysis (discussed later). Triplicate vials were created with headspaces of CO_2 concentration levels of 2, 5, 10, and 15%. Gasses was introduced to the vials with direct contact into the liquid medium (observed by the creation of bubbles) for 45 minutes. The gas flow was ceased and the septum was sealed with the mixture. The vials were stirred overnight via magnetic plates and a stir bar to allow for equilibrium. In the following morning, both the gaseous concentration of CO_2 and the final carbon in the liquid were measured. The amount of dissolved carbon dioxide from the introduced gas was taken to be the difference between the final and initial liquid measurements. Using Henry's law, the effective

Henry's constant, H, was determined via the measurements of the gas and liquid phase. This constant was related to the measured pH value after equilibrium and the results are shown in Figure 10.

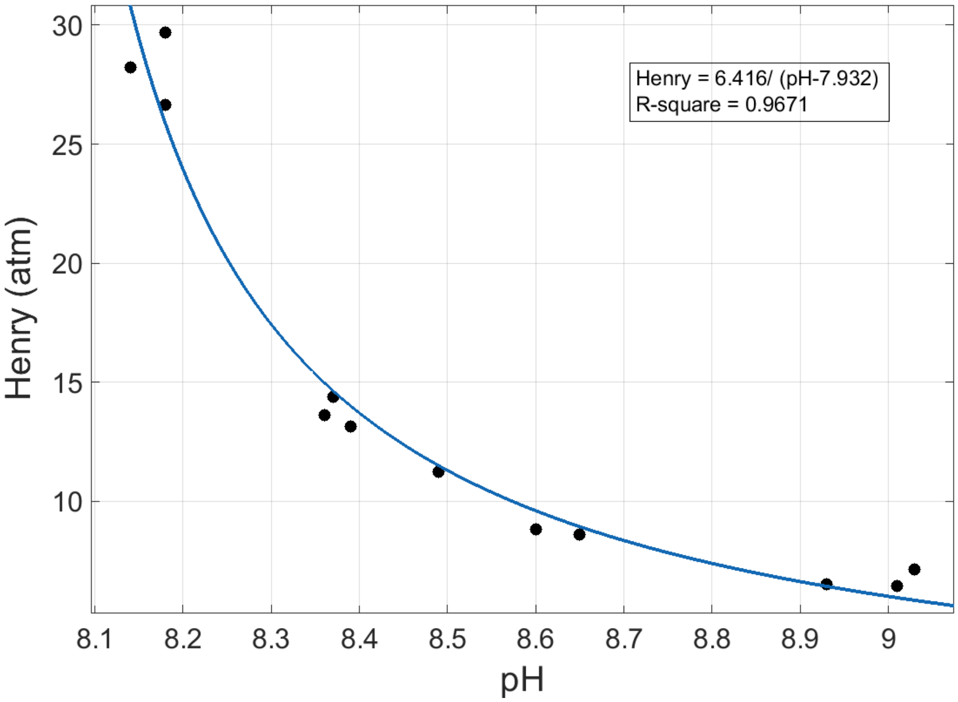

Figure 10: Relationship between the measured pH and calculated effective Henry's constant (atm). The block dots (●) are Henry constants calculated from measured carbon dioxide in the headspace and inorganic carbon in the liquid phase. The line represents the estimated curve relationship between the two factors.

Figure 10 demonstrates that the alkaline medium has an enhanced solubility for CO_2. The effective Henry constant that accounts for chemical equilibria ranged from 6.5-29.7 atm depending on the pH. This is significantly different from typical values for Henry's constants, which is about 1650 atm [115]. It should be noted again, that the above data is for illustrative purposes. During cell growth, the ionic strength of the solution changes because salts are consumed by the cells for nitrogen (KNO_3), sulfur ($MgSO_4$), and other elemental building blocks. In addition, the cells produce carbon dioxide that form carbonate and bicarbonate and effectively disrupt the ionic strength value. Ionic strength not only affects pH readings by a typical pH probe (see equation 6) but also the equilibrium constants of equations 4 and 5. This has been observed in another system with trimethylamine [116] in which the effective Henry's constant was altered by the amount of NaCl in the solution. Thus, for these experiments, inorganic carbon in the liquid phase was not estimated via Henry's law but rather through direct measurement.

3.4 Analytical Tools Utilized for Both Vial and Chemostat Experimentation

Gas analysis for was conducted with an Agilent Technologies 7890B GC system equipped with a TCD at 250^{o}C. The oven was held at a constant temperature of 60 ^{o}C throughout the analysis run. The carrier gas was nitrogen (ultra-high purity) that flowed through a valve system (held at 115^{o}C) to analyze methane, oxygen, and carbon dioxide with the use of Unibeads IS 60/80 mesh and MolSieve 5A 60/80 SST columns. For the chemostat culture a SRI 8610C gas chromatographer with a Silica column was used to quantify dilute amounts of CO_2. The oven in the system was maintained at 80 ^{o}C and the TCD at 100^{o}C.

Total carbon (TC) and inorganic carbon (IC) in the liquid phase was analyzed via a Shimadzu TOC-V_{CSN} analyzer. Inorganic carbon analysis required the use of 2M HCl that was injected at 8.0% vol/vol. Through this injection, the pH of the sample is dropped below 3 and the carbon from bicarbonate and carbonate become CO_2 that is easily sparged and analyzed. Sample preparation was done as follows: liquid gathered from the cell cultures were first centrifuged at 10,000 rpm for 10 minutes using an Eppendorf 5415 D centrifuge. Retrieved supernatant was filtered with a 0.2 µm nylon membrane (VWR) to remove any lingering cell biomass. The filtered solution was then diluted (6x for vial cultures and variably for the chemostat) before being used for TC and IC analysis. Total organic carbon (TOC) was taken to be the difference between TC and IC measurements.

Cell biomass was measured via a Beckman Coulter DU Life Science UV/Vis spectrophotometer. Samples were taken at a fixed wavelength (OD_{600}) and calibrated to biomass concentration in units of g dry cell weight per liter (g DCW L^{-1}).

3.5 Re-pressurizing Vials for Accurate Headspace Analysis

To conduct a comprehensive carbon balance, accurate measurement of headspace gas composition is required. As growth occurs in the closed system, methane and oxygen are consumed that decrease the overall moles of gas present. In addition, headspace volume increases as liquid samples are taken (see Figure 11). Thus, the vials are under pressurized (P< 1 atm) at stationary phase. To re-pressurize the vials, nitrogen was added till atmospheric pressure was reached, as measured by a manometer, and at this point a gas measurement was taken.

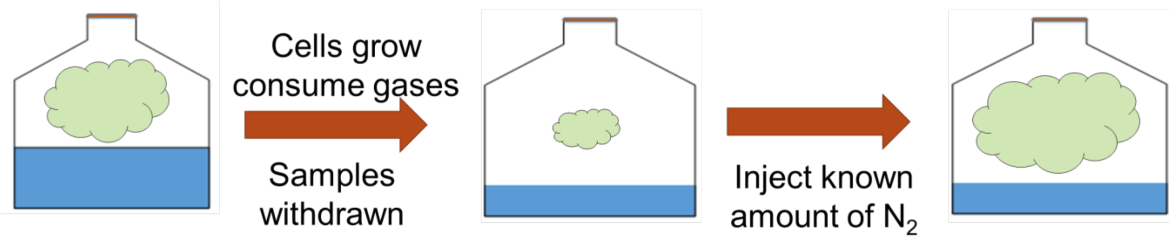

Figure 11: Re-pressurization for batch cultures of 5GB1

This methodology was tested by using separate serum vials filled with 150 mL of distilled water that allowed for 100 mL of headspace. The headspace was then filled continuously with a certain mixture of oxygen, methane, carbon dioxide, and nitrogen for 15-20 minutes. The initial headspace was measured with the gas chromatographer and the amount of mmols of each gas was calculated. A portion of the water was then removed (~100 mL) carefully via syringe through the septum cap. This increase in headspace volume causes an inversely proportional pressure drop. For instance, if headspace volume doubles through the removal of water, the pressure will drop by half. This effectively mimics the pressure drop experienced during actual experimentation. The system with depleted water was then filled with nitrogen for a final gas measurement. Using Henry's law, dissolved methane, oxygen, and carbon dioxide were accounted before liquid removal and after. From the results listed in Table2, minimal errors were overserved with methane and carbon dioxide, indicating minimal disruption for an accurate carbon balance.

a) Methane Results

	Initial gas	Initial liquid	Total Initial	Final Gas	Final Liquid	Withdrawn	Total Final	% of Initial
Trial 1	0.278	0.015	0.293	0.280	0.003	0.010	0.293	100%
Trial 2	0.290	0.014	0.304	0.299	0.003	0.009	0.311	100.6%
Trial 3	0.298	0.014	0.312	0.296	0.008	0.004	0.308	98.7%

b) Oxygen Results

	Initial gas	Initial liquid	Total Initial	Final Gas	Final Liquid	Withdrawn	Total Final	% of Initial
Trial 1	0.617	0.032	0.649	0.657	0.006	0.020	0.683	105.2%
Trial 2	0.656	0.031	0.687	0.702	0.006	0.020	0.728	106.0%

Trial 3	0.675	0.030	0.705	0.688	0.017	0.008	0.713	101.1%

c) Carbon Dioxide Results

	Initial gas	Initial liquid	Total Initial	Final Gas	Final Liquid	Withdrawn	Total Final	% of Initial
Trial 1	0.740	1.017	1.757	0.852	0.201	0.642	1.695	96.5%
Trial 2	0.786	0.983	1.769	0.907	0.196	0.630	1.733	98.0%
Trial 3	0.799	0.957	1.756	0.871	0.566	0.253	1.690	96.2%

Table 2: Results of re-pressurization examination with mixtures of a) methane, b) oxygen, and c) carbon dioxide in water. Vials were filled with nitrogen to raise pressure to atmospheric levels. All values are in mmols, unless stated otherwise.

As shown above, all gasses are accounted for with average errors of < 5%. The increase in oxygen is due to the few stray air bubbles that make its way into the vial when the vacuum becomes too large and water continues to be withdrawn. Overall the re-pressurization method was adopted for the vial experimentation, the results of which are discussed in the next chapter.

3.6 Headspace Analysis for Chemostat Cultures

For actively growing chemostats, methane and oxygen are continuously consumed for steady state and dynamic conditions. In doing so, the effluent flow rate from the continuous system drops noticeably, especially with higher biomass concentrations. In order to achieve a reliable carbon balance, the altered flow rate must be accounted for. In this work, flow rate was calculated by a mole balance of helium. This gas is utilized as a tracer that is constantly introduced into the gas stream for accurate measurement. Helium is selected for several reasons: 1) It is an inert gas with no toxic effects on cell viability, 2) Due to this thermal conductivity, the gas is easily detected by the GC, and 3) Helium is far less soluble than oxygen with a dimensionless Henry constant of 9 $*10^{-3}$ versus 3* 10^{-2} [115] creating minimal loss to liquid medium.

To prove this concept in an abiotic fashion, the bioreactor was filled with about 1.5L of tap water and fed a mixture of gasses at 300 smL min^{-1}, the same gas flow rate used in the methanotroph runs. The agitation was 500 rpm. Two sets of experiments were completed based off helium concentrations of 10 and 9.3%, with nitrogen as the balance. Gas samples were taken from the effluent gas stream, alongside effluent temperature measured from an online temperature probe purchased from Vernier Software and Technology. Together these measurements (the concentration from the GC and the gas temperature) were inputted into Equation 7 to calculate the mole faction of the interested component (helium, methane or oxygen). With the mole fraction of helium in the effluent known, the flow rate can be estimated via a simple mass balance (Equation 8).

$$y_{out} = \left(\frac{n}{V}\right) * \frac{RT}{P} = GC_{reading} * \frac{RT}{P} \tag{7}$$

$$\frac{F_{in} * y_{He}}{y_{out}} = F_{out} \tag{8}$$

Assuming that nitrogen’s and helium’s concentration within the water is minimal (since both Henry’s constants are rather large), the flow rate out can be measured in this circumstance with an Alicat mass flow meter as a mode of comparison. The results are illustrated in Table 3 where the mass flow rate calculated by gas concentration is compared to the direct measurement.

It should be noted that neither the bioreactor temperature nor the condenser temperature was controlled during this time.

Helium Set	Y_out	Flow rate calculated (mmol/min)	Flow rate measured (mmol/min)	% error
10%	9.84	12.68	12.49	1.48
10%	9.87	12.64	12.48	1.26
10%	9.83	12.89	12.49	3.24
10%	9.79	12.91	12.49	3.34
9.33%	9.12	12.76	12.49	2.16
9.33%	9.12	12.97	12.49	3.82
9.33%	9.08	12.98	12.50	3.88

Table 3: Comparison of calculated flow rate via gas concentration to measured values using helium as a tracer.

From the results above, it is apparent that the flow rate calculated by the mass balance of helium experiences a slight positive error (average was 2.74%) from the measured flow rate. These errors could possibly arise by the manual injection into the GC or the presence of water vapor from sparged gas that would dilute the streams.

To further evaluate the tracer gas system, methane, oxygen, helium, and nitrogen (10%, 20%, 10%, and 60%, respectively) were sent through the bioreactor with tap water that was agitated at 400 rpm, temperature controlled at 30^{o}C, and effluent condenser maintained at ~5^{o}C. As before, the GC concentration and temperature prober were utilized to calculate the gas flow rate. Again, the flow rate was measured by a mass flow meter for comparison purposes. The overall results are demonstrated in Table 4.

Y CH_4	Y O_2	Y He	Flow out calculated (mmol/min)	Flow out measured (mmol/min)	% error	Methane Balance Error (%)	Oxygen Balance Error (%)
0.098	0.197	0.097	12.59	12.26	2.63	0.23	0.99
0.098	0.197	0.097	12.69	12.26	3.51	1.43	1.95
0.098	0.200	0.097	12.68	12.26	3.37	1.71	3.14
0.098	0.195	0.097	12.68	12.26	3.40	0.89	1.05
0.098	0.195	0.097	12.60	12.26	2.73	0.72	0.37
0.098	0.195	0.097	12.65	12.26	3.12	0.59	0.62
0.098	0.196	0.097	12.66	12.26	3.22	1.10	0.98

Table 4: Flow rate evaluation and mole balance for methane and oxygen with calculated gas flow rate using helium as a tracer.

As before, the flow rate demonstrated less than 4% error (average was 3.14%), while the mole fraction measured was slightly lower than inputted levels. The combined behavior of mole fraction and flow rate perceivably introduced minor error to the methane and oxygen balance (within 2%). Thus, helium as a trace gas will provide a satisfactory estimate of methane and oxygen consumption for chemostat cultures with calculated flow rates. This concept is utilized in two case studies for continuous cultures in Chapter 5, Sections 1 and 2. Additionally, the challenges associated with chemostat carbon analysis without a tracer gas is illustrated in Chapter 5 Section 3.

Chapter 4 : Systematic Carbon and Growth Characterization of *M. buryatense* 5GB1

4.1 Objective and Methodology of Study

Despite *M. buryatense*'s promising potential, only Gilman et al. has initially attempted to undergo phenotype characterization under balanced growth, a single level of oxygen limitation and another for methane limitation [36]. To enhance this current body of knowledge without any gas mixture limitation, a systematic approach was developed to monitor the carbon distribution and growth patterns of 5GB1 under various headspace conditions. In particular, the influence of methane and oxygen partial pressures (pCH_4 and pO_2) on growth were evaluated. Additionally, an effective carbon balance was completed to examine overall carbon dispersion amongst the three main carbon sinks: carbon dioxide, organic liquid matter, and biomass.

Five case studies are presented in this chapter. The first half of the results focus on the evaluation of methane's and oxygen's influence on growth (Cases 1,2, and 3). The other half addresses the carbon distribution amongst various headspaces considered (Cases 4 and 5). It is important to note that the specific and overall growth rates achieved in this study are significantly lower than those reported previously for this strain which were 0.21-0.23 h^{-1} [36,110]. This is attributed to two main reasons. The first is due the poor transfer rate of the gasses from the headspace to the liquid medium in a vial shaken at 200 rpm. However, this growth rate was necessary as it allowed for multiple (8-16) vials to grow throughout the days of experimentation and compensated for lengthy sample/analysis time. Secondly, a large cell inoculum was utilized, as diluted cell concentration may strongly affecting carbon balance.

4.2 Case Outlines and Experimental Parameters

Methylomicrobium buryatense 5GB1 was provided by Dr. Mary Lidstrom from the University of Washington and grown in modified nitrate mineral salts (NMS2) medium as described by Puri et al. [110]. Initial pre-cultures were inoculated from plates to the 50 mL of medium contained within 250 mL serum vials. The vials were topped with a rubber septum and crimped with an aluminum cap. The headspaces of pre-culture sets were a 1:1 atmosphere of methane and oxygen generated by continuously feeding the vial through the gas mixing system with a mixture of 35% methane, 35% oxygen, and 30% nitrogen for five to seven minutes at 200 smL min^{-1}. After gas feeding, the input and output streams were removed from the septum so that the gasses were trapped. Pre-culture and experimental vials were grown in a Lab-Line Orbit Environ-shaker with a rotation speed of 200 rpm and temperature controlled at 30^{o}C.

The headspaces created for all case studies are listed in Table 5 and all vial sets were performed in duplicate. Cases 1, 2, and 3 evaluate methane's and oxygen's influence on growth rate. The carbon distribution amongst various headspaces are studied and analyzed in Cases 4 and 5 based off the influential factors from the previous cases. The flasks were filled with 50 mL of medium and capped in the same fashion as the pre-culture. Gas mixtures were fed continuously at a total flow rate of 200 smL min^{-1} for 5-7 minutes and then an initial gas sample was taken to verify desired composition and for later cases, the methane input for the carbon balance. After this gas sample, another five minutes of gas feeding was allowed to maintain the same headspace concentrations.

O_2:CH_4	O_2	CH_4	N_2
Case 1			
2:1*	0.40	0.20	0.40
1.33:1	0.40	0.30	0.30
1:1	0.40	0.40	0.20
0.66:1	0.40	0.60	0
3:1	0.60	0.20	0.20
2:1	0.60	0.30	0.10
1.5:1	0.60	0.40	0
Case 2			
1.07	0.30	0.28	0.42
0.833	0.30	0.36	0.34
0.667	0.30	0.45	0.25
1.96	0.55	0.28	0.17
1.53	0.55	0.36	0.09
1.22	0.55	0.45	0
Case 3			
0.66:1	0.20	0.30	0.50
1:1	0.30	0.30	0.40
1.33:1	0.40	0.30	0.30
1.5:1	0.45	0.30	0.25
1.66:1	0.50	0.30	0.20
1.83:1	0.55	0.30	0.15
2:1	0.60	0.30	0.10
2.33:1	0.70	0.30	0
Case 4			
1:1	0.35	0.35	0.30
1.2:1	0.42	0.35	0.23
1.6:1	0.56	0.35	0.09
1.8:1	0.63	0.35	0.02
Case 5			
1:1	0.20	0.20	0.60
2:1	0.40	0.20	0.40
3:1	0.60	0.20	0.20
4:1	0.80	0.20	0

Table 5: Outline of the methane, oxygen, and nitrogen used for each vial in set in the case studies covered. The values listed under each gas is the partial pressure within the vials in atm. Note that since there were two 2:1 gas mixtures for Case 1, the first with the partial pressure of 0.4 atm of oxygen was referred to as 2b:1 in figures below.

Pre-culture vials were grown till mid exponential growth phase as measured by specific growth rates. Systems that exhibited the best growth were harvested. The liquid medium and cells were centrifuged to cell pellets that were then re-suspended in fresh NMS2 medium to remove the effects of any extracellular organic carbon for the carbon and growth analysis. This inoculum was then injected to each of the vials to create an initial concentration of 0.05-0.06 gDCW L^{-1}. After inoculation was complete, the first sample was taken and the time was referred to as t = 0 hrs.

Samples were taken multiple times on the initial day to monitor if or when a peak growth rate occurs. In Cases 4 and 5, subsequent samples were taken the following day(s) less frequently till stationary phase was reached as defined by negligible values in specific growth rates (see Equation 9). Additionally, for these cases each sample volume was measured in order to complete the carbon balance. Samples withdrawn in all cases were subject to OD measurement for biomass concentration and samples for Cases 4 and 5 also underwent TC/IC measurement for liquid carbon analysis.

4.3 Carbon Balance and Growth Rate Considerations

There are three initial sources of carbon that must be accounted for the carbon balance. The first is the amount of methane fed into the system, as measured by the initial headspace sample. Secondly, there are carbonate ions in the buffer from the medium and of the inoculated pre-culture. Thirdly, the inoculated biomass is produced from the pre-culture’s methane. Any initial carbon from the buffer or inoculated biomass must not be considered for the carbon balance, as this carbon is separate from the substrate of interest and will inflate the results. Both of these are measured and thus a baseline of the initial carbon is created. The subsequent liquid and biomass samples then utilize this baseline to account for the actual carbon consumed. Any dissolved methane left over within samples or final liquid measurement is not accounted for because of the insoluble nature of the gas. This assumption was thought to have a negligible impact, if any.

The carbon consumed is measured from the liquid phase, biomass, and headspace. Carbon in biomass was determined by the mass flux equation used in the genome scale metabolic model [106]. This came out to be approximately 39.3 mmol C gDCW^{-1}. A key assumption to keep in mind is that the carbon in biomass varies negligibly over the oxygen or methane limited conditions. A similar assumption was verified with another methanotroph, *Methylomonas flagellata* [117] who experienced insignificant differences in the organism's carbon makeup. The liquid carbon is measured via TC/IC analysis. Finally, vials were re-pressurized till atmospheric pressure was reached, as measured by a manometer, an accurate gas measurement was taken. The analytical methods are discussed in detail in Chapter 3 Section 5.

Specific growth rate between points was calculated as follows.

$$\mu = \frac{\ln\left(\frac{X_i}{X_{i-1}}\right)}{t_i - t_{i-1}} = \frac{\ln(X_i) - \ln(X_{i-1})}{t_i - t_{i-1}} \qquad \textbf{(9)}$$

Where, μ is the specific growth rate (h^{-1}), X is cell concentration (g DCW L^{-1}), and t, is time in hours of sample point, i, and the previous sample point, i-1.

The overall growth rate (μ_{ovr}) is found via non-linear fitting of several pairs of time and biomass concentration data along the typical biomass equation (Equation 10) with delay time, d. This analysis was done through the nonlinear fit options within Matlab.

$$X = \mu_{ovr} * e^{(\mu_{ovr} * (t-d))} \qquad \textbf{(10)}$$

4.4 Case Studies 1-3: Oxygen vs Methane Influence

In this section, the influence of oxygen and methane concentration on growth rate (specific and overall) were evaluated. For Cases 1 and 2, two groups were created based off the oxygen partial pressure fed. Each group then consisted of three to four sets determined by methane concentrations. In doing so, this creates a systematic approach to evaluate not only the influence of each gas, but also the combinational ratio of the two.

The growing biomass for Cases 1 and 2 are demonstrated below in Figure 12a and b where it is apparent that growth observed in the first day separated the vials into two groups. These groups are defined by the oxygen presence rather than methane, suggesting that oxygen's influence dominate growth in both cases. Specifically, groups with headspaces that consisted of the larger oxygen partial pressure tended to grow significantly slower. Additionally, the duplicates of each vial set varied insignificantly without affecting the separation observed.

a)

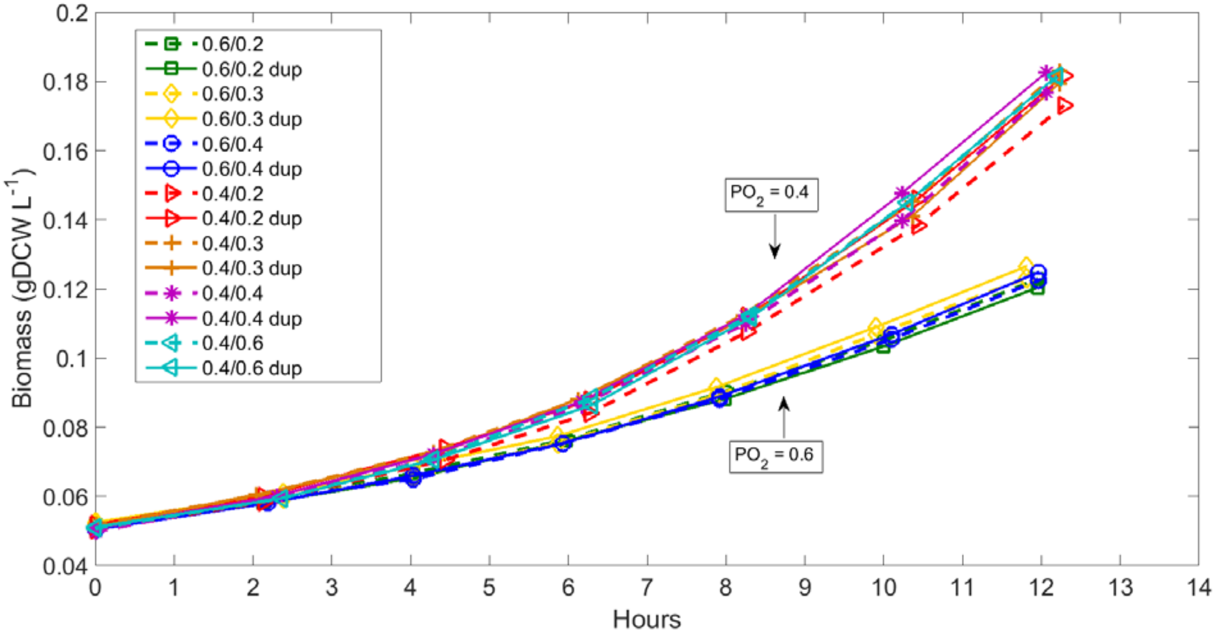

b)

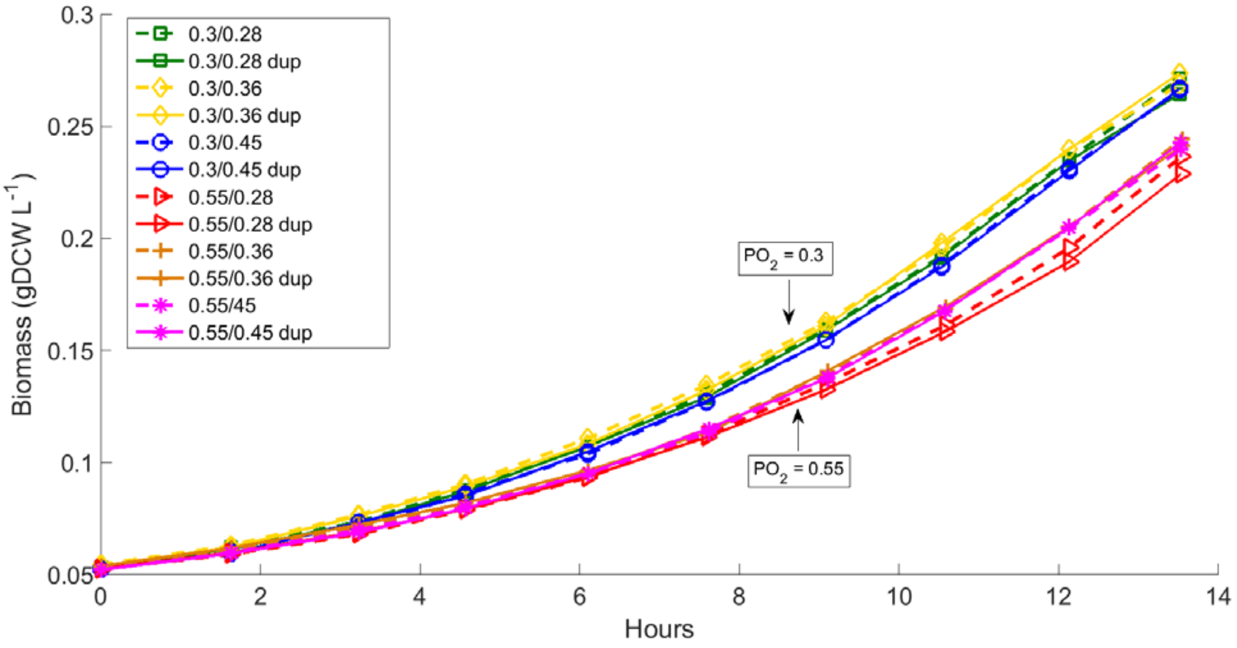

Figure 12: Growth curves for a) Case 1 and b) Case 2. The legend is labeled as partial pressure of oxygen over partial pressure of methane fed to the vial.

The overall growth rates were then gauged on a time basis for both cases, meaning that the data from the initial time point till a desired time point were taken collectively to estimate the growth rate in Equation 10. The estimated overall growth rates along the time of testing are illustrated in Figure 13 a and b.

a)

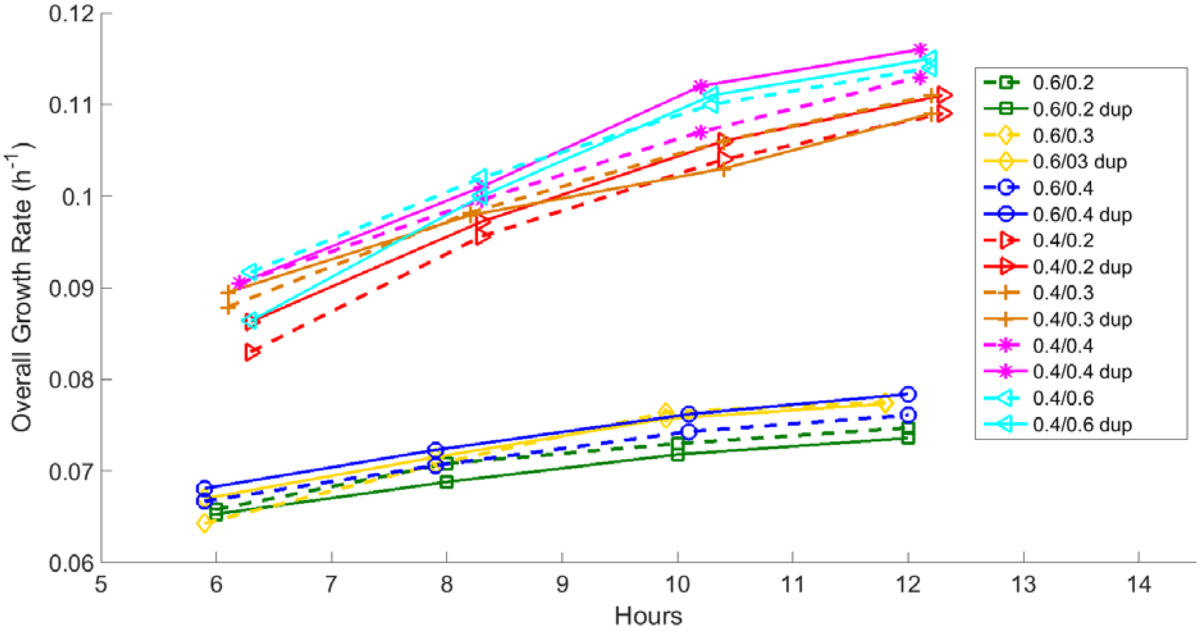

Overall Growth Rate (h^{-1})
0.12
0.11
0.1
0.09
0.08
0.07
0.06
5
6
7
8
9
10
11
12
13
14
Hours
0.6/0.2
0.6/0.2 dup
0.6/0.3
0.6/03 dup
0.6/0.4
0.6/0.4 dup
0.4/0.2
0.4/0.2 dup
0.4/0.3
0.4/0.3 dup
0.4/0.4
0.4/0.4 dup
0.4/0.6
0.4/0.6 dup

b)

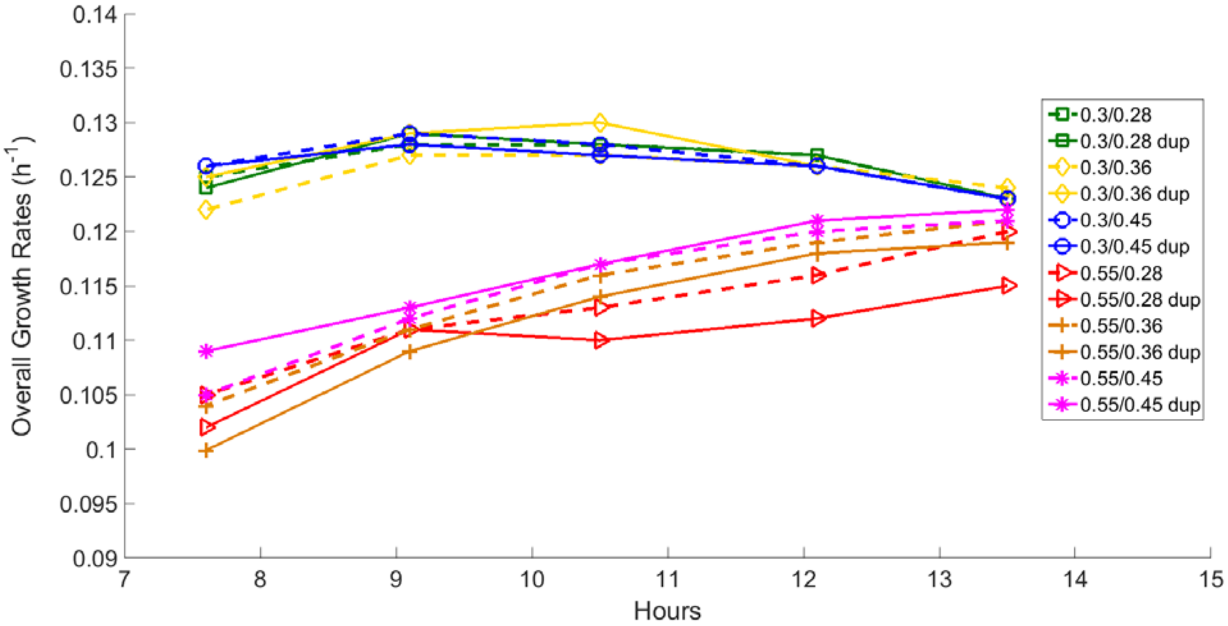

Overall Growth Rates (h^{-1})
0.14
0.135
0.13
0.125
0.12
0.115
0.11
0.105
0.1
0.095
0.09
7
8
9
10
11
12
13
14
15
Hours
0.3/0.28
0.3/0.28 dup
0.3/0.36
0.3/0.36 dup
0.3/0.45
0.3/0.45 dup
0.55/0.28
0.55/0.28 dup
0.55/0.36
0.55/0.36 dup
0.55/0.45
0.55/0.45 dup

Figure 13: Overall growth rates for a) Case 1 and b) Case 2. The legend is labeled as partial pressure of oxygen over partial pressure of methane fed to the vial.

As exhibited in Figure 13a, there appears to be an increasing trend in growth rates over time for those vials with oxygen presence of 0.4, while those with a pO_2 of 0.6 atm appears to increase at a noticeably slower rate. At 12 hours the average overall growth rates (as determined by Equation 10) are 0.112 $\pm$ 0.002 and 0.076 $\pm$ 0.001 h^{-1} for atmospheres of pO_2 0.4 and 0.6 atm, respectively. Results shown in Figure 13b show consistently higher growth rates at 12.1 hours with values of 0.128 $\pm$ 0.001 h^{-1} and 0.118 $\pm$ 0.003 h^{-1} for pO_2 of 0.3 and 0.55 atm, respectively. Interestingly the latter group (with pO_2 of 0.55) exhibited increasing growth rates later in the experiment that approached those of first group (at 13.5 hours, growth rate was 0.120 $\pm$ 0.003 h^{-1}). This behavior is currently postulated with two theories. Firstly, the group of vials with 0.3 pO_2 experienced larger cell concentrations early on that would in turn require larger oxygen demands. This may cause enough deprivation of dissolved oxygen to occur so that poor gas transfer in a vacuum setting becomes highly influential. Secondly, the group with 0.55 atm pO_2 may have seen experienced alleviation of oxygen inhibition due consumption to a point where the dissolved oxygen concentration was far more tolerable and allowed for rising cell growth rate over time.

From these two cases, oxygen's influence is predominant with methane initial concentrations having little to no noticeable effects. To expand on the studied oxygen concentration, Case 3 was conducted in a fashion that standardized the amount of methane in each vial while increasing the amounts of oxygen. Since Cases 1 and 2 showed inhibition at pO_2

of 0.55 and 0.6 atm, oxygen levels between 0.4 and 0.6 atm were broken down to 0.05 increments.

After inoculation for Case 3, the growth patterns of the first day presented in Figure 14a confirm the influential factor oxygen has on growth rates. At hour 8 the biomass concentration decreases in value with the increased initial presence of oxygen. Hour 14 displays the same general behavior except for the obvious decrease in biomass for vials with a pO_2 of 0.2 atm. These vials experienced sharp declines in specific growth rates between hours 8 (0.14 h^{-1}) and 14 (0.10 h^{-1}), as indicated by Figure 14b. This declination was presumably because of oxygen limitation and thus, the growth pattern was not sustained. The cells continued to grow till stationary phase (Figure 14b). The larger oxygen supply in vials allowed for larger biomass concentrations till methane in turn became the limiting substrate, which occurred with pO_2 of 0.45 atm and higher.

From the data accumulated in the first day, overall growth rates were found by fitting towards the typical growth curve with delay time (Equation 10). These values were then plotted against the pO_2 fed to each vial as plotted in Figure 15a. The trend illustrated with the blue line demonstrates that a relative maximum occurred with initial pO_2 of 0.3 atm, though the values of 0.2 and 0.4 atm are comparable. Beyond 0.4 atm, the growth rate declines steadily with increasing oxygen concentration. It is important to note that this maximum was achieved through batch experimentation with gas transfer depending on shaker speed. This relative maxima and rate of declination may be significantly different with more efficient transfer of oxygen (i.e. a continuously aerated and stirred reactor) that in turn may increase oxygen tension in a more consistent manner. Appendix A provides indicative evidence of such, but the concept was not thoroughly explored beyond this point.

a)

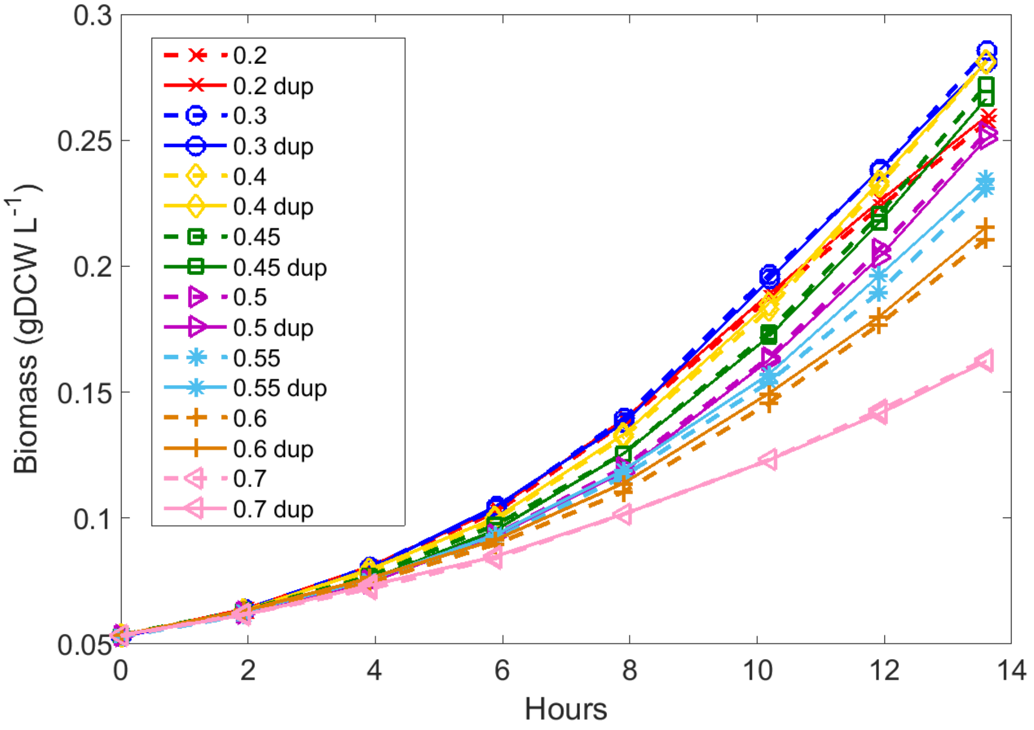

0.2
0.2 dup
0.3
0.3 dup
0.4
0.4 dup
0.45
0.45 dup
0.5
0.5 dup
0.55
0.55 dup
0.6
0.6 dup
0.7
0.7 dup
Biomass (gDCW L^{-1})
0.3
0.25
0.2
0.15
0.1
0.05
0
2
4
6
8
10
12
14
Hours

b)

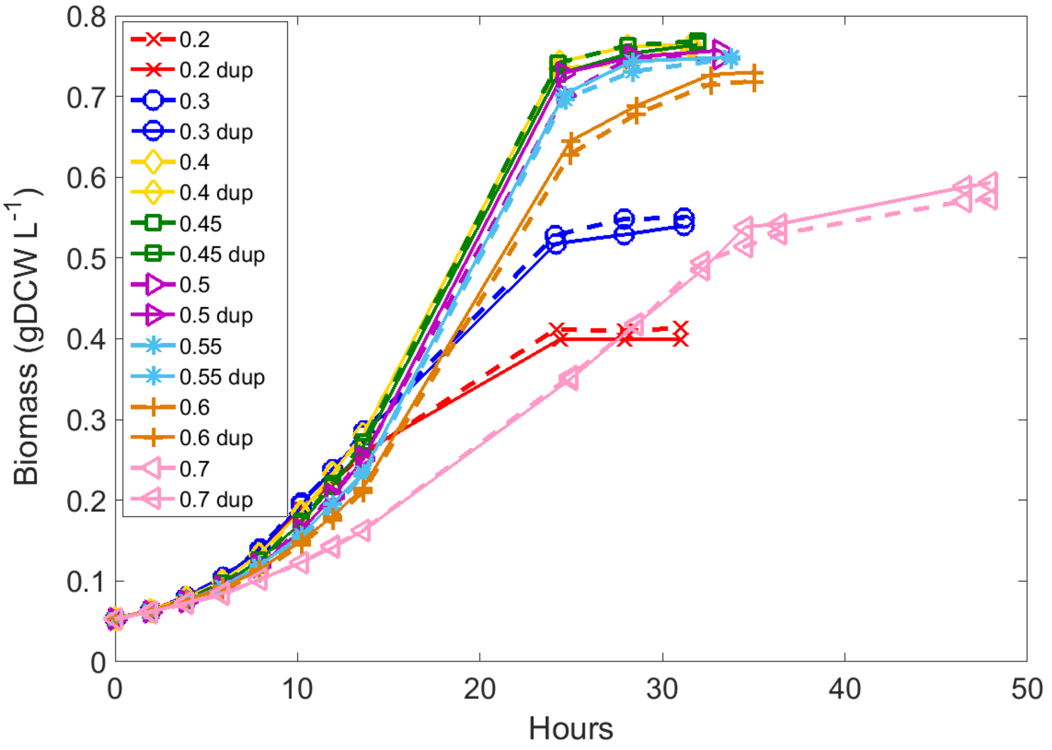

0.2
0.2 dup
0.3
0.3 dup
0.4
0.4 dup
0.45
0.45 dup
0.5
0.5 dup
0.55
0.55 dup
0.6
0.6 dup
0.7
0.7 dup
Biomass (gDCW L^{-1})
0.8
0.7
0.6
0.5
0.4
0.3
0.2
0.1
0
0
10
20
30
40
50
Hours

Figure 14: Biomass concentration (g DCW L^{-1}) over the initial 14 hours (a) and the total time frame (b) in the vials for Case 3. The solid and dashed lines amongst the different shapes represent each vial of a duplicate set. The legend refers to the partial pressure of oxygen fed to the vial.

a)

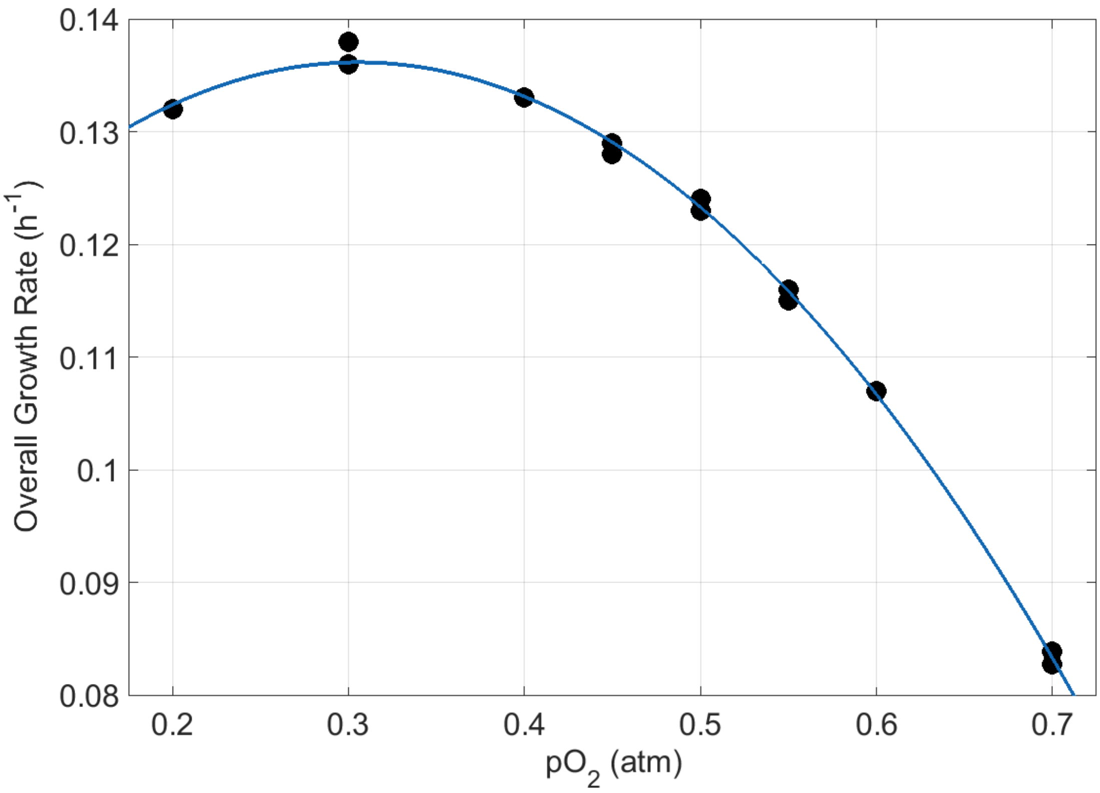

Figure 15: Overall growth rates vs oxygen partial pressure for Case 3. The overall growth rates determined for each vial in the duplicates sets are represented as black dots while the trend line illustrates the declining behavior observed.

4.5 Case Studies 4 and 5: Carbon Distribution Amongst Various Headspaces

From the cases above, it is clear that oxygen has an impact on cell growth, however what remains unclear is oxygen's influences on carbon distribution. Thus, Cases 4 and 5 were created to evaluate how carbon is dispersed amongst biomass, CO_2, and liquid organic matter.

For Case 4, the overall growth of the vials are shown in Figure 16a and the specific growth (derived from Equation 9) associated with the first 15 hours are plotted in Figure 16b. Again, the order of the growth is clearly associated with initial oxygen concentrations. The oxygen limited vials (pO_2 of 0.35 and 0.42 atm) had peak specific growth rates of $0.173 \pm 0.002\ h^{-1}$. Vials with pO_2 0.56 atm reached an average peak growth rate of $0.129\ h^{-1,}$ while those with pO_2 0.63 atm experienced a slower rate of $0.115\ h^{-1}$. Additionally, the larger oxygen content had an impact on the final cell concentration. Vials with pO_2 0.35 atm reached stationary phase with an average cell concentration of 0.62 gDCW L^{-1} and those with pO_2 0.42 atm leveled off at 0.77 g DCW L^{-1}. Both sets resided in stationary phase with hardly any oxygen left in the headspace (<0.34 mmol L^{-1}) and an abundance of methane, confirming the oxygen limitation expected. Due to the larger oxygen content of vials with pO_2 0.42 atm, more methane was consumed (see Table 6) and accumulated larger biomass. Vials with headspace compositions of pO_2 0.56 and 0.63 atm reached biomass densities of 0.85 and 0.86 g DCW L^{-1}, respectively. Both had depreciated amounts of methane left in the headspace (<0.25 mmol L^{-1}) with an abundance of oxygen that confirmed methane limitations occurred.

Table 4 provides specifics about the carbon balance, O_2:CH_4 uptake, and total amount of carbon accounted for. For the carbon analysis, only the total carbon (TC) content was considered as this contains both the IC and TOC in samples. With this methodology a consistent carbon balance of $95.3 \pm 1.8\%$ was achieved.

a)

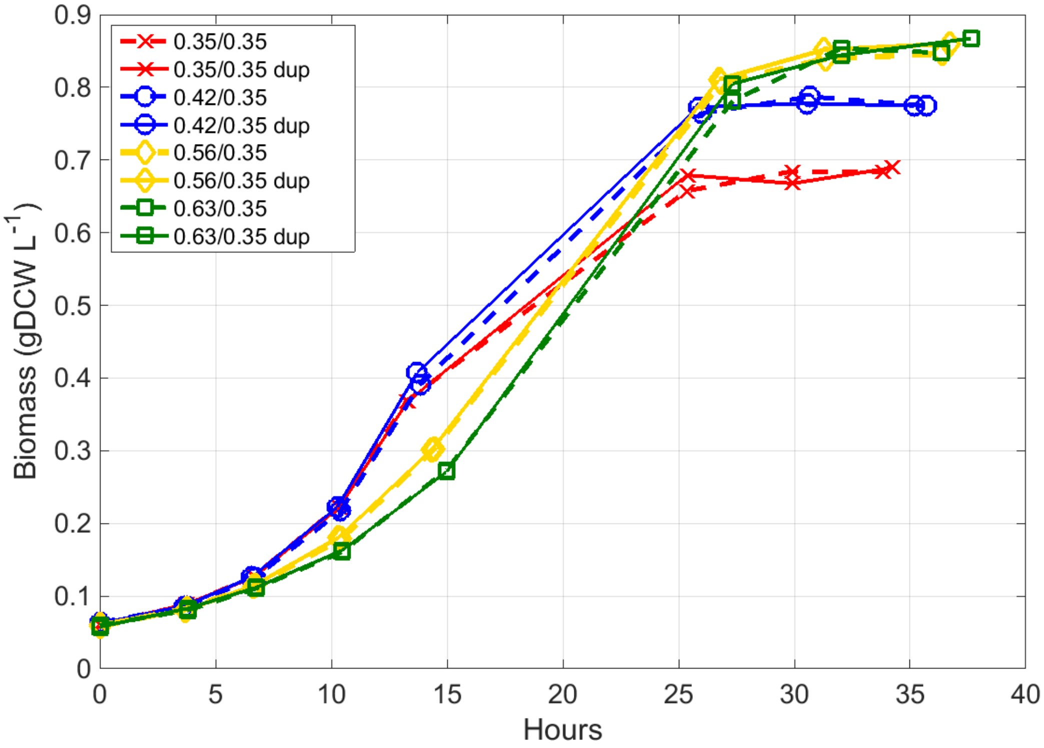

0.35/0.35
0.35/0.35 dup
0.42/0.35
0.42/0.35 dup
0.56/0.35
0.56/0.35 dup
0.63/0.35
0.63/0.35 dup
Biomass (gDCW L-1)
Hours
0
0.1
0.2
0.3
0.4
0.5
0.6
0.7
0.8
0.9
0
5
10
15
20
25
30
35
40

b)

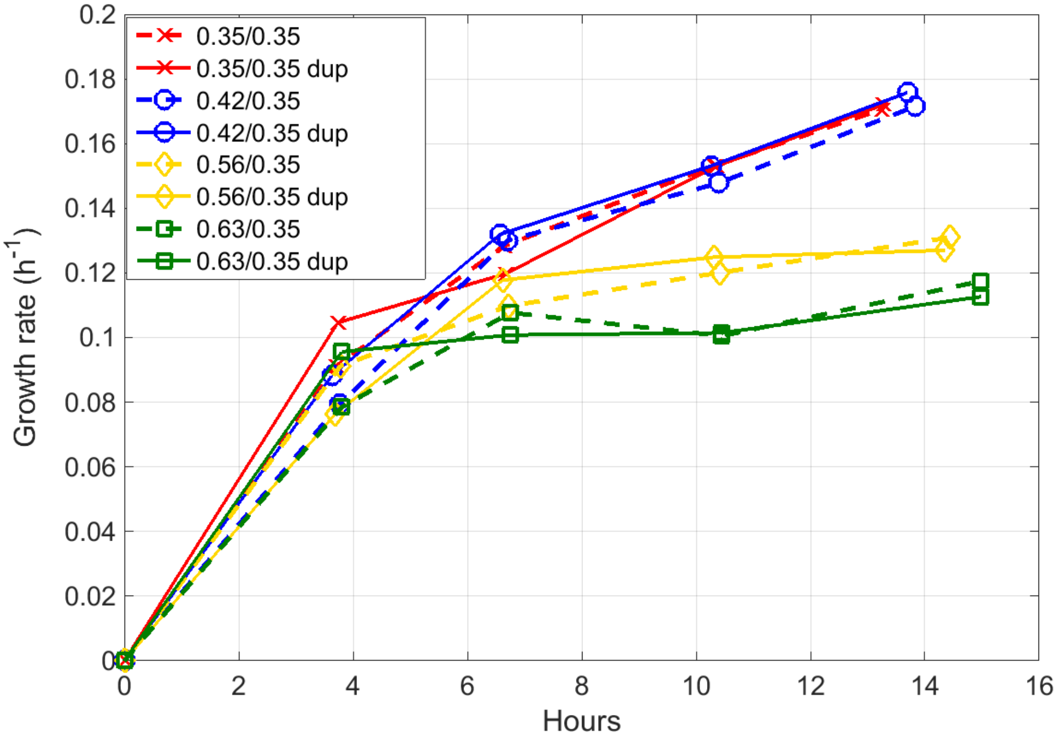

0.35/0.35
0.35/0.35 dup
0.42/0.35
0.42/0.35 dup
0.56/0.35
0.56/0.35 dup
0.63/0.35
0.63/0.35 dup
Growth rate (h-1)
Hours
0
0.02
0.04
0.06
0.08
0.1
0.12
0.14
0.16
0.18
0.2
0
2
4
6
8
10
12
14
16

Figure 16: a) Biomass and b) Specific growth rate for Case 4. The solid and dashed lines amongst the different shapes represent each vial of a duplicate set. The legend is labeled as partial pressure of oxygen over partial pressure of methane fed to the vial.

pO_2	CH_4 consumed	O_2:CH_4 uptake	CO_2 produced	TC	IC	OC	Biomass carbon	% C accounted
0.35	2.04	1.29	0.36	0.72	0.61	0.10	0.93	98.5
0.35 dup	2.03	1.29	0.35	0.65	0.64	0.01	0.93	94.2
0.42	2.41	1.30	0.52	0.73	0.63	0.10	1.04	94.6
0.42 dup	2.44	1.29	0.49	0.74	0.65	0.09	1.06	93.7
0.56	2.66	1.34	0.59	0.73	0.64	0.09	1.15	93.0
0.56 dup	2.67	1.33	0.62	0.81	0.63	0.18	1.16	96.9
0.63	2.63	1.33	0.60	0.74	0.67	0.07	1.16	95.1
0.63 dup	2.65	1.35	0.61	0.76	0.64	0.12	1.18	96.4

Table 6: Carbon analysis of vials with varying headspace conditions for Case 4. Units for pO_2 are in atm. Methane consumed, carbon dioxide produced, TC, IC, OC, and biomass carbon values are all in mmol of carbon.

From Table 6, the O_2:CH_4 uptake ratio were similar and ranged from 1.29-1.35. Furthermore, when comparing the IC and TC content, it is evident that carbonate ions makeup a significant portion of the liquid carbon. Specifically, the IC content made up 78-98.5% of the liquid carbon dependent on the vials final pH. This reaffirms the increased solubility of CO_2 and the need for liquid phase inorganic measurement for an accurate carbon balance.

The yields of three main products were calculated: biomass (Y X/S), CO_2 (headspace concentration + IC as Y CO_2/S), and liquid organic carbon (Y OC/S). Organic carbon was not further analyzed, but is assumed to be composed of the extracellular polysaccharides (EPS) or organic acids produced during growth [118] or if/ when oxygen is severely limited sparking fermentation pathways [66]. The yields of Case 4 are displayed in Figure 17 and it is apparent that carbon dioxide and biomass yields make up the largest portions of carbon consumed. Amongst all the headspaces, Y X/S and Y CO2/S remained relatively constant with average values of 0.463 ± 0.009 and 0.498 ± 0.012, respectively. The Y OC/S, however, varied amongst all vials (0.01-0.07 mol C/mol CH_4) with no clear pattern.

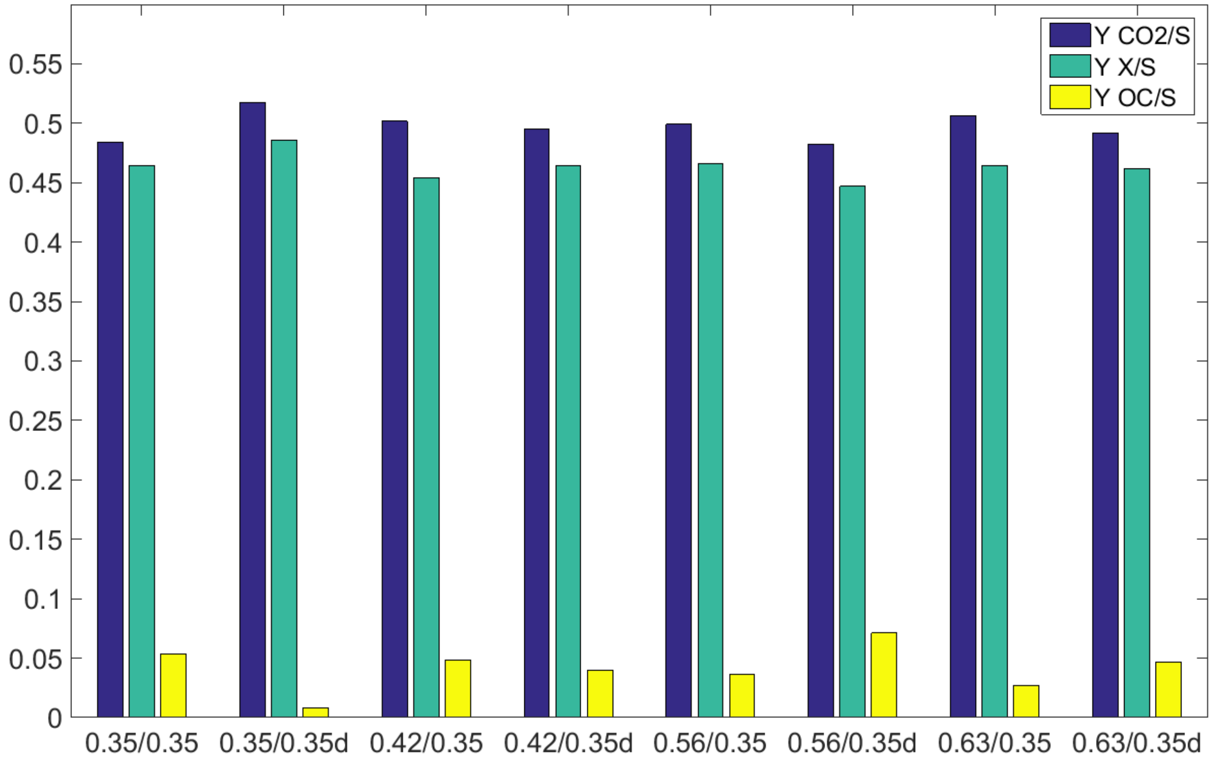

Figure 17: Yields to carbon dioxide (CO_2), biomass (X), and organic carbon (OC) of the different vials tested for Case 4. Yields are mmol C/mmol CH_4 consumed.

Case 5 was designed as second trial to evaluate the carbon distribution for a set methane condition with various oxygen concentrations. Cell growth is exhibited in Figure 18a, while the specific growth rates (calculated by Equation 9) for the first day of sampling is shown in Figure 18b. Vials with pO_2 of 0.2 atm attained peak specific growth rates of 0.153 h^{-1}, while those with pO_2 of 0.4 atm achieved 0.147 h^{-1}. Vials with pO_2 0.6 atm experienced a slower growth rate with an average peak growth rate of 0.12 h^{-1}. Interestingly, after a peak growth rate of 0.087 h^{-1}, the vials with a pO_2 of 0.8 atm, grew at in a linear fashion for almost 24 hours till the experiment was ceased. During this growth the overall organic carbon continued to increase from levels of <25 mg C L^{-1} (as experienced by the other vials) to levels of 145-160 mg C L^{-1}.

As observed beforehand, the vials with larger oxygen supply fallowed for nearly complete consumption of methane (see Table 7) and thus achieved higher cell density. The exception being pO_2 0.8 vials where carbon was distributed to organic products rather than biomass. The final average cell density amongst duplicates for pO_2 of 0.2, 0.4, 0.6, and 0.8 atm were 0.41, 0.51, 0.50, and 0.42 g DCW L^{-1}, respectively.

a)

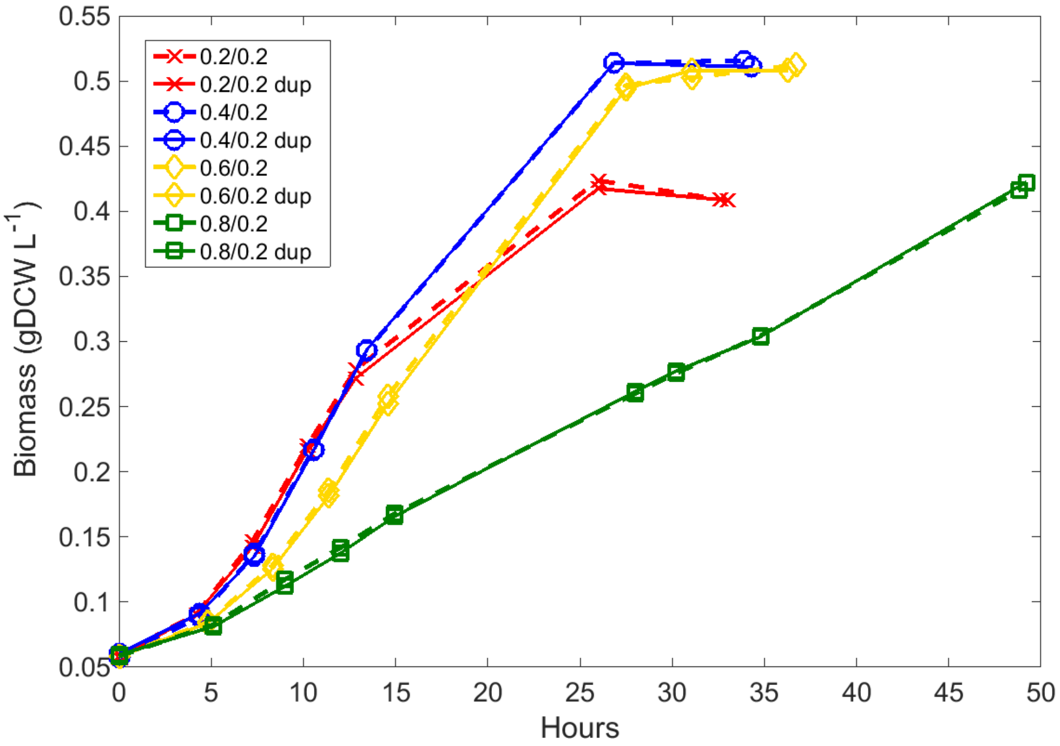

b)

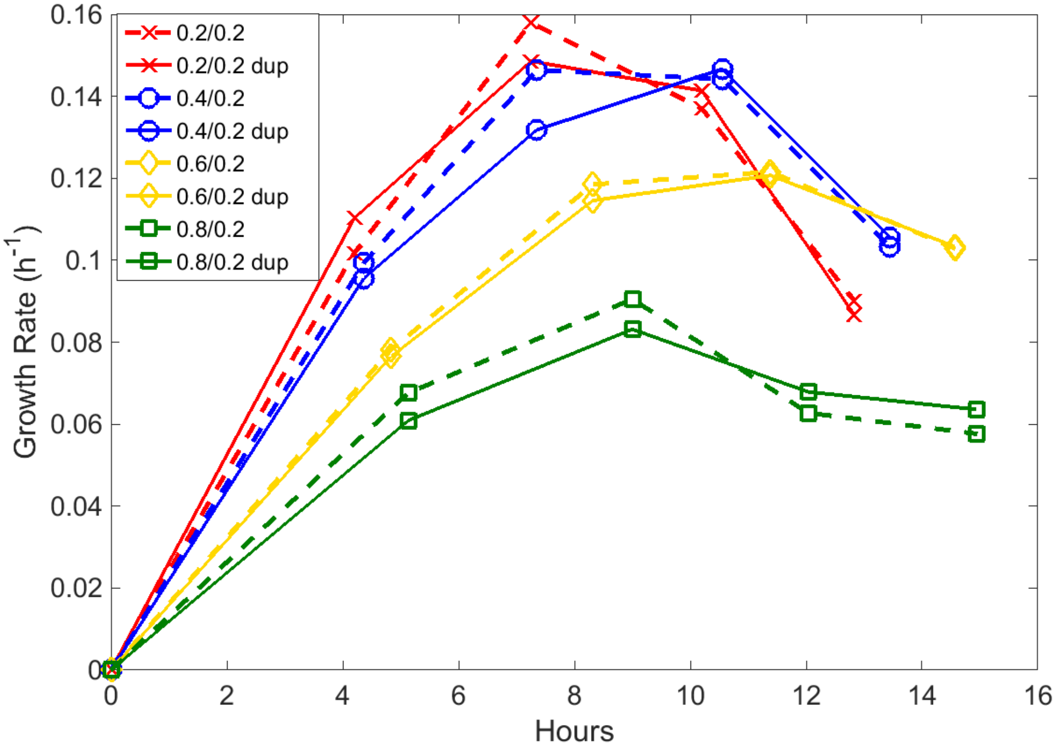

Figure 18: a) Biomass and b) Specific growth rates for Case 5. The solid and dashed lines amongst the different shapes represent each vial of a duplicate set. The legend is labeled as partial pressure of oxygen over partial pressure of methane fed to the vial.

pO_2	CH_4 consumed	O_2:CH_4 uptake	CO_2 produced	TC	IC	OC	Biomass carbon	% C accounted
0.2	1.17	1.23	0.09	0.55	0.52	0.03	0.55	101.6
0.2 dup	1.18	1.26	0.09	0.53	0.51	0.02	0.56	99.8
0.4	1.53	1.31	0.18	0.64	0.61	0.04	0.70	100.1
0.4 dup	1.53	1.31	0.19	0.63	0.58	0.05	0.70	99.2
0.6	1.53	1.30	0.21	0.61	0.58	0.04	0.69	99.0
0.6 dup	1.53	1.32	0.20	0.59	0.57	0.03	0.69	97.1
0.8	1.49	1.38	0.34	0.63	0.22	0.40	0.48	97.3
0.8 dup	1.47	1.43	0.34	0.61	0.17	0.44	0.47	96.4

Table 7: Carbon analysis of vials with varying headspace conditions for Case 5. Units for pO_2 are in atm. Methane consumed, carbon dioxide produced, TC, IC, OC, and biomass carbon values are all in mmol of carbon.

The uptake ratio of O_2:CH_4 remained relatively similar to the previous case, with values falling between 1.23-1.32. A slight increase in uptake was observed with the highest oxygen partial pressure with values of 1.38 and 1.43. Additionally, the inorganic carbon in the liquid phase for sets between pO_2 0.2-0.6 atm made up a significant portion of the total liquid carbon (>90%) that again demonstrates the necessity of inorganic liquid carbon measurement.

The yields for pO_2 0.2-0.6 atm demonstrated constant values with Y X/S, Y CO_2/S, and Y OC/S, averaging 0.463 ± 0.006, 0.514 ± 0.004, and 0.024 ± 0.006, respectively (see Figure 19). These yields are similar to those in Case 4, demonstrating a general consistency of the carbon distribution by the cells regardless of any substrate limitation. Vials in pO_2 0.8 atm, however, had a significant difference in yields of all components with a Y X/S, Y CO_2/S, and Y OC/S averaging 0.334, 0.373, and 0.293, respectively. Due to the large presence of oxygen in these vials, it is assumed that most of the organic carbon is associated with EPS. EPS production at elevated oxygen levels has been observed before and is associated with a mechanism to alleviate stress due to do the excess oxygen concentrations [119,120]. EPS also has been known to affect gas diffusion from the headspace to the cells, thus explaining why a consistent, low growth rate was observed [120].

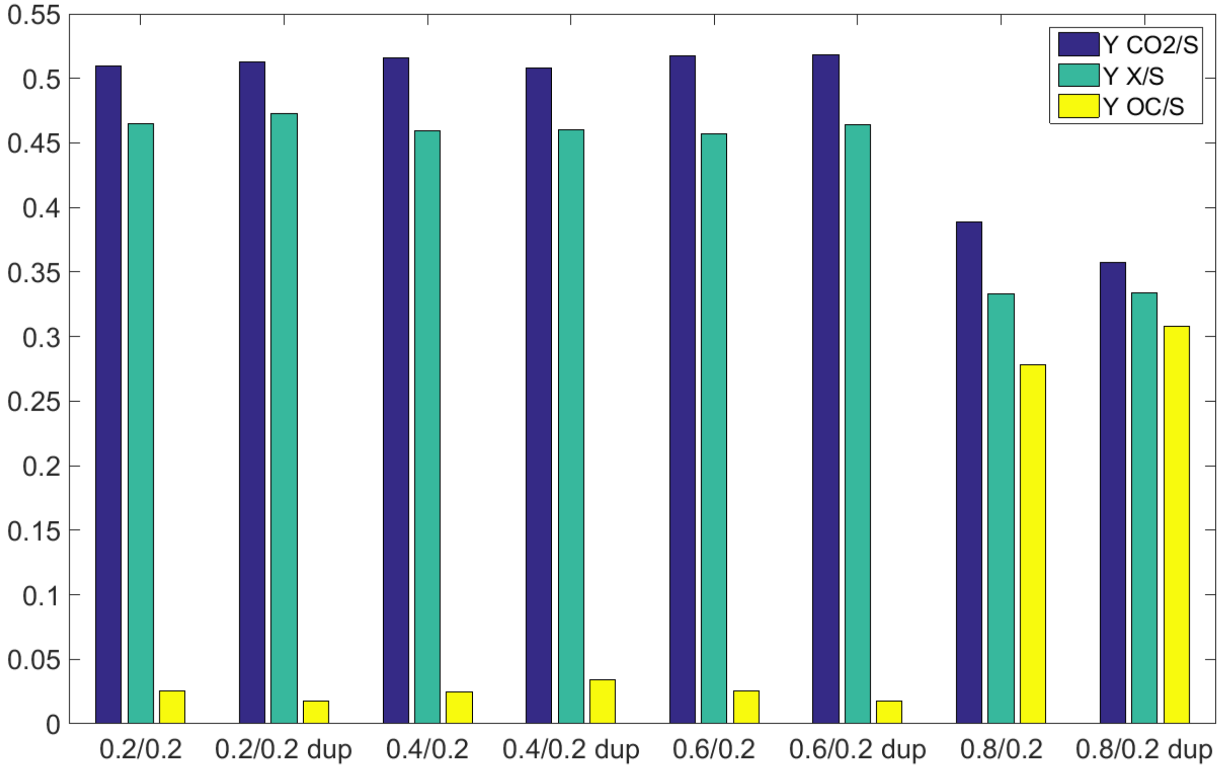

Figure 19: Yields to carbon dioxide (CO_2), biomass (X), and organic carbon (OC) of the different vials tested for Case 5. Yields are mmol C/mmol CH_4 consumed.

4.6 Discussion of Case Studies

The above case studies highlighted the clear effect of oxygen concentration on the growth rate of the pure culture of *M. buryatense*, regardless of the amount of methane present. From Cases 3-5 growth rates above pO_2 of 0.4 atm experience noticeable growth inhibition. This behavior continues to deteriorate with increase oxygen presence to a point in which the cells change phenotype completely and produce significant amounts of organic liquid carbon.

Oxygen has been identified as an influential factor for methanotrophs within previous published research. The gas not only affects the growth rates of certain species but can alter whole methanotroph consortiums in landfills and applied biofilters that in turn may affect methane oxidation rates [121–124]. In pure culture studies, Ren et al. demonstrated that with oxygen concentrations above 20% v/v a general decrease in methane oxidation is experienced with *Methylobacter luteus* and *Methylosinus trichosproium*. Specifically, at 60% v/v of oxygen an average 23% inhibition of methane consumption occurs for both organisms [122].

Carbon conversion efficiencies (CCE) is defined as the total amount of carbon to organic liquid components and biomass. In this study, CCE remained relatively constant in the trials regardless of oxygen content till pO_2 of 0.8 atm. The cultures typically distributed half of the carbon to CO_2 and the other half to biomass and organic liquid products. At the pO_2 0.8 atm, the carbon conversion increased to >60% that directed almost evenly towards organic carbon and to biomass. These values are comparable to what Gilman et. al. reported, where their CCE for oxygen limited and methane limited cultures were 43-46% and 54-61%, respectively [36].

4.7 Conclusions of Systematic Approach

Several key conclusions were found in this chapter: 1. Growth was affected by the presence of oxygen over a critical amount (pO_2 of 0.4 atm for the vial cultures). 2. An accurate carbon balance (average >95%) was conducted due to re-pressurization of vials and accounting for the carbon dioxide salts within the liquid phase. 3. Carbon dioxide accounts for a predominant amount of carbon in the liquid phase under most conditions due to the chemical equilibrium of carbonate/bicarbonate. 4. Yields to carbon dioxide, biomass, and organic carbon were relatively constant until oxygen presence caused a change in phenotype behavior and created significantly larger amounts of EPS.

This data adds to the foundation required to evaluate *M. buryatense* as an environmental and industrial biocatalyst. Insight on the metabolic shift caused by oxygen growth inhibition requires further study. Any knowledge gained will allow for efficient genetic manipulation of this promising microbe and in turn, further develop a process that produces sustainable energy while reducing green gas emissions.

Chapter 5 : Gas and Carbon Analysis of *M. buryatense* 5GB1 in a Continuous Chemostat

5.1 Brief Considerations and Theory for Methane Fermentation

Gas transfer into the liquid phase of a chemostat originate from two main sources: the bubble sparged and the gas accumulated in the headspace of the reactor [75]. Due to low cell concentrations, relative to cultures dependent on liquid substrate (such as glucose fed to yeast), and higher interfacial surface area of the bubble, it can be assumed that the transfer of gas is predominantly from the bubble. In doing so, the gas transfer rate of the substrate for both methane and oxygen can be described by the traditional equations:

$$OTR = \frac{dC_{L_{O2}}}{dt} = k_L a_{O2} * \left(H_{O2} C_{b_{O_2}} - C_L\right) \quad \textbf{(11)}$$

$$MTR = \frac{dC_{L_{CH4}}}{dt} = k_L a_{CH4} * (H_{CH4} C_{b_{CH_4}} - C_L) \quad \textbf{(12)}$$

In these expression, OTR and MTR stand for oxygen and methane transport rate, respectively. The term C_L, refers to the dissolved concentration of the gas species, C_b, the bubble concentration of the gas species (as dictated by the flow rates in the mixing system), H, the Henry's constant of the species, and finally $k_L a$, the volumetric transfer rate of the species. As discussed in Chapter 1, the volumetric transfer rate is highly dependent on bioreactor type. For

STR the most influential factors for optimal gas transfer include, gas flow rate, sparger type, agitation rate, and cell density [73,75]. Equations 11 and 12 can be compressed into one by relating the volumetric transfer rate of methane to oxygen. For this experimental plan, the relationship by Yu et. al. was utilized where $k_La_{CH4} = 0.855k_La_{O2}$. In doing so, Equation 13 can be formed

$$\frac{OTR}{MTR} = \frac{1}{0.855} * \frac{H_{O2}y_{O2}}{H_{CH4}y_{CH4}} \tag{13}$$

The concentration of the individual gas species can be broken down to the molar fraction,y, since the gasses are introduced together to the bioreactor at a constant gas flow rate. Using $1.4 * 10^{-5}$ and $1.3 * 10^{-5}$ mol (m^{-3}* Pa^{-1}) as Henry constants for methane and oxygen, respectively, and the known gas concentration in the feed, the overall transfer rate to cells can be calculated [115]. It should be noted that the above equation is for approximation for experimental planning. Factors with the bioreactor design, gas accumulation, and specific cellular uptake can have a significant effect on this estimated transfer ratio.

From the classic work of Schill et. al. that described the fundamental behavior of gas fermentation units, a few considerations were to be expected during the continuous cultivation of methanotrophs [125]. For methanotrophs it can be expected that either oxygen or methane or even both substrates would be the limiting agent for growth. Since it would be a gaseous substrate that affects growth, the transfer rate is almost completely independent of dilution rate. Thus the following would be expected: (1) The gas uptake rate (mmol h^{-1}) would remain constant over the tested dilution rates as uptake rate would always be equivalent to the much slower transfer rate; (2) The biomass concentration decreases with increasing dilution rate as cellular pickup would increase but the gas transfer would not (referring to previous point); (3)

The specific gas pickup rates (mmol g DCW^{-1} h^{-1}) would increase with increasing dilution rates as transfer remains constant (rule 1) and fewer cells are present for consumption (i.e., rule 2).

This behavior is quite different from cultures fed with a substrate in the liquid phase, such as glucose to *E. coli* or yeast. With liquid phase bioreactors, the substrate conversion rate (mmol h^{-1}) increases with dilution rate in a proportional format (transfer rate α uptake rate). In doing so, the biomass does not drop in typical liquid substrates but rather grows or stays constant [125].

5.2 Objective of the Study and Experimental Set Up

Utilizing the analysis structure from the vial experimentation, chemostat experiments were conducted to: (1) confirm that a complete carbon analysis could be done, (2) maintain steady state with consistent pickup/production rates, and (3) determine how cell behavior changes with methane deprived and oxygen deprived settings. Utilizing the concepts covered in Chapter 3 Section 6 with helium as an internal standard to measure effluent flow rate, two case studies were completed. Case 1 will cover how objectives (1) and (2) were successfully completed, while Case 2 expands on the success of Case 1 into several more steady state conditions within the same bioreactor run.

All continuous cultures presented here utilized either the Eppendorf Bioflo 110 or 115. The reactor vessel was 3 L with 1.5 L of liquid volume and contained the standard baffles were placed within the vessel. Agitation was kept at 500 rpm to avoid any over-agitation affects while also maximizing the rotational bubble flow for efficient gas transfer (see Figure 20). The gas mixing system delivered a consistent flow of 300 smL min^{-1} through a microsparger to create smaller bubbles and enhance substrate transfer. Any increase or decrease in oxygen levels were accompanied by an equivalent but opposite change to nitrogen to maintain the same flow rate. The exhaust gas was passed through a condenser kept at 5 ^{o}C that was cooled continuously via recycled water. A gas sample port was installed in the effluent stream for GC measurement. The temperature of the gas was measured via the online probe/software made by Vernier Software and Technology.

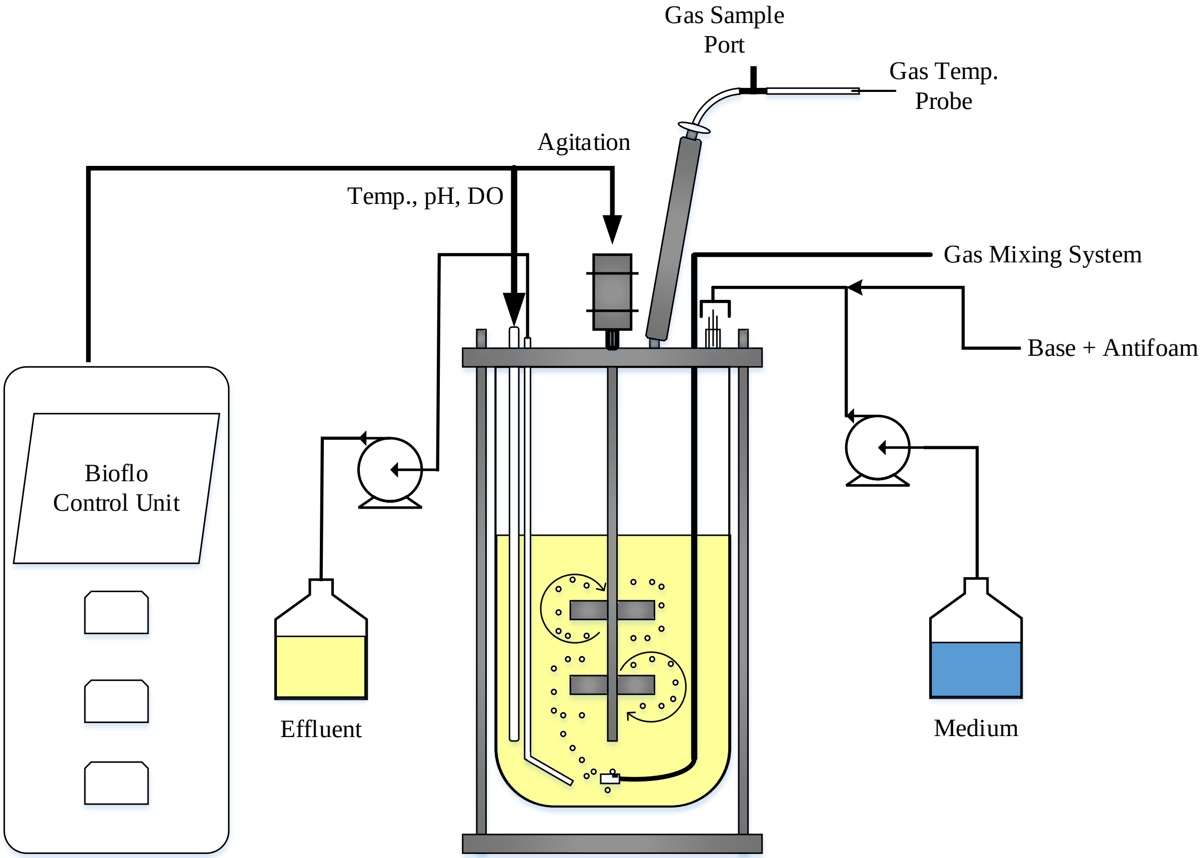

Figure 20: Continuous chemostat for methane bioconversion. Redrawn and adapted from [126]. Unit displayed here is not drawn to scale.

The Bioflo unit maintained temperature at 30°C and pH at 9 via addition of 4 M NaOH. For all cases, Struktol J 660R was used as antifoam and is a mixture of vegetable fatty acid and ethylene oxid / propylene oxide blockpolymers. Antifoam in Case 1 was added intermittenly via manual injection while the antifoam was pumped in with New Era syinge pump at 18 µL h^{-1} to 24 µL h^{-1} in Case 2. For the carbon balance to be accurate, the carbon in the antifoam (almost completely organic carbon) was measured to be approximately 485,000 mg C L^{-1}.Thus, the inflow of organic carbon can be calculated and accounted for in carbon canalysis.

The initial medium inside the bioreactor was similar to the standard NMS2 medium with all associated buffers, except with a larger concentration of nitrate (2x) and trace element solution (2x). These two components were concentrated so that carbon was not forced towards organic acid production due to nitrogen or microcompoenent limitations [32,67]. The medium fed into the reactor for steady state conditions also contained double the nitrate (unless stated otherwise) and trace concentration, but excluded carbonate buffer, as the pH was maintained via the bioflo unit. This means that initially the carbon balance is affected by the buffer till the continuous system allows for it to be washed out.

Two rounds of pre-culture are conducted to obtain the initial inoculum to the bioreactor. The first round is inoculated via cells grown on medium plates. These cultures are allowed to grow to mid-exponential growth phase within vials that have an initial headspace of 1:1 O_2:CH_4 and standard NMS2 medium. The second round is inoculated from selected vial that show the best growth in headspace of ~0.9:1 O_2:CH_4 with NMS2 medium supplemented with 2x nitrate. The cells are inoculated early in the day and are re-fed again at night. The purpose of the second round is to solely accumulate enough biomass so that the cells can handle the large exposure of oxygen in the bioreactor. This inoculum to DO ratio was observed to be extremely influential, as shown in the results discussed in Appendix A.

Initially the bioreactor is operated as a batch culture on the day of inoculation to allow for a maintainable accumulation of biomass. On the following day, the system becomes continuous mode via powering on the inlet and outlet pumps.Samples are taken 4-5 times a day during the bioreactor run through the day (morning, noon, early and late afternoon, and night). The sample process is summarized as follows. After recording flow rates and bioflow control units (temperature, dissolved oxygen, agitation, and pH), manual gas samples are taken to both the Agilent and SRI GC systems from the gas port. A liquid sample is taken to wash out the sample line and discarded. A subsequent sample is taken to measure OD with appropriate dilutions. Any unused sample is centrifuged and filtered for TC/IC analysis and to measure formate concentration via Agilent 1200 series high performance liquid chromatography (HPLC) equipped with an RID and MWD. Formate was analyzed on an Aminex HPX-87H column (Bio-Rad, Hercules, CA, USA) at 35°C with 0.05 N H2SO4 solution as the mobile phase tat was pumped at a flow rate of 0.6 mL/min. The injection was 100 µL and peakwidth set at 0.4 min (8 s, slow). Calibration curves were generated with the appropriate concentration of sodium formate. No other component was measured via HPLC as formate is the largest organic acid produced from this methanotroph during growth and acetate's peak was continuously interfered with by other liquid components [36].

5.3 Carbon and Growth Analysis of a Chemostat without Helium as a Tracer

To conduct an effective carbon balance, the molar flow rate of the effluent stream leaving the condenser must be accurately measured. In the first attempt of the continuous reactor run, a nitrogen balance was conducted based off the measurements of the other components of the gas stream: oxygen, methane, and carbon dioxide (see Equations 14 and 15). Recall, that nitrogen is the carrier gas for the Agilent GC system and thus, nitrogen itself cannot be directly measured. Due to the poor solubility of the gas and the abundance of nitrate in the system, it was thought the component would remain relatively unbothered throughout the run.

$$y_{N_{2out}} = 1 - y_{CH_{4out}} - y_{O_{2out}} - y_{CO_2} \quad \textbf{(14)}$$

$$F_{in} * y_{N2_{fed}} = F_{out} * y_{N2_{out}} \quad \textbf{(15)}$$

As with helium in Chapter 3 Section 6, the inflow of nitrogen is fixed via the mass flow rate of the mixed gas system. With simple mathematics the gas flow out could be found and a carbon balance completed. For the initial analysis, the temperature of the effluent was thought to be typical room temperature of 25 °C. Especially since the residence time of the gas in the reactor held at 30°C and the condenser held at 5°C was relatively short compared to the residence time in the tank stored within the room. The results of the growth and carbon balance for this first chemostat run are illustrated in Figure 21 and 22.

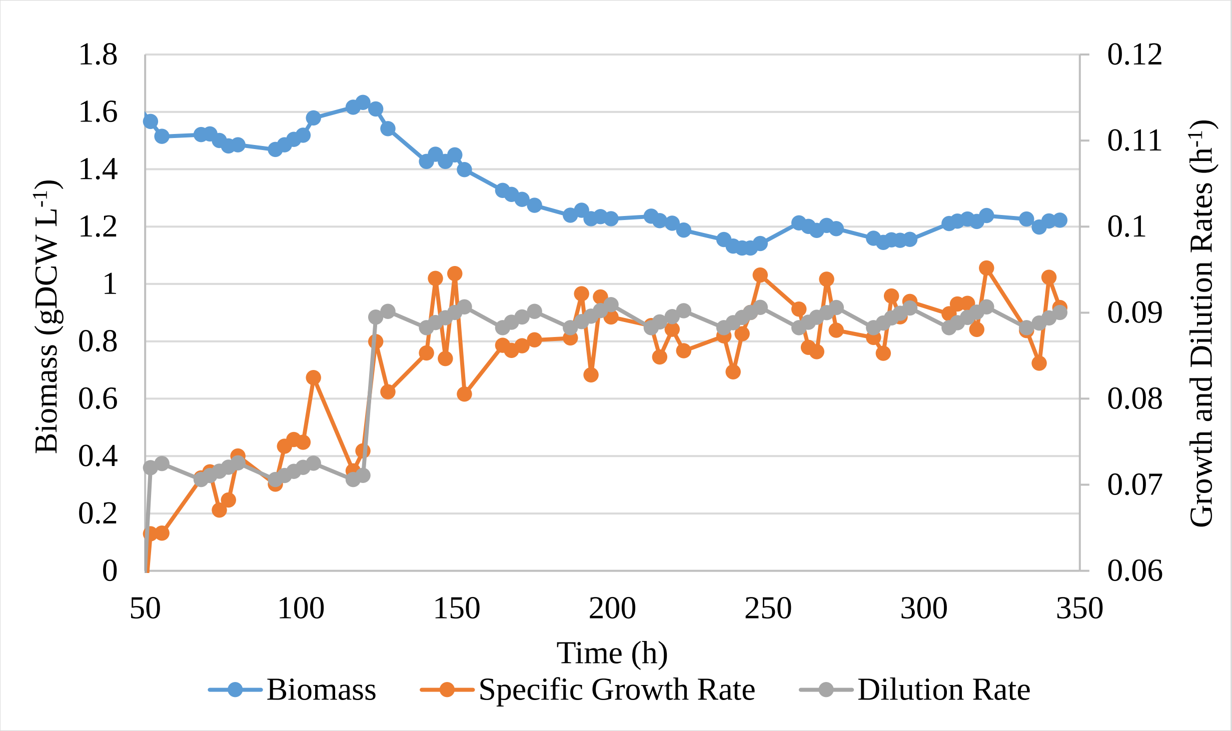

Figure 21: Cell density and the accompanying specific growth gate at tested dilution rate

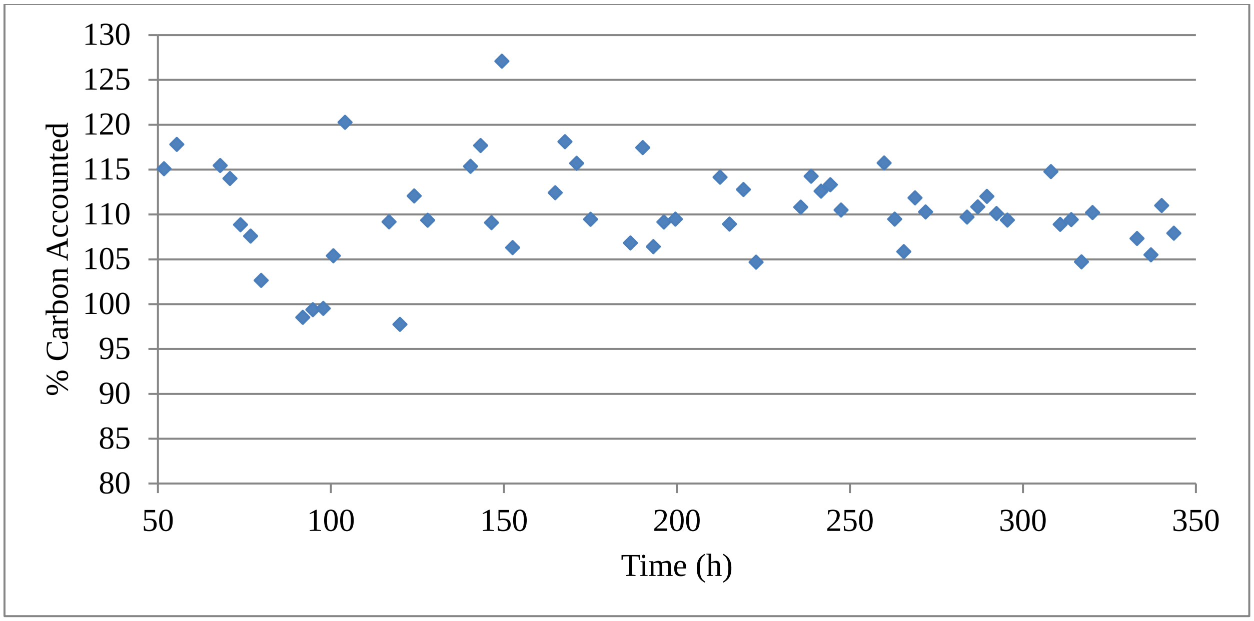

Figure 22: Carbon balance for chemostat where flow rate is calculated via nitrogen balance

As the cells reached a steady state starting at about 220 hours, the carbon balance narrowed to a range of 105-115%. To evaluate whether outlet temperature was behind this inflated amount of carbon, the temperature was altered for Equation 7 for each gas component measured and the carbon balance calculated again. The results for a few points are displayed in Table 8.

Sample Hour	25 C	23 C	21 C
259.8	115%	111.4%	107.3%
262.9	109.5%	105.4%	101.7%
265.6	105.9%	101.9%	98.3%

Table 8: Effects of temperature on the carbon balance for three time points.

From the above table it is apparent that the assumed temperature value has a significant impact on the carbon balance due to how effluent flow rate is calculated. Specifically, each change in temperature affects the mole fraction of the measured components and in turn, the concentration of nitrogen used in the above flow rate calculation. To avoid this compounded error from gas measurement and that created from temperature assumption, an online temperature probe was installed and helium was used as a tracer to measure flow rate (see Chapter 3 Section 6).

5.4 Case 1: Obtaining an Accurate Carbon Balance of Methanotroph Chemostat

After establishing that a nitrogen balance was not utilized satisfactorily to measure the effluent flow rate, helium was continuously fed into the system. The gas composition for this was constant throughout with 14%, 11.67%, 64.3%, and 10% (v/v) for CH_4, O_2, N_2, and He, respectively. Utilizing Equation 13 the expected OTR/MTR is 0.91, which is under the 1:1 ratio needed for oxidation of methane and purposely depletes the additional oxygen required for aerobic respirations. Thus, the system was run at an oxygen depleted state for a complete carbon analysis, the equations of which are covered in Appendix B.

With helium as an internal standard, the carbon balance amongst the three groups of steady state data averaged between 101.3-103.7% (illustrated in Figure 23 and Table 9). Thus, the predicted flow rate with the tracer has allowed for a complete balance. This flow rate can be double checked via a partial carbon balance by only considering carbon in biomass and from liquid phase (TC measurement). Due to the alkaline pH, the CO_2 in the headspace was fairly dilute (between 0.2-0.3% of the effluent gas) and represents a small portion of all carbon. With that in mind, a rough calculation of the expected flow rate from the carbon in liquid products could be produced. As demonstrated in Figure 24, the calculated flow rate from the carbon products remained relatively close to the flow rate derived from the helium balance, with less than 3% difference. This difference however is significant, because the calculated flow rate form liquid products is consistently higher than the estimate flow of gas into the bioreactor. Meanwhile, the flow rate via helium balance was consistently lower than the flow rate in, as expected in a system with continuous consumption.

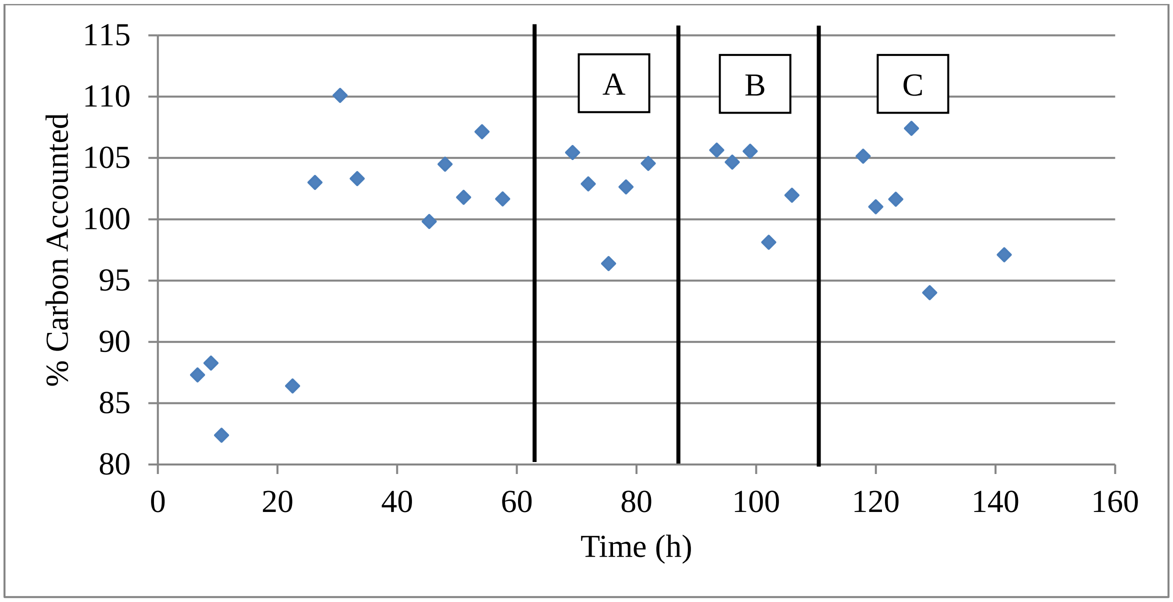

Figure 23: Carbon balance for chemostat Case 1.

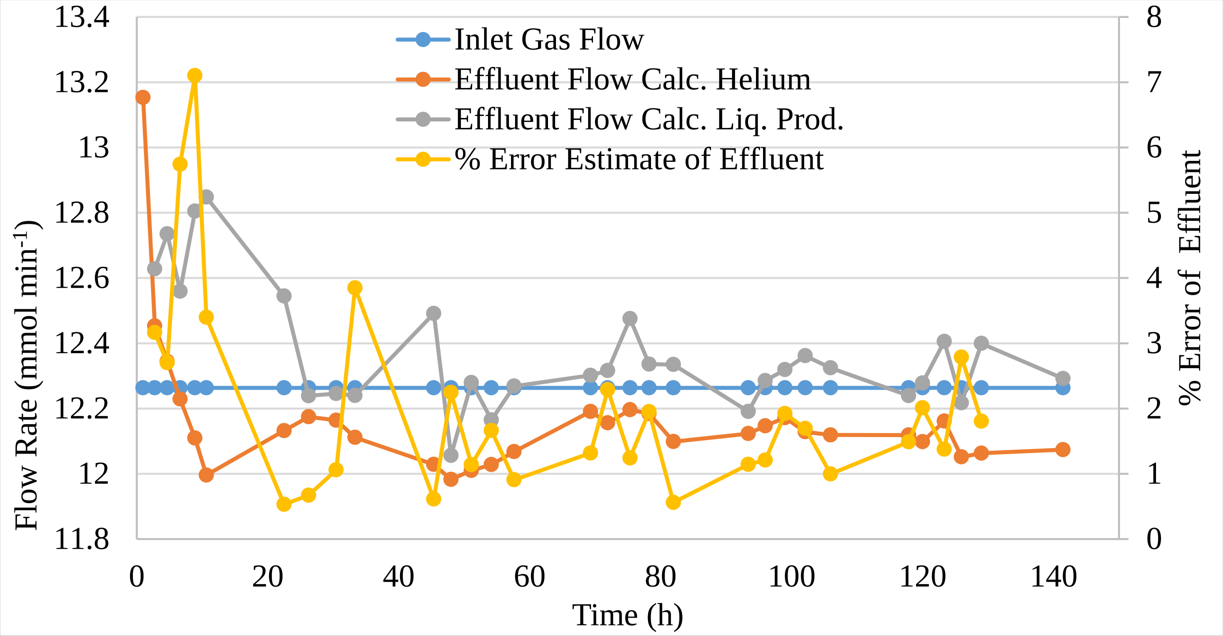

Figure 24: Calculated flow rate from the effluent stream of the chemostat for Case 1.

Due to the confidence in the carbon balance, steady state values were found for biomass accumulation, gas pickup rates, and CO_2 production rates. Steady state was defined by data sets within time spans that experience less than 10% deviation in biomass, gas pickup rates, and production rates. For this study, biomass reached levels of 1.15 g DCW L^{-1} on the 3rd day of the experiment and remained at that concentration till the experiment was ceased (Figure 25). Due to the consistent gas transfer and biomass, the specific methane and oxygen pickup rates were also relatively constant (Figure 26). It should be noted that the noticeable increase in methane and oxygen pickup between hours 123-125 is usually observed after antifoam is added manually. This rapid momentary enhancement is possibly due to a liquid vector effect where methane and oxygen are more soluble in the heavy organic phase than water. Such vectors have been covered in Chapter 1 Section 4.

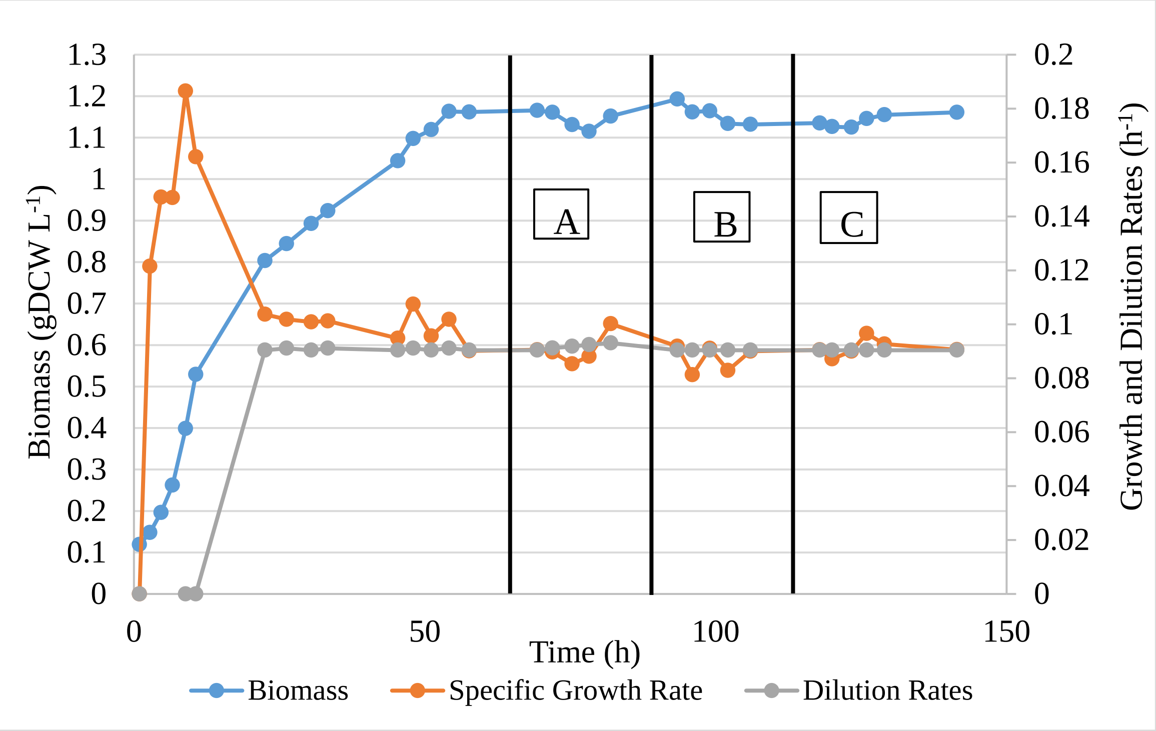

Figure 25: Cell density and specific growth rate for the set dilution rate for chemostat Case 1.

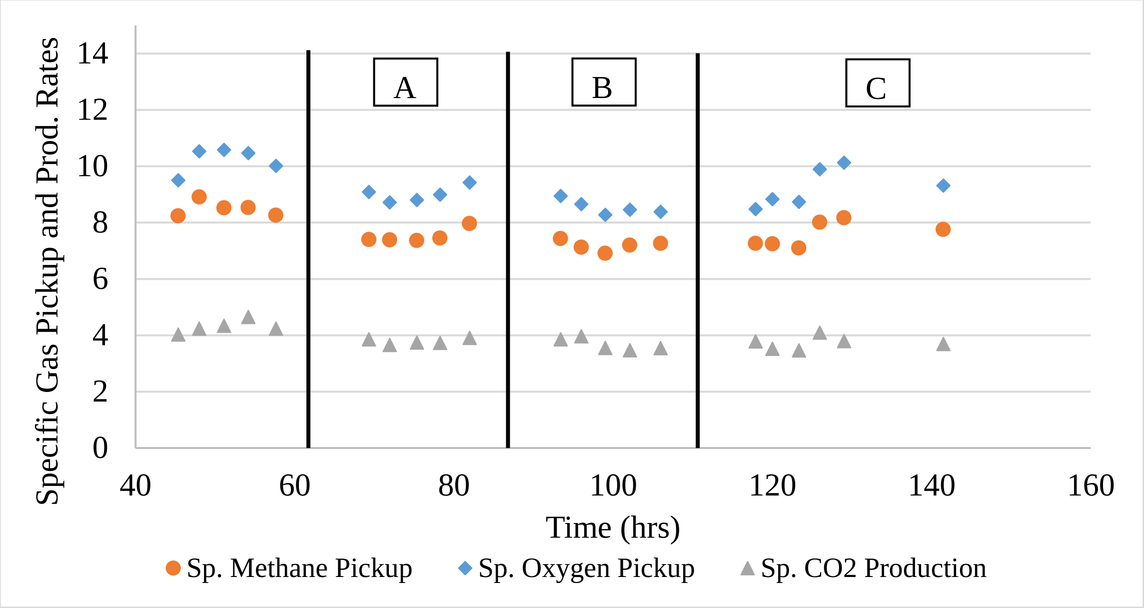

Figure 26: Specific gas pickup and production rates for chemostat Case 1. The units for the rates are in mmol gDCW^{-1} h^{-1}.

a)

Set	Hours	Methane Pickup	Oxygen Pickup	O_2:CH_4 pickup	CO_2 Production	Formate Production
A	69-82	7.51 ± 0.25	9.00 ± 0.28	1.20 ± 0.02	3.78 ± 0.10	0.004 ± 0.001
B	94-106	7.19 ± 0.19	8.54 ± 0.26	1.19 ± 0.02	3.68 ± 0.22	0.004 ± 0.001
C	118-142	7.59 ± 0.45	9.23 ± 0.67	1.22 ± 0.03	3.73 ± 0.23	0.004 ± 0.001

b)

Set	Hours	Biomass (gDCW L^{-1})	Growth Rate (h^{-1})	Carbon Balance	Y CO_2/S	Y X/S	Y OC/S
A	69-82	1.15 ± 0.02	0.091 ± 0.005	102.4 ± 3.5	0.492 ± 0.022	0.464 ± 0.009	0.044 ± 0.025
B	94-106	1.16 ± 0.02	0.088 ± 0.004	103.2 ± 3.2	0.496 ± 0.020	0.464 ± 0.024	0.040 ± 0.010
C	118-142	1.15 ± 0.01	0.091 ± 0.003	101.1 ± 5.0	0.486 ± 0.008	0.469 ± 0.016	0.045 ± 0.020

Table 9: Chemostat case 1 steady state data a) Gas pickup, production, and formate in units of mmol gDCW^{-1} h^{-1}. b) Biomass, carbon balance, and growth rates. Yields are mmol C/mmol CH_4 consumed with X as biomass and OC as organic carbon.

From the above tables, the average methane and oxygen pickup rates fluctuated from day to day, though less than 10% as needed for steady state condition. Additionally, a large standard deviation is seen in the third day probably due to the effects seen with manual injection of antifoam. Despite this variability, the overall ratio was relatively consistent at approximately 1.20, the same value found in the oxygen limited sets Gilman et al achieved [36]. Formate production varied considerably throughout the run as concentrations ranged between 35-85 µmol L^{-1} (or 33-70 µmol gDCW^{-1}). This large irregularity could again be due to the manual injection of antifoam. With antifoam additions, a small jump in cell growth was observed that in turn was accompanied by a formate production increase. Regardless of the variability, the formate concentration observed here is significantly lower than those overserved in other studies where the production was well over 200 µmol gDCW^{-1} [36]. From literature, formate production is thought to be caused by a redox imbalance where NADH abundance leads to excess carbon heading towards organic acid production. In this case however, formate production is low and carbon yields to organic components is approximately 4-5%. From Table 9, the carbon converted to biomass stayed between 46-47%, creating a carbon conversion efficiency of 53-54% that is noticeably larger than the oxygen limited sets from previous studies that reported efficiencies of 43-46% [36].

5.5 Case 2: Expansion of Carbon Balance to Methane and Oxygen Depleted States

With the demonstrated success of utilizing helium to measure the effluent gas stream and in turn, obtain an accurate carbon balance, another chemostat run was designed with various dilution rates and oxygen levels. As exhibited in Table 10 and Figure 27, the reactor underwent six experimental conditions with three different dilution rates and two different oxygen levels. Methane and helium were kept at constant levels throughout the test at 14% and 10% of the 300 smL min^{-1} feed, respectively. Utilizing Equation 13, oxygen levels were created to have solely methane (ratios of 1.80) or oxygen limitation (ratios of 0.95). From Figure 27, it can be seen that between conditions either the dilution rate or the headspace is altered and not both. This was to avoid any unnecessary stress and washout of the cells caused by changing both conditions simultaneously.

	Condition 1	Condition 2	Condition 3	Condition 4	Condition 5	Condition 6
Dilution rate (h^{-1})	0.085	0.085	0.105	0.105	0.121	0.121
DO expected	~0	5-7	5-7	~0	~0	5-7
Oxygen flow rate	35	70	70	35	35	70
Methane flow rate	42	42	42	42	42	42
OTR/MTR	0.95	1.80	1.80	0.95	0.95	1.80

Table 10: Experimental plan for chemostat Case 2

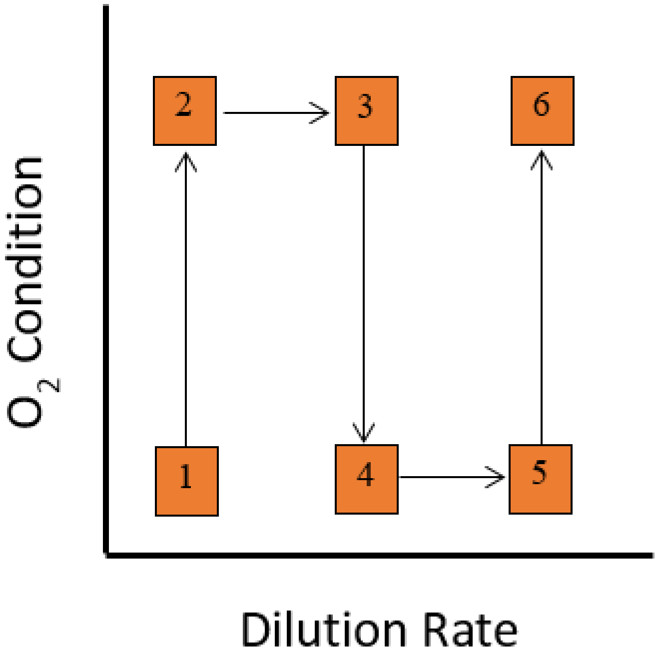

Figure 27: Illustrative schematic of experimental design for chemostat Case 2

Upon starting the experiment, a series of unfortunate events caused a delay in applying condition 1 fully. Firstly, the TC areas measured from samples became inconsistent and ranged with errors over 100%. This was fixed after installing new catalyst and adjusting the injection tube. Antifoam was inputted constantly with a syringe pump to avoid the random intervals of enhanced pickup rates. A power loss caused the solenoid valve to close the methane line for twenty minutes, causing >10% biomass drop. Finally, the inlet tube became clogged, causing a significant problem when keeping constant volume and thus had to be replaced. Throughout this delay however, cell growth was maintained and medium continuously fed. Upon doing so, condition 1 was finally applied after 450 hours. The overall biomass growth from that point on is shown in Figure 28.

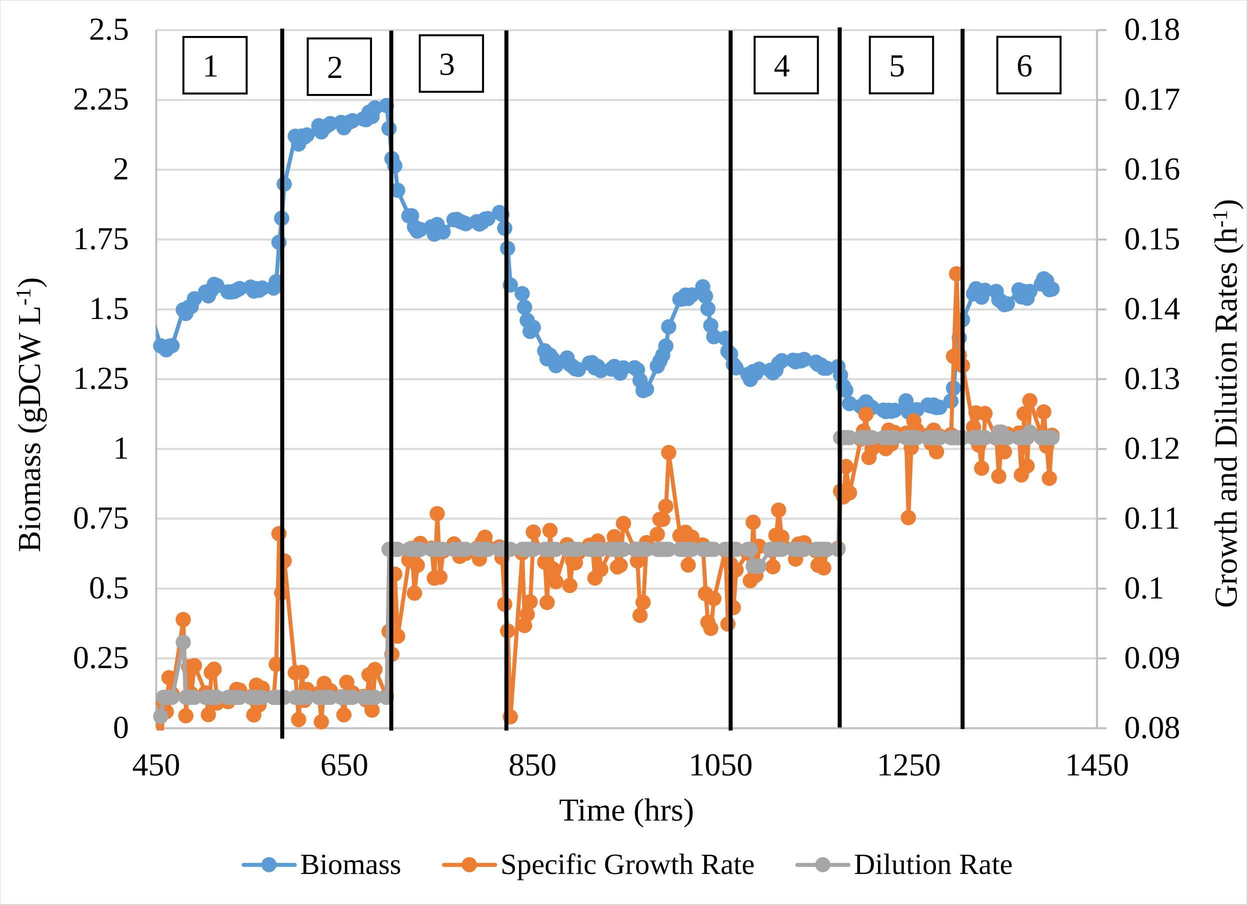

Figure 28: Cell density and specific growth rate over the tested dilution rate for chemostat Case 2

From Figure 28, the significant change in biomass upon transitioning to different oxygen levels is apparent as seen in the comparison between conditions 1 vs 2, 3 vs 4, and 5 vs 6. Thus, providing clear evidence of when the cells are under methane or oxygen depletion as planned with Equation 13. Additionally, the increase in dilution rate between conditions 2 to 3, and again with 4 to 5 exhibit drops in biomass. This agrees with the general behavior observed in Schill et. al., where the drop in biomass is expected as the transfer rate stay constant, but the dilution rate increases [125].

The substrate pickup rates (O_2 and CH_4) are illustrated below as well as the complete CO_2 production rate (accounted from the headspace and the liquid phase) in Figures 29-30 and Tables 11-12. The values selected as steady state are those that show less than 10% deviation for biomass and pickup rates within the tested condition. Compared to the data in Case 1 (see Figure 30), it is apparent that the standard deviation for this run (Case 2) is significantly smaller. This is due to the application of the syringe pump continuously flowing antifoam into the system that eliminates the enhanced pickup rates and biomass production previously observed. A noticeable range of data between hours 850-1050 are not considered steady state because of a steady decline in oxygen. This behavior was unexpected and perplexing because as the oxygen dropped, the biomass and methane production remained relatively constant, as if the cells expressed enzymatic pathways that decrease the dependence on this substrate. Such behavior continued through hours 960-968 till the cells experienced a noticeable drop in biomass as the behavior appeared to be unsustainable. From previous literature, an excessive abundance of nitrate is known to negatively affect cell growth and vitality [32,107]. To test whether nitrate may indeed be the influential factor, the cells were temporarily induced with a higher oxygen state between hours 967-1030 to recover biomass while the medium inside the reactor was replaced with typical NMS2 medium with only 2x the trace element solution and no supplemented nitrate (i.e. remained at 1 g L^{-1}). Then condition 4 was reset and the cells reached steady state with satisfactory deviation between gas rates and biomass. For Conditions 4 and 5 nitrate remained at normal levels for typical NMS2 medium and supplemental nitrate (2x) was not re-used again till Condition 6. The possible role of nitrate on metabolic behavior is discussed further in the next chapter.

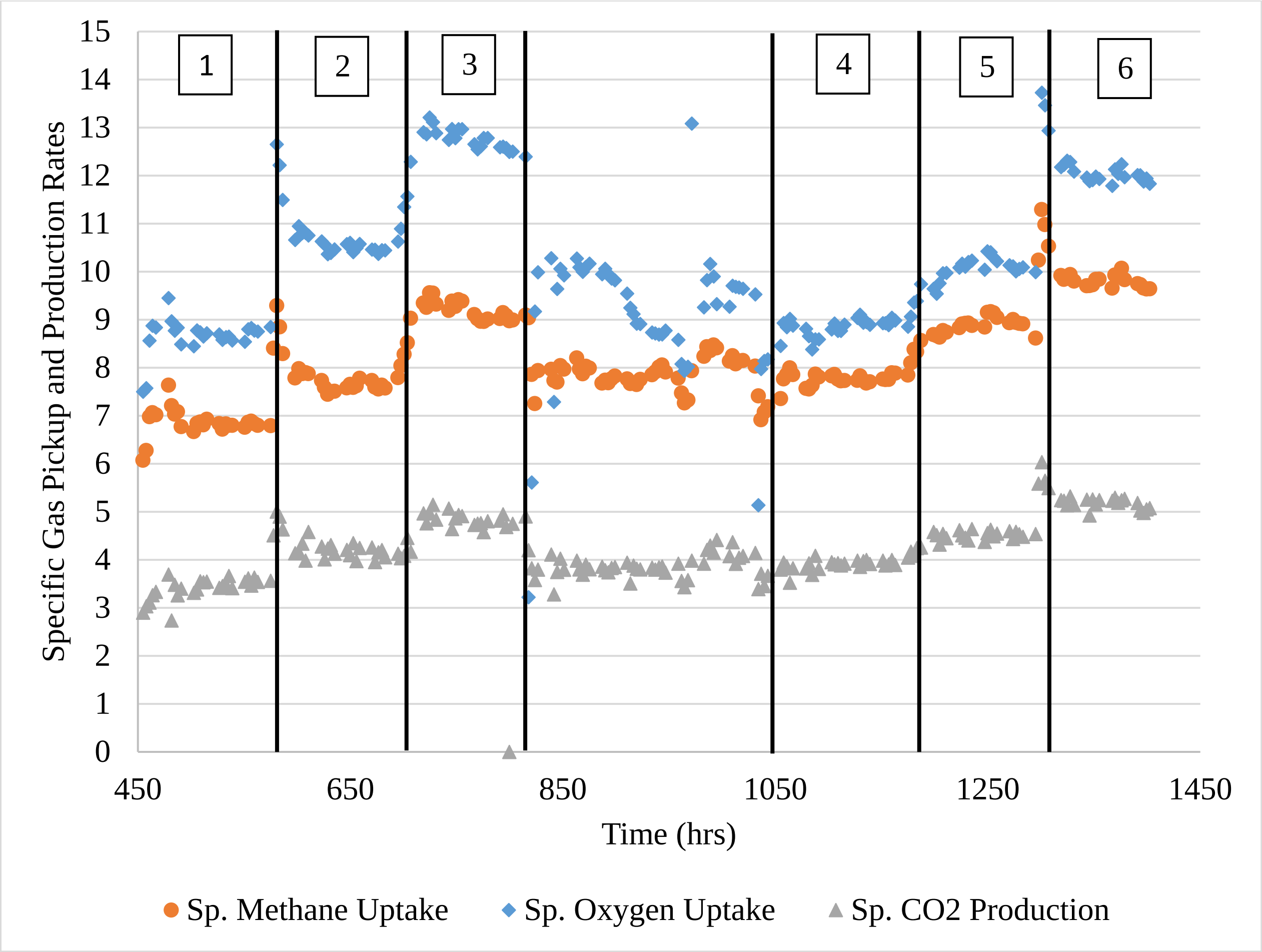

Figure 29: Gas pickup and production rates for chemostat Case 2. All rates are in units of mmol gDCW^{-1} h^{-1}.

Condition	Methane Pickup	Oxygen Pickup	O_2:CH_4 pickup	CO_2 Production	Formate Production
1 A	6.82 ± 0.10	8.66 ± 0.13	1.27 ± 0.01	3.46 ± 0.11	0.006 ± 0.001
1 B	6.80 ± 0.05	8.62 ± 0.05	1.27 ± 0.01	3.48 ± 0.10	0.006 ± 0.001
1 C	6.83 ± 0.05	8.74 ± 0.11	1.28 ± 0.01	3.56 ± 0.07	0.006 ± 0.001
2 A	7.55 ± 0.11	10.48 ± 0.11	1.39 ± 0.01	4.19 ± 0.12	0.001 ± 0.001
2 B	7.64 ± 0.08	10.53 ± 0.08	1.38 ± 0.01	4.17 ± 0.14	0.001 ± 0.001
2 C	7.62 ± 0.07	10.43 ± 0.04	1.37 ± 0.01	4.12 ± 0.12	0.001 ± 0.000

3 A	9.33 ± 0.09	12.89 ± 0.11	1.38 ± 0.00	4.88 ± 0.16	0.007 ± 0.002
3 B	9.01 ± 0.06	12.68 ± 0.11	1.41 ± 0.02	4.72 ± 0.09	0.006 ± 0.001
3 C	9.04 ± 0.07	12.55 ± 0.05	1.39 ± 0.01	4.80 ± 0.11	0.006 ± 0.001
4 A	7.78 ± 0.06	8.83 ± 0.07	1.13 ± 0.01	3.92 ± 0.03	0.002 ± 0.001
4 B	7.74 ± 0.06	8.98 ± 0.08	1.16 ± 0.01	3.94 ± 0.06	0.001 ± 0.001
4 C	7.81 ± 0.07	8.95 ± 0.06	1.15 ± 0.00	3.93 ± 0.05	0.001 ± 0.001
5 A	8.89 ± 0.04	10.16 ± 0.06	1.14 ± 0.01	4.53 ± 0.10	0.004 ± 0.002
5 B	9.07 ± 0.13	10.28 ± 0.16	1.13 ± 0.01	4.52 ± 0.09	0.003 ± 0.002
5 C	8.94 ± 0.04	10.08 ± 0.06	1.13 ± 0.01	4.53 ± 0.07	0.002 ± 0.002
6 A	9.87 ± 0.06	12.22 ± 0.09	1.24 ± 0.01	5.21 ± 0.08	0.006 ± 0.003
6 B	9.76 ± 0.07	11.93 ± 0.04	1.22 ± 0.01	5.17 ± 0.14	0.007± 0.001
6 C	9.88 ± 0.15	12.03 ± 0.17	1.22 ± 0.00	5.24 ± 0.04	0.007 ± 0.001
6 D	9.68 ± 0.05	11.93 ± 0.08	1.23 ± 0.00	5.06 ± 0.08	0.007 ± 0.002

Table 11: Chemostat Case 2 steady state pickup and production values for gasses and formate. All pickup and production rates are in units of mmol gDCW $^{-1}$ h^{-1}.

From the above table and Figure 30c an interesting difference in O_2:CH_4 is observed. For conditions 2 to 3 and 4 to 5 the pickup ratios remain relatively constant with values of about 1.15 and 1.39, respectively. With Condition 1, that experiences oxygen depletion as condition 4 and 5, a considerably larger pickup with average values of 1.27 was measured. Similarly, Condition 6 experiences a pickup of 1.27 that is lower than those observed with similar atmospheres in Condition 2 and 3. This difference is not caused by methane pickup, but rather than oxygen pickup. When comparing Conditions 1 and 4 where the only difference is the higher dilution rate, the methane increases by ~14% while the oxygen by ~2%. On the other hand, the parallel change for Conditions 4 to 5 see a methane and oxygen uptake increase of 14.7% and 13.5%, respectively. Thus, oxygen pickup rate between Condition 1 and 4 does not follow the expected increased behavior (seen with transition of Conditions 4 to 5) as outlined by traditional gas fermentation theory in Chapter 5 Section 1. Similarly, when comparing Conditions 6 to 3, the methane increases by ~7.4%, while the oxygen actually decreased by 5.3%. When comparing the differences with condition 2 to 3 which was done via changing dilution rate only, the methane and oxygen content increased by 37.8 and 39.2% respectively. From this data, it is apparent that the previous state of the cell is heavily influential on the next state, a factor not considered from the discussed theory. The metabolic implications of this noticeable difference are discussed further in the next chapter.

a)

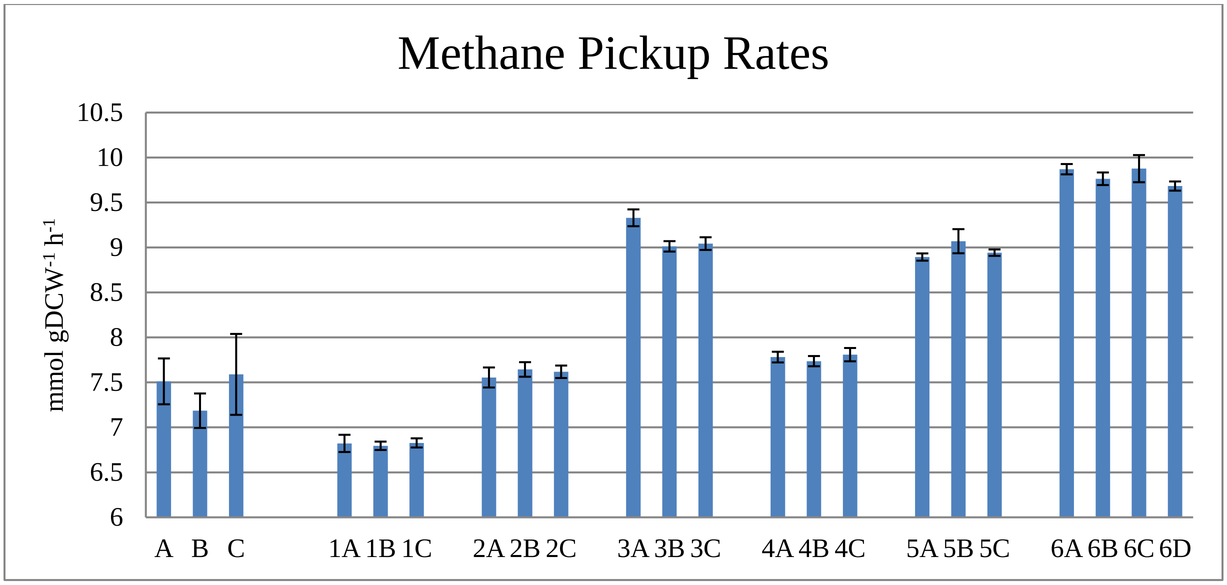

b)

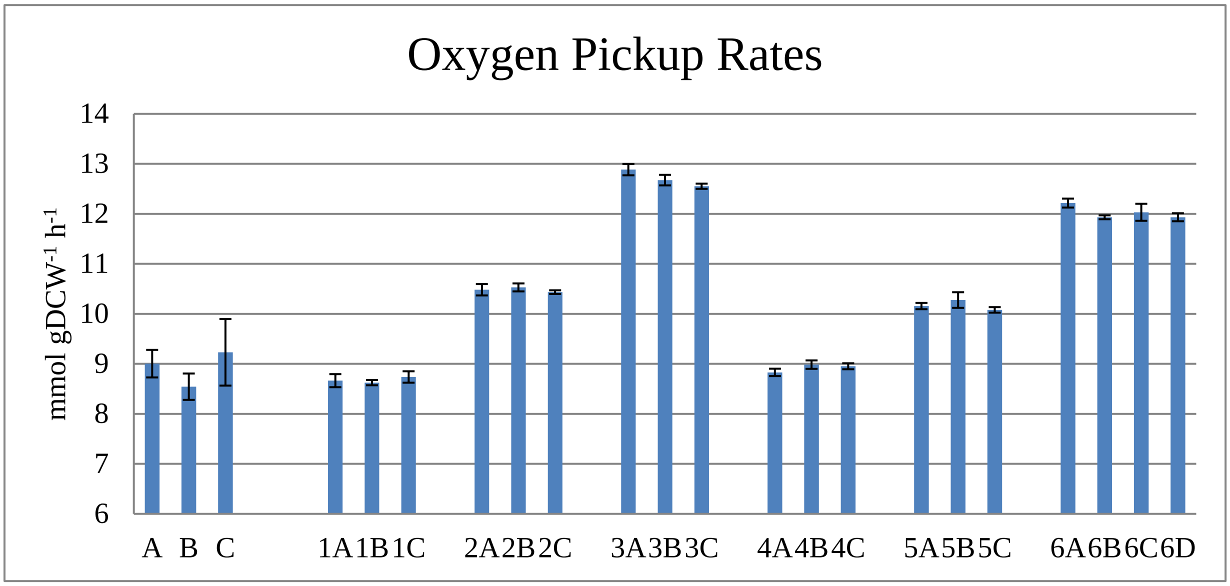
Oxygen Pickup Rates
mmol gDCW-1 h-1
14
13
12
11
10
9
8
7
6
A
B
C
1A
1B
1C
2A
2B
2C
3A
3B
3C
4A
4B
4C
5A
5B
5C
6A
6B
6C
6D

c)

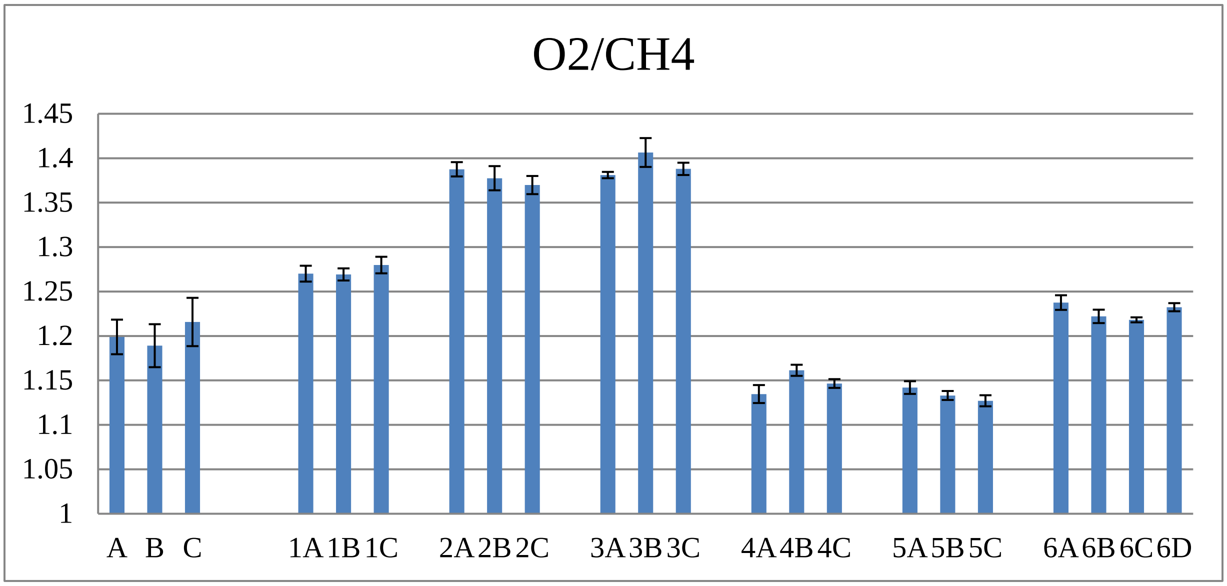
O2/CH4
1.45
1.4
1.35
1.3
1.25
1.2
1.15
1.1
1.05
1
A
B
C
1A
1B
1C
2A
2B
2C
3A
3B
3C
4A
4B
4C
5A
5B
5C
6A
6B
6C
6D

d)

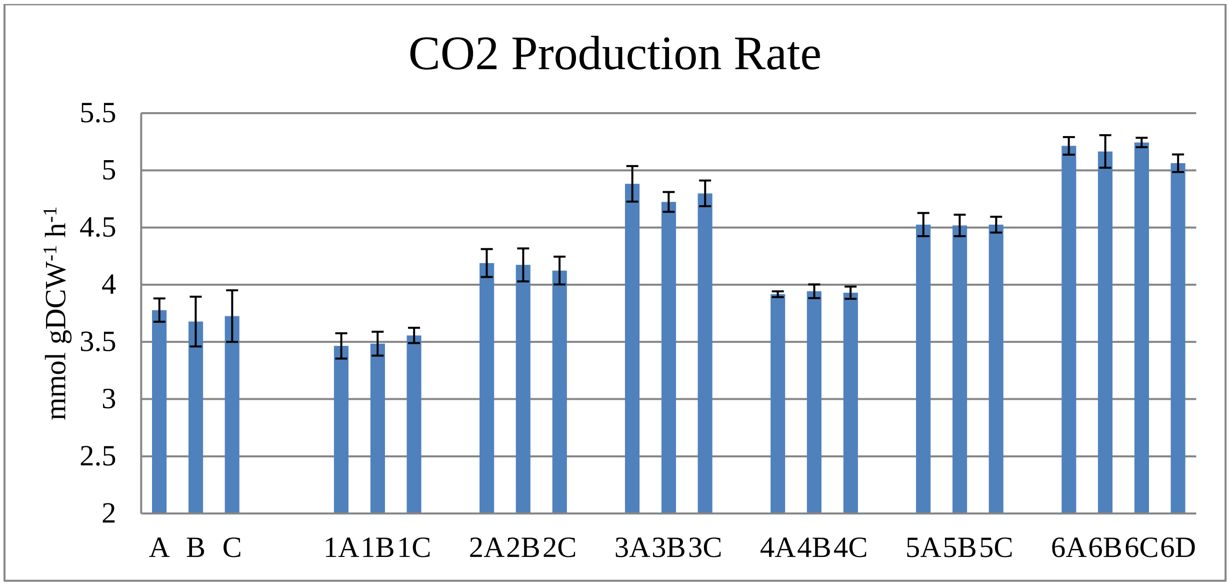

Figure 30: Comparative gas data from chemostat Cases 1 and 2.

Condition	Biomass (gDCW L^{-1})	Growth Rate (h^{-1})	Carbon Balance	Y CO$_2$/S	Y X/S	Y OC/S
1 A	1.57 ± 0.02	0.085 ± 0.003	101.2 ± 2.4	0.502 ± 0.010	0.480 ± 0.007	0.012 ± 0.007
1 B	1.57 ± 0.01	0.085 ± 0.001	101.3 ± 3.3	0.506 ± 0.018	0.478 ± 0.013	0.017 ± 0.015
1 C	1.57 ± 0.01	0.084 ± 0.002	101.3 ± 2.3	0.515 ± 0.011	0.473 ± 0.011	0.008 ± 0.009
2 A	2.15 ± 0.01	0.085 ± 0.002	103.0 ± 3.9	0.539 ± 0.011	0.422 ± 0.011	0.034 ± 0.020
2 B	2.17 ± 0.01	0.085 ± 0.002	102.6 ± 0.9	0.532 ± 0.020	0.418 ± 0.008	0.044 ± 0.026
2 C	2.20 ± 0.02	0.085 ± 0.002	102.0 ± 2.2	0.531 ± 0.015	0.427 ± 0.010	0.037 ± 0.012
3 A	1.78 ± 0.01	0.105 ± 0.004	100.8 ± 2.2	0.520 ± 0.018	0.433 ± 0.012	0.042 ± 0.024

3 B	1.81 ± 0.01	0.105 ± 0.001	102.5 ± 1.7	0.512 ± 0.015	0.443 ± 0.006	0.040 ± 0.020
3 C	1.82 ± 0.01	0.106 ± 0.001	101.8 ± 1.7	0.522 ± 0.018	0.447 ± 0.003	0.027 ± 0.019
4 A	1.29 ± 0.02	0.107 ± 0.003	104.4 ± 2.0	0.482 ± 0.011	0.511 ± 0.015	0.008 ± 0.014
4 B	1.32 ± 0.00	0.106 ± 0.001	104.6 ± 2.1	0.487 ± 0.004	0.507 ± 0.004	0.002 ± 0.003
4 C	1.30 ± 0.01	0.104 ± 0.001	103.3 ± 0.9	0.487 ± 0.009	0.502 ± 0.007	0.007 ± 0.009
5 A	1.14 ± 0.00	0.121 ± 0.001	104.9 ± 2.0	0.485 ± 0.007	0.505 ± 0.007	0.005 ± 0.007
5 B	1.14 ± 0.02	0.120 ± 0.006	101.4 ± 2.7	0.491 ± 0.014	0.505 ± 0.015	0.000 ± 0.001
5 C	1.15 ± 0.00	0.121 ± 0.001	103.3 ± 0.7	0.490 ± 0.008	0.510 ± 0.007	0.002 ± 0.003
6 A	1.56 ± 0.01	0.122 ± 0.003	103.9 ± 2.2	0.509 ± 0.012	0.462 ± 0.009	0.0232 ± 0.010
6 B	1.53 ± 0.02	0.120 ± 0.002	103.3 ± 1.4	0.512 ± 0.008	0.462 ± 0.004	0.020 ± 0.012
6 C	1.56 ± 0.01	0.122 ± 0.005	102.8 ± 3.6	0.517 ± 0.015	0.465 ± 0.007	0.0132 ± 0.011
6 D	1.59 ± 0.02	0.121 ± 0.003	103.3 ± 1.1	0.506 ± 0.006	0.470 ± 0.012	0.0179 ± 0.0107

Table 12: Chemostat Case 2 steady state biomass and carbon values. Yields are mmol C/mmol CH_4 consumed with X as biomass and OC as organic carbon.

From the above table, the carbon balance has clearly been satisfactorily applied throughout the run with average positive errors of 0.8-5%. The deviation for biomass and yields for biomass and CO_2 are fairly narrow, allowing for steady state to be reached. The deviation for the organic content were larger, possibly due to how the organic content is measured. Recall, to find OC, the TC measured is subtracted from the IC measured and thus the OC itself is not directly measured and impacted by the error from both types of analysis.

The yields from methane depended on the conditions and were influenced based off of uptake ratio (O_2:CH_4) as illustrated in Figure 31 and Figure 32. In Figure 31 an increase in uptake ratio leads to a noticeable carbon distribution change. The yields to organic carbon and carbon dioxide increase, while biomass yields decrease. Such alterations may be due to the internal coping mechanism of cells dealing with higher oxygen pickups or oxygen concentration in the gas feed [122,123].

For Y X/S, Conditions 4 and 5 were 50-51%, while Conditions 2 and 3 were 42-45%. Condition 1 varied from the other oxygen depleted states with a drop in biomass yield to 47-48%, as was Condition 6 that was between 46-47%. The difference in CO_2 is subtle between all conditions where Condition 2 and 3 varied between 51-54%, Conditions 1 and 6 were 50-52%, and Conditions 4 and 5 between 48-49%. With that in mind the total carbon conversion efficiency lies between 49-52% throughout the study.

a)

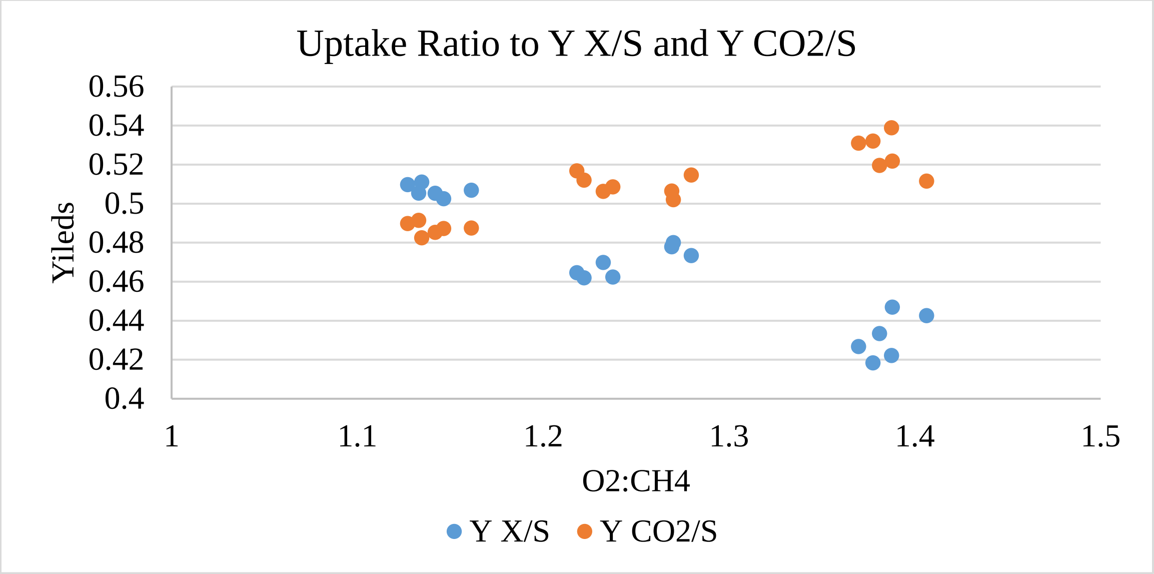

b)

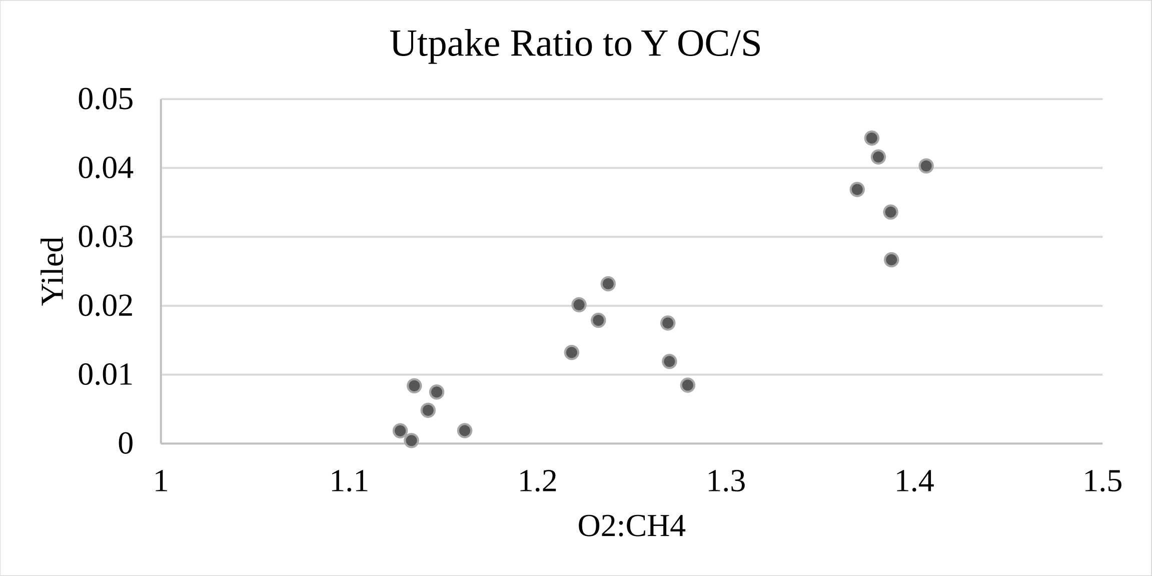

Figure 31: Trends in yields based off of O_2:CH_4 uptake ratios.

a)

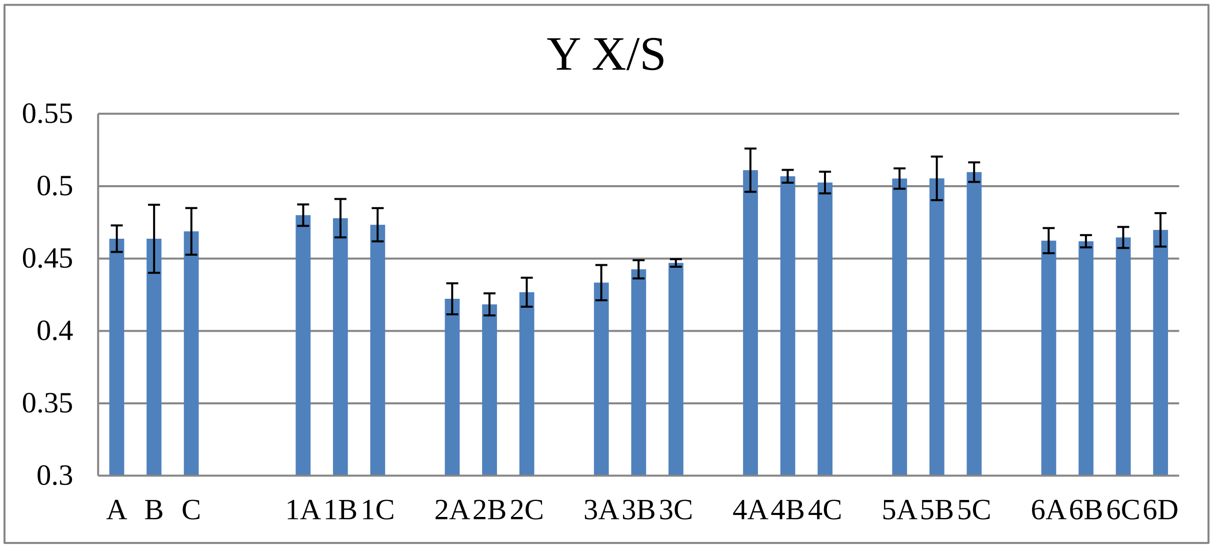

b)

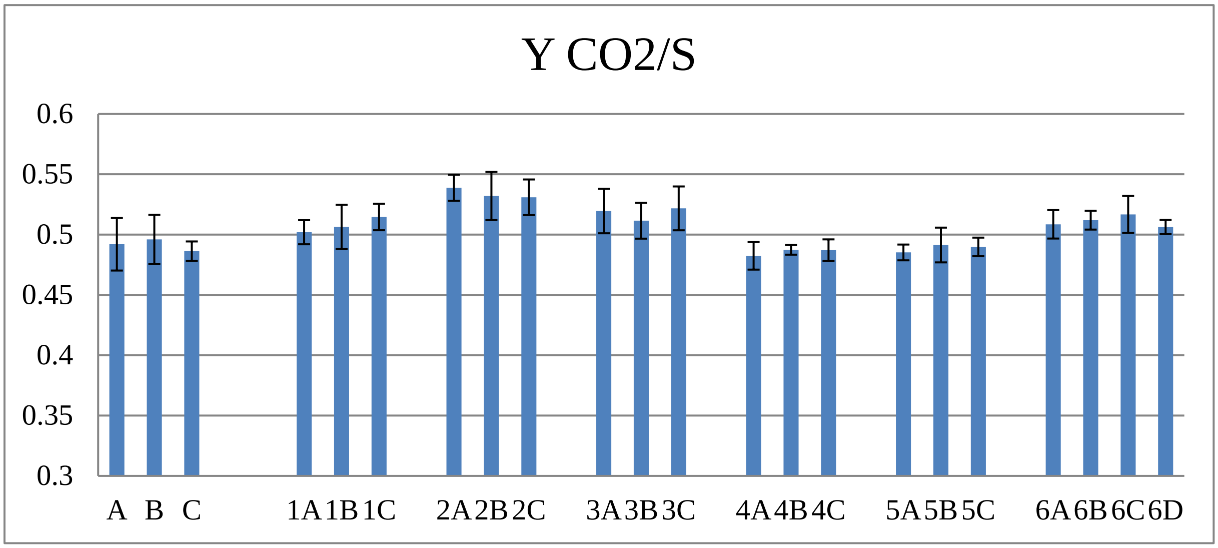

c)

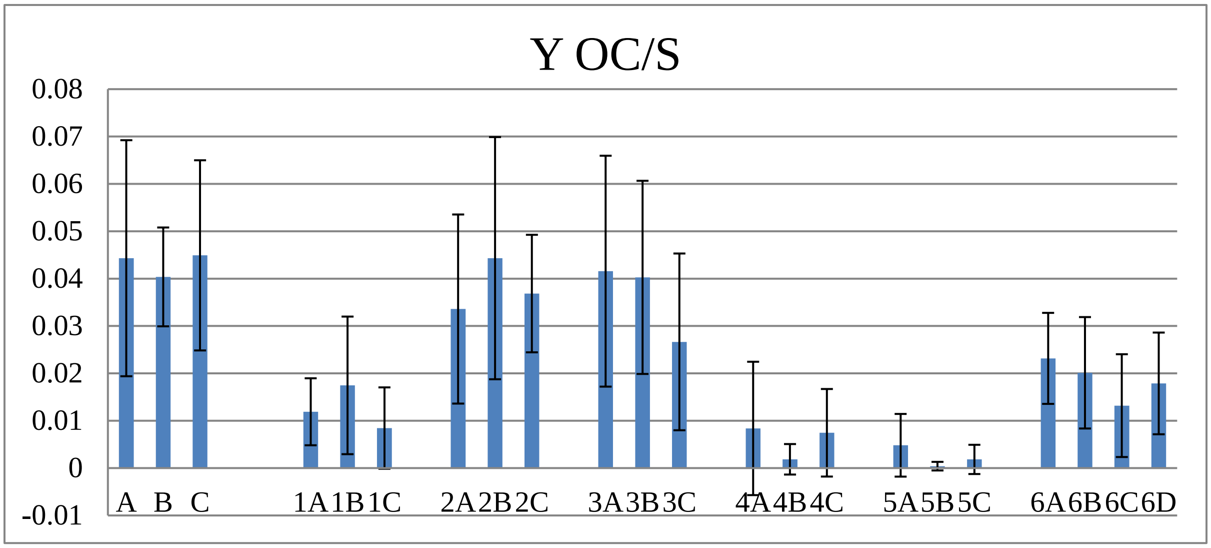

Figure 32: Comparative yield data from chemostat Cases 1 and 2. Case 1 is simply listed as A, B, and C.

Formate production remained low and did not vary in any noticeable pattern. For the steady state values achieved here the specific concentrations were found to vary between 5-32 µmol gDCW^{-1}. Again, the production is lower compared to literature sources and may be due to the larger amounts of nitrate and micronutrients that inhibit a substantial redox imbalance.

5.6 Discussion and Directions for Future Research

Following the data analysis of Case 2, the gas pickup behavior has brought forward many points of interest and room for future questions. Of prominent interest are the low O_2:CH_4 pickup ratios for the oxygen depleted Conditions 4 and 5. When comparing the substrate pickup ratios to literature, these values were found to be consistent with the 1.1-1.2 O_2:CH_4 ratios reported by Gilman et. al, while that of Condition 1 was slightly higher [36]. Methane depleted Conditions 2,3, and 6 experienced pickup ratios between 1.2-1.4. These values were noticeably lower than the 1.6:1 in the same literature source. The lower amounts of oxygen pickup may be due to the methane concentration that was fed into this chemostat versus that of Gilman et. al. Although in Chapter 4, oxygen influence was the dominant influence, both this study and that cited have similar concentrations in the feed stream (23.3 vs 20.5% v/v). However, the methane content fed here was 14% compared to the 2.5% in the reported literature. This larger methane content allows for a larger biomass concentration and in turn, leads to lower dissolved oxygen levels, which prevent a change in phenotypes with lower growth and higher carbon conversion (~60%) efficiencies as seen in vial experiments here and what appears to have occurred in the cited study.

As mentioned before, the specific gas pickup of oxygen (and to a certain extent, methane) did not follow the traditionally expected behavior that Schill et. al. found with their research on methanogens [125]. Thus, one of two rules covered in Section 1 must be at fault: either the biomass concentration or the conversion rate. In the bioreactor run, the dilution rate increased from 0.085 to 0.105 h^{-1} (a 23.5% increase) and then to 0.121 h^{-1} (15.2%). When comparing the biomass between the methane depleted sets with Conditions 2 → 3 → 6, there was a 16.9 and 13.6% drop. Similarly, for the oxygen depleted sets with Conditions 1 → 4 → 5, there was a 17.1 and 12.2 % drop. Both drops are expected as the dilution rate increases and the gas transfer rate stays relatively consistent. Thus, rule 2 of Section 1 holds.

Recall, rule 1 states that the conversion rates would be fairly consistent regardless of the dilution rates examined. When comparing the oxygen conversion rate (mmol h^{-1}) with Conditions 1 → 4 → 5, there was a 14.7% drop and a 0.1% increase, and for the methane conversion rate (mmol hr^{-1}) there was a 5.4% drop and a 1.31% increase. Oddly, for Conditions 2 → 3 → 6 the oxygen conversion rate increased by 0.7% and then dropped 18.2%, while the methane conversion rate dropped by 0.2% and then another drop of 7.3%. All these behaviors are summarized in Table 13 below. From this analysis it is apparent that Condition 1 (compared to 4 and 5) and Condition 6 (compared to 2 and 3) break from the traditional behavior.

Condition	Oxygen Pickup Rate (mmol h^{-1})	Methane Pickup Rate (mmol h^{-1})
1 A	20.40	16.06
1 B	20.26	15.96
1 C	20.60	16.10
2 A	33.85	24.39
2 B	34.21	24.83
2 C	34.36	25.09
3 A	34.49	24.97
3 B	34.50	24.53
3 C	34.18	24.62
4 A	17.10	15.07
4 B	17.73	15.27
4 C	17.43	15.21
5 A	17.31	15.16
5 B	17.59	15.52

5 C	17.42	15.46
6 A	28.61	23.11
6 B	27.42	22.44
6 C	28.08	23.05
6 D	28.43	23.07

Table 13: Pickup rates (mmol h^{-1}) for methane and oxygen from Case 2 of chemostat runs.

As stated above, rule 1 of Section 1 was broken as the conversion rates from Conditions 1 and 6 were not consistent. So, the question becomes what has altered the conversion rate of the gases: the transfer of rate or the uptake? As stated beforehand, the transfer rate can be affected by antifoam addition. However, the antifoam levels were only adjusted after Condition 2, which does not explain the change is observed in Condition 6 but not Condition 3. Additionally, the antifoam appeared to have an equal effect on oxygen and methane as seen in the pickup rates in Case 1 set C (see Figure 26). Separately, the carbon balance suggests that there was no potential leak from the mixing system thus negating that as a potential issue. Finally, the Bioflo shows minimal to no change in the control of agitation and pH, meaning these factors that affect cell behavior were properly controlled. Regardless if any of these possibilities could affect the transfer rate, it is unclear why oxygen would be overly influenced with differences >14% while methane was <8%. Even when considering the k_La ratio of 0.855 (from Equation 13), the effects should be much closer (methane % change ~11). Thus, the transfer of the gasses does not appear to be the problem, leaving only the cellular pickup as the potential cause.

Pickup rates can be influenced by components in the medium or any change in intracellular mechanisms. For this study, no analytical tools were utilized to measure macronutrients, such as nitrate, or micronutrients, such as copper. However, the rate at which nitrate and influential micronutrients (e.g. copper), are known. Thus, these two components were plotted along the CH_4:O_2 pickup ratio to explore their potential effect on the unusual conversation pickup ratio observed. The results of which are illustrated in Figures 33 and 34.

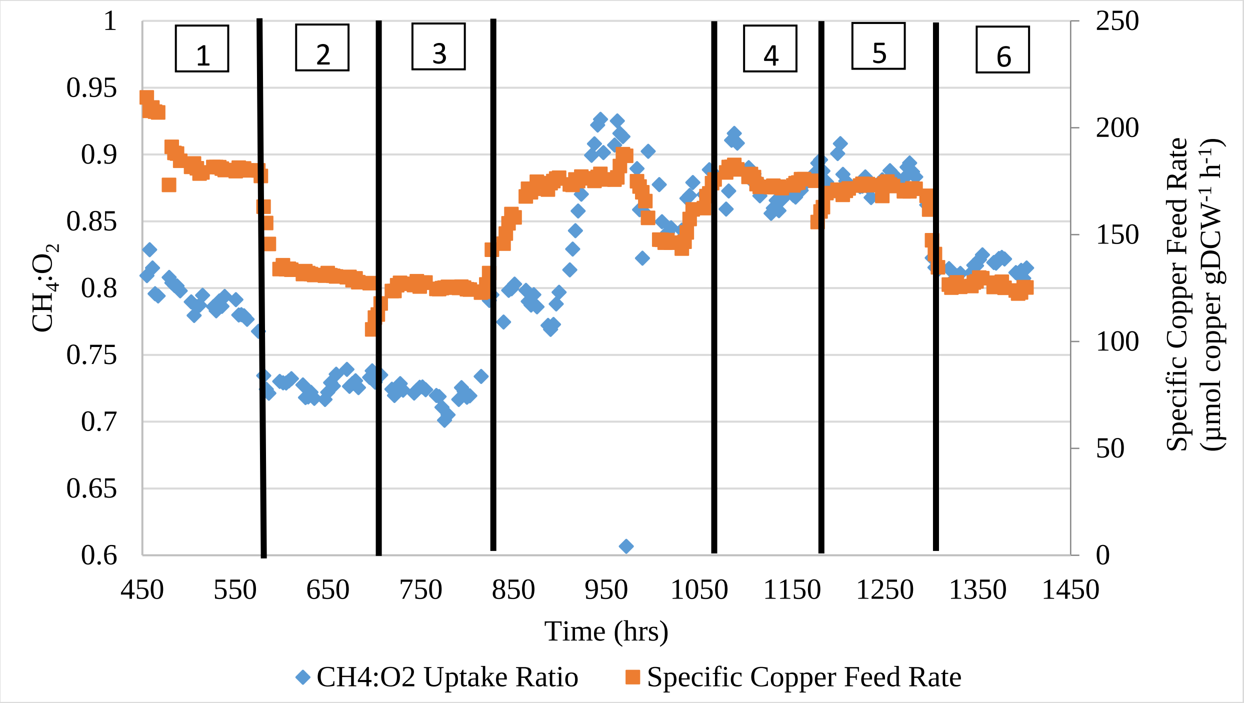

Figure 33: Pickup ratios vs specific copper feed rate.

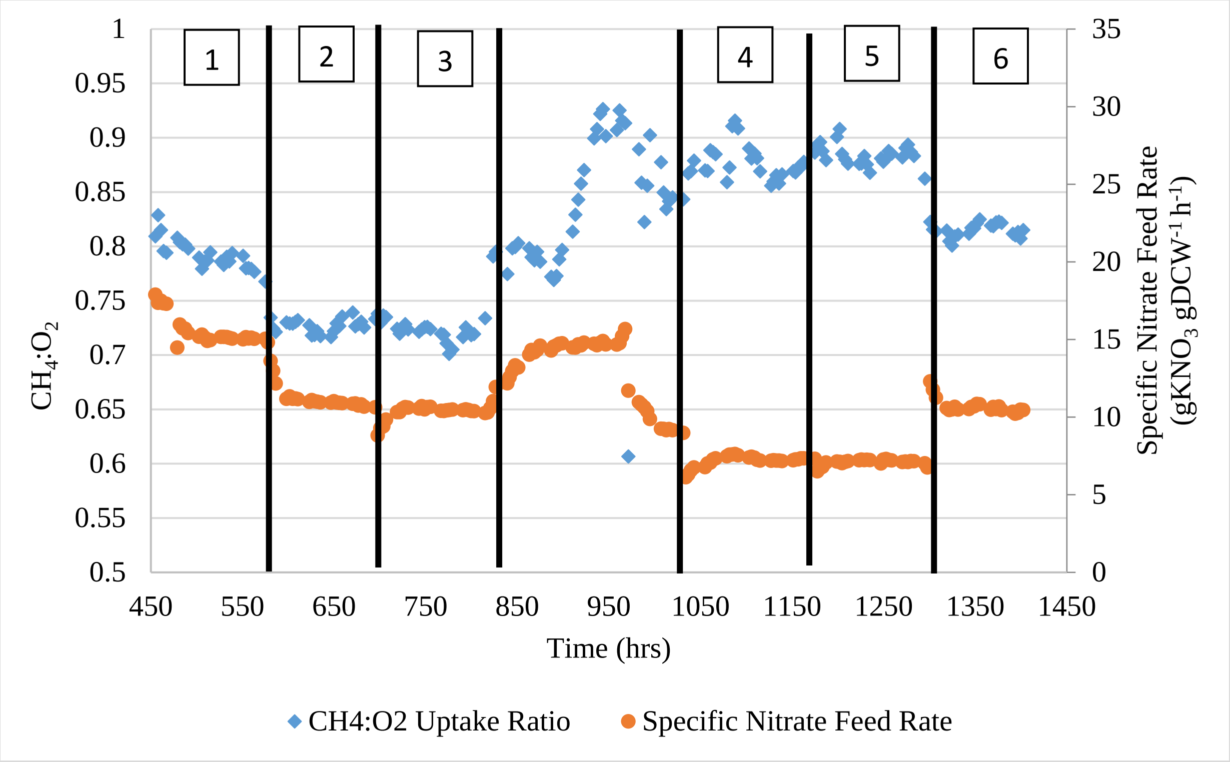

Figure 34: Pickup ratios vs specific nitrate feed rate.

As shown, the initial specific copper feed rate differed on only two levels at approximately 130 and 180 µmol Cu gDCW^{-1} h^{-1}. From the graph, Conditions 2 and 3 share similar ratios and the pickup ratios (CH_4:O_2). The same conclusion can be drawn for Conditions 4 and 5. However, Condition 6 which shares the same copper feed rate as Conditions 2 and 3, does not have the same pickup ratio. Neither does Condition 1 with Conditions 4 and 5, that have similar copper feed rates. Finally, Conditions 1 and 6 with comparable pickup rates have completely different specific copper feed rates. A similar conclusion can be drawn with the specific nitrate feed rates. Conditions 2, 3, and 6 share similar feed rates, but again the pickup ratios are different. Condition 1 has a higher specific nitrate rate than all conditions (recall the medium was adjusted for Condition 4), but again has similar pickup ratios as condition 6.

Though these plots above are not constructed with measured concentrations of either copper or nitrate within the reactor vessel and only based on initial medium concentrations, it does provide doubt that nitrate, as a macronutrient, and/or copper, as micronutrient, have caused a difference in pickup rates. Since the other nutrients can be scaled with these two components in the medium, it appears that logically the other components did not cause the conversion rate differences.

From literature of the biochemistry and metabolic models of methanotrophs, oxygen has two main roles for the organism [66,106,108]. The first as a key electron donor in methane oxidation and second, as the electron acceptor for aerobic respiration. Since the conversion rate drop is not equivalent for methane and oxygen (see Table 13), it is doubtful that methane oxidation alone causes the difference in pickup rates. However, a noticeable dip in methane conversion rates suggests an impact was observed for whatever caused this pickup difference. Thus, leaving the second case of ATP production via aerobic respiration as a possible reason why the cells themselves could have adjusted their pickup rates and broken rule 1 of Section 1. If ATP production is too abundant or limited, it could potentially influence internal mechanism that in turn would affect the pickup rates. These concepts of ATP influence on all conditions are examined further in Chapter 6.

The role of nitrate between the transition of condition 4 and 5 may also be affected by the ATP issues discussed above. As shown in Figure 29, the specific oxygen picks up sharply dropped between the hours of 893-933, while methane uptake remained relatively constant. This led to an O_2:CH_4 relative minimum of 1.08-1.10. After considering the oxygen consumed, very little oxygen is available for aerobic oxidation. Another possibility, but one that is far more unclear, is whether another electron acceptor was adopted by the cells in a hybrid respiratory chain. In recent literature by Kits et. al., two different strains of methanotrophs were found to exhibit denitrification of nitrite (a reduced form of nitrate) [127,128]. With nitrate or nitrite available cells could reduce the cellular oxygen demand for the respiratory chain and thus, utilize oxygen for methane oxidation [129]. In essence, the cell behavior observed here indicates they have adapted their metabolism for efficient use of ATP and how this happens is explored further in Chapter 6.

Finally, to end the discussion of this chapter, it is important to understand why Schill et al. did not observe the deviant behavior that occurred with Case 2 [125]. The organism used in the cited literature was part of the general bacteria class called methanogens. Methanogens fix carbon dioxide in the presence of hydrogen, the latter of which is used by the cell for energy production. Methanogens are highly sensitive to oxygen, as it is toxic to their metabolism, unlike methanotrophs who traditionally produce ATP via aerobic respiration. With completely different pathways towards energy production, the same variability would likely not be observed in their study as it was here.

5.7 Conclusions of Continuous Chemostat Experiments

The results of Case 1 and 2 for this chapter demonstrate that steady state was achieved for a variety of headspace and dilution conditions. With the use of helium as an internal standard, the effluent stream of the bioreactor was able to be properly measured and in turn, provide a carbon balance with typical errors <5%. In addition, the use of continuous source of antifoam allows for less deviation in gas pickup as seen between the results of Case 1 to Case 2 data.

Interestingly, the expected outcome of a constant pickup rate for both methane and oxygen did not occur. Significant drops in oxygen pickup specifically provided evaluation of the transfer rate and pickup rates of the gas. Strictly judging from the physical data, it is does appear that oxygen use in the cells is heavily influenced based off the genetics expressed in their previous state. Such transitions are thought to occur based off energy production within the cells that are further researched in Chapter 6.

Within hypoxia states, aerobic respiration appears to be limited based off the O_2:CH_4 ratio alone. Literature suggests that nitrate plays a role in hybrid aerobic oxidation that could possible explain the ratios observed in Case 2. However, without different analysis and transcriptomic data, this explanation must be further examined.

The carbon conversion efficiencies for all conditions for both cases, regardless of the conditions, range between 47-51%. Those with oxygen abundance tended to divert a slight but noticeable portion of the carbon away from biomass and towards organic carbon production, as is common with cells dealing with larger dissolved oxygen concentrations. The extent of organic carbon production however did not match that observed in high oxygen content vials seen in Chapter 4.

Chapter 6 : Metabolic Modeling of the Cellular Metabolism for *M. buryatense* 5GB1

6.1 Considerations and Assumptions for Metabolic Modeling

As stated beforehand, the reduced model for 5GB1underwent performance analysis of predicted production rates with inputted pickup rates measured in chemostat runs of the previous chapter. Unless stated otherwise, the following assumptions were held throughout this modeling work. The ATP/NADH yield was assumed to remain at 3 (as shown in Equation 2). The growth maintenance value within the set biomass equation was set at low mode with 23 ATP g DCW $^{-1}$. The EMP/EDD ratio was left at the default 0.75/0.25 ratio. Only direct coupling was evaluated within these studies as redox arm and uphill transfer are far less efficient with limited gaseous substrate at desired growth rates [106]. All these assumptions allow for efficient ATP production/consumption and utilizing constrained gaseous substrate pickup for maximal growth, which is the objective function of all studies.

To effectively evaluate model outputs (O_2 pickup rates, CO_2 production, and growth rate) from methane input, the proper non-growth maintenance must be first accounted for. This value can be estimated mathematically via the below mathematical expression. Growth associated maintenance however is often found via fitting experimental results to metabolic models [108].

$$q_{CH_4} = m_{CH_4} + \frac{\mu}{Y_{max}} \tag{16}$$

Figure 35, illustrates that a linear regression could be applied to the six conditions from Case 2. However, before utilizing this regression relationship, it is apparent that the data appears to be split in half. This separation follows those conditions that were methane depleted and those that were oxygen depleted allowing for the non-growth maintenance terms to be calculated for both sets. From the regression analysis and assuming a yield of 6 mol ATP per mole of CH_4 [108], the non-growth maintenance for oxygen and methane depleted conditions were calculated to be 10.60 and 15.53 mmol ATP g DCW^{-1} h^{-1}, respectively. Both values are significantly higher than the assumed value of 8.39 from the original genome scale metabolic model paper [106]. On a separate note, the Y_{max} calculated from both figures remain fairly consistent with values of 1.07 and 1.04 for oxygen and methane depleted conditions, respectively.

a)

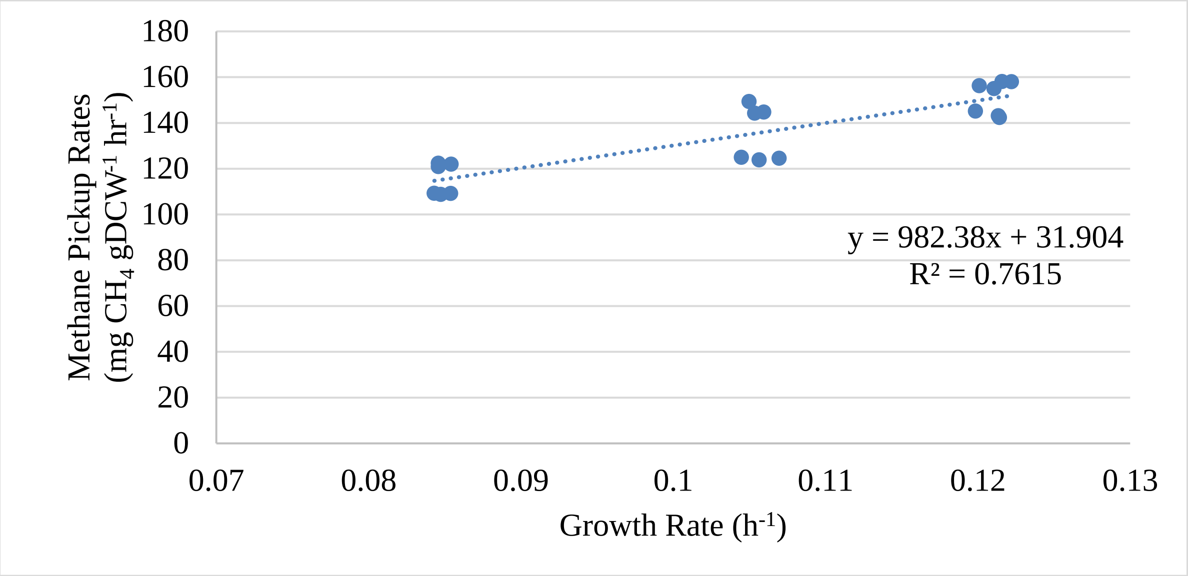

b)

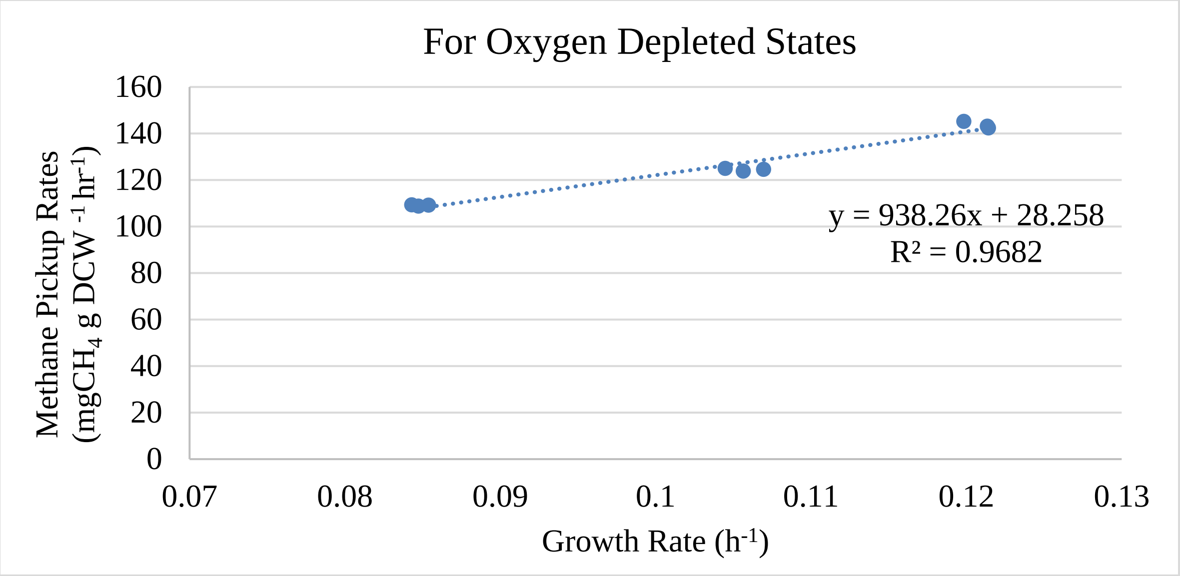

c)

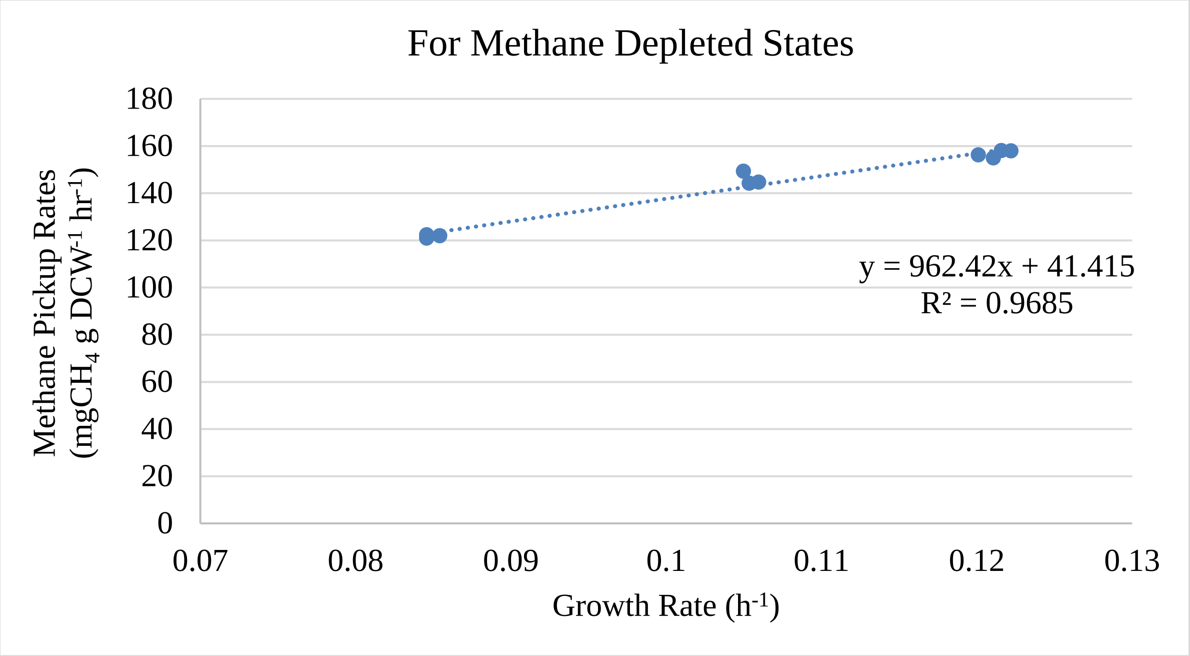

Figure 35: Specific methane pickup vs growth rate to calculate non-growth maintenance ATP flux. a) All fluxes vs growth rate, b) Fluxes of oxygen depleted conditions vs growth rate, c) Fluxes of methane depleted conditions vs growth rate.

6.2 Initial Evaluation with Single Methane Pickup Rate as the Input

The single input of methane into the metabolic model without limitation on oxygen or any extracellular production would automatically generate the optimal solution at that specific point. For Case 1 chemostat data both 8.39 and 10.6 mmol ATP g DCW^{-1} h^{-1} were considered for non-maintenance growth terms. The first value is from initial assumption during model development [106] and latter calculated from the oxygen depleted sets of Case 2. Since Case 1 utilized a single dilution rate, no linear relationship could be developed similar to those seen in Figure 35 to calculate the correct value, thus both are examined. From this single point input, oxygen pickup, carbon dioxide production, and growth rates (represented by the flux in the biomass equation) can be predicted and compared to experimental data measured in Chapter 5 as shown in Tables 14 and 15 for Cases 1 and 2, respectively.

Cond.	Non-Growth Main.	Pred. O2	% O2 Error	Pred. O2/CH4	Biomass	% Growth Error	CO_2	% CO_2 Error
A	8.39	9.06	0.66	1.21	0.101	11.05	3.51	-7.00
	10.6	9.38	4.12	1.25	0.096	5.25	3.72	-1.48
B	8.39	8.72	2.08	1.21	0.096	10.10	3.40	-7.70
	10.6	9.03	5.72	1.26	0.091	4.03	3.60	-2.02
C	8.39	9.14	-0.94	1.21	0.102	12.42	3.54	-4.96
	10.6	9.46	2.43	1.25	0.097	6.62	3.75	0.65

Table 14: Prediction results for growth, oxygen pickup, and CO_2 production rates with methane pickup rate as the only input for Case 1. The pickup and production rates are in units of mmol gDCW^{-1} h^{-1}. The non-growth maintenance term is in units of mmol ATP gDCW^{-1} h^{-1}.

With the lower non-growth maintenance limitation (value of 8.39), the predictions for oxygen were closer to the measured values for each of the three steady state data sets. Recall oxygen is utilized mainly (99% of the time) for methane oxidation and aerobic respiration. Thus, if lower ATP is required for non-growth maintenance, less oxygen would be picked up. On the other hand, growth rate predictions (represented by the flux in the biomass equation) were significantly over predicted (10-12%) with the lower non-growth maintenance while CO_2 production is concurrently under predicted (5-7%). These percentages indicate that an over efficiency in carbon assimilation is taking place relative to the actual measurements. With higher demands of non-growth maintenance, the oxygen pickup prediction worsens slightly (but lie well within experimental standards). Additionally, the lower percent error for growth and carbon dioxide predictions suggest that a higher non-growth maintenance term may be appropriate for model predictions regarding Case 1.

Cond.	Growth Main.	Predicted O_2 Pickup	% Error O2	Pred. O2/CH4	Pred. Growth Rate	% Error Growth Rate	Pred. CO_2 Prod.	% Error CO_2 Prod.
1A	23	8.65	-0.15	1.27	0.085	0.000	3.47	0.20
1B	23	8.62	-0.02	1.27	0.084	-1.18	3.46	-0.63
1C	23	8.66	-0.93	1.27	0.085	1.19	3.47	-2.33
2A	23	10.11	-3.51	1.34	0.085	0.00	4.20	0.33
2B	23	10.21	-3.06	1.34	0.086	1.18	4.24	1.51
2C	23	10.18	-2.44	1.34	0.086	1.18	4.23	0.03
3A	59.81	12.52	-2.86	1.34	0.104	-0.95	5.21	6.70
3B	23	11.64	-8.14	1.29	0.108	2.86	4.73	0.15
3C	23	11.68	-6.98	1.29	0.109	2.83	4.74	-1.17
4A	23	9.66	9.38	1.24	0.100	-6.54	3.82	-2.48
4B	23	9.61	6.96	1.24	0.099	-6.60	3.80	-3.55
4C	23	9.69	8.19	1.24	0.101	-2.89	3.83	-2.55
5A	23	10.83	6.59	1.22	0.118	-2.48	4.22	-6.70
5B	23	11.01	7.12	1.21	0.121	0.83	4.29	-5.11
5C	23	10.88	7.90	1.22	0.119	-1.65	4.24	-6.30
6A	23	12.54	2.69	1.27	0.122	0.00	5.04	-3.30
6B	23	12.43	4.19	1.27	0.120	0.00	5.00	-3.12
6C	23	12.55	4.31	1.27	0.122	0.00	5.04	-3.81
6D	23	12.35	3.47	1.28	0.119	-1.65	4.97	-1.74

Table 15: Prediction results for growth, oxygen pickup, and CO_2 production rates with methane pickup rate as the only input for Case 2. The pickup and production rates are in units of mmol $gDCW^{-1}$ h^{-1}. The non-growth maintenance term is in units of mmol ATP $gDCW^{-1}$ h^{-1}.

The content of Table 15, indicates various behavioral patterns between and even within the oxygen and methane depleted conditions evaluated for Case 2. Predictions for Condition 1 were on point with minimal error in oxygen pickup, carbon dioxide production, and growth prediction rates. Both Conditions 2 and 3 see under predicted oxygen pickup rate values. Recall from Table 12 these conditions were tested with an abundance of oxygen and higher O_2:CH_4 pickup ratios were measured. Despite the additional non-growth associated maintenance for methane depleted conditions (see Figure 35), the efficiency of direct coupling is still efficient enough to require less oxygen. Prediction differences from measured values are minimal for CO_2 production and growth rates. It should be noted, that condition 3A matched well with larger ATP growth maintenance levels compared to the other days for 3B and 3C. Such differences are possibly due to the transition behavior observed in 3A for biomass and pickup rates. This suggests that a smaller window of deviation (<10%) should be considered for proper steady state comparisons.

Conditions 4 and 5 were conducted as oxygen depleted states and thus the pickup rate for the gas is lower. Both sets are predicted by the single methane rate input to have larger than measured oxygen pickup rates (6-9%). This is possibly due to elevated ATP non-growth maintenance from default values (8.39 to 10.6) and the limitations of aerobic respiration yield. Condition 4 growth rate predictions are larger in magnitude compare to those of Condition 5, while the relationship is flipped for carbon dioxide production. This indicates that the methane is used slightly differently between both conditions to handle the energy requirements set by the oxygen pickup values. Finally, model performance for Condition 6 were generally accurate with less than 5% error for all outputs evaluated.

With methane pickup rate being the only set constraint, the following flux map (Figure 36) was created through the central core carbon network for all conditions of Case 2. This network would represent the optimal solutions found in the line of optimality as no other substrate or production was limited. By assuming that no alternative optimal solution is found by the model (something not evaluated in this work but overall studied in Dr. Jin Wang's group [130]), the optimal fluxes throughout the central carbon network would be consistently proportional regardless of the methane pickup rate inputted.

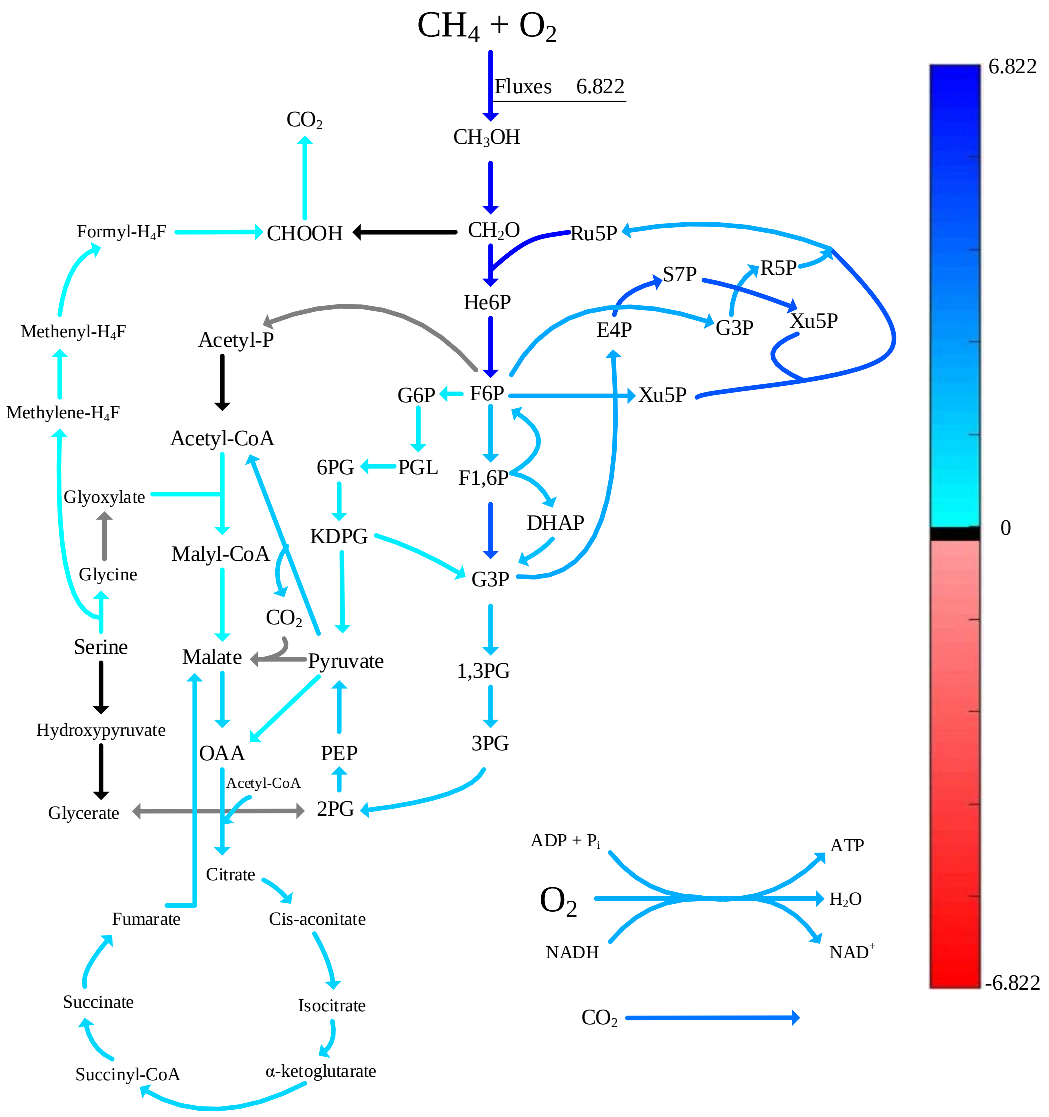

Figure 36: Flux map of *M. buryatense* 5GB1 with specific methane pickup as only input**.** Values represent the fluxes predicted by FBA. The blue indicates positive fluxes and the reaction proceeds in the direction of the arrow. Red fluxes (if any) would indicate flux flows opposite of the arrow direction. Black arrows carry no fluxes and grey arrows are outside of the model stoichiometric matrix.

In addition to the flux map, PhPP analysis (introduced in Chapter 2) was conducted and the measured points are shown on 3D and 2D plots, as illustrated in Figures 37 and 38 for Case 2 of the chemostat runs. The analysis displays only two main phenotypes (light blue and light orange) with the line of optimality for the predicted optimal solutions displayed by the line of black dots. This is a rather small number of planes for this sized model suggesting more work is necessary for developing an accurate GEMs the predicts additional phenotypes. For example, the *E. coli* core model with 95 reactions and 72 metabolites was able to generate 4 phenotypes and many more phenotypes were noted with larger models of *S. stipits* [105,131,132].

a)

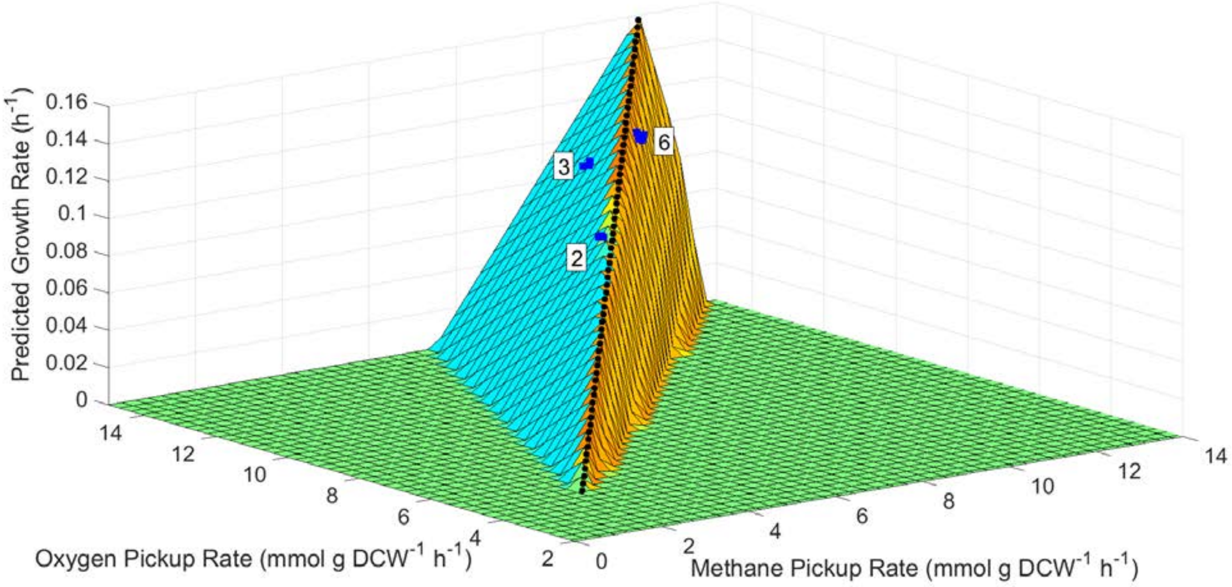

b)

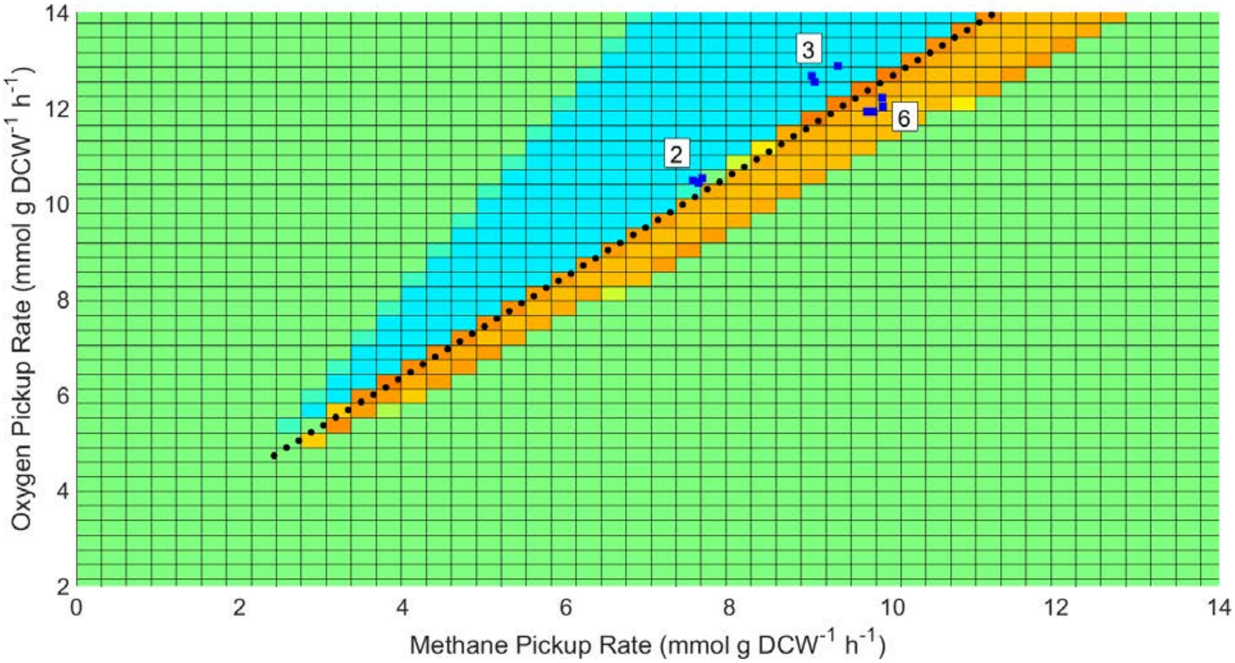

Figure 37: Phenotype phase plane with reduced model for methane depleted conditions 2, 3, and 6. a) 3D plot b) 2D plot. Black points represent the line of optimality. The blue points indicated where actual measured conditions lie on the phenotype phase plane.

a)

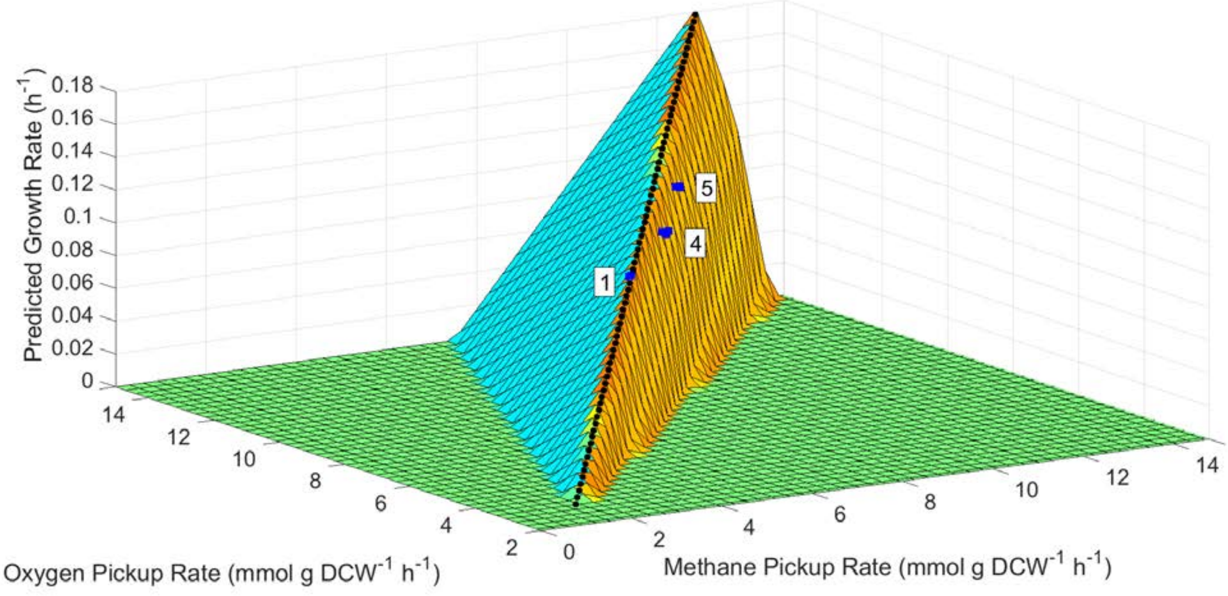

b)

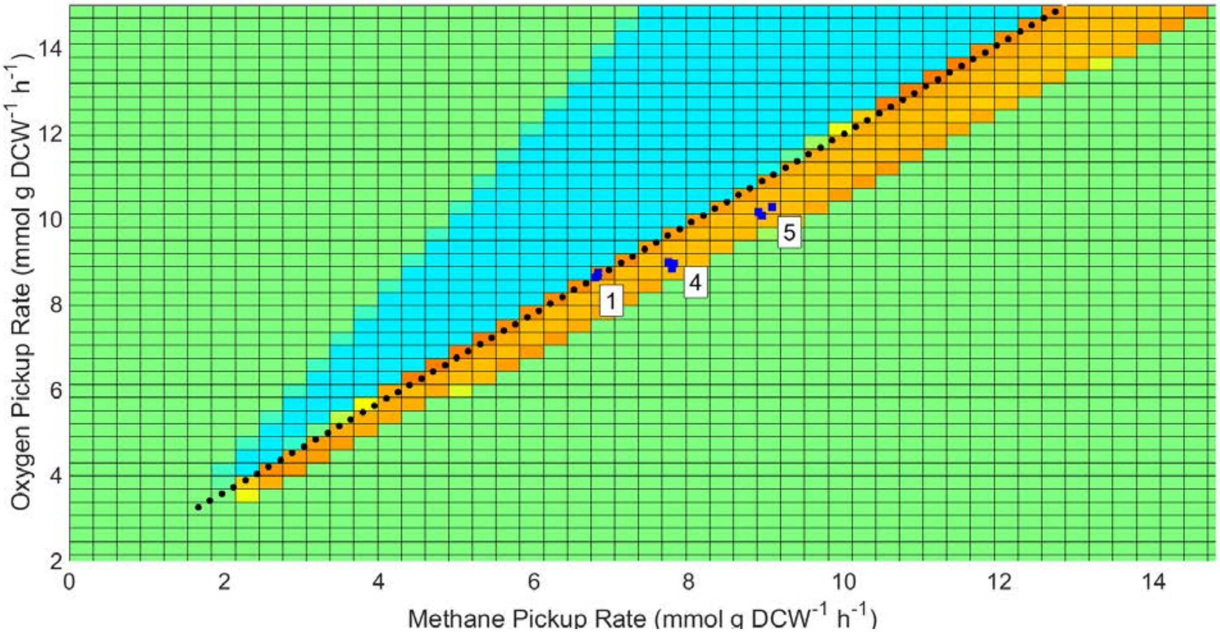

Figure 38: Phenotype phase plane with reduced model for oxygen depleted conditions 1,4, and 5. a) 3D plot b) 2D plot. Black points represent the line of optimality. The blue points indicated where actual measured conditions lie on the phenotype phase plane.

Methane depleted conditions displayed in Figure 37 show that none of the points lie on the line of optimality, though Condition 2 is reasonably close. Conditions 2 and 3 skews into blue phenotype phase plane while Condition 6 drifts into the orange plane. Oxygen depleted conditions in Figure 38 show that condition 1 falls on the line of optimality, agreeing with data analysis from Table 15. Conditions 4 and 5 on the other hand, are positioned far below the line of optimality and slightly above the orange phenotype phase plane. Interestingly to note conditions with the same substrate depletion that were tested subsequently by changing dilution rates (e.g. 2 to 3 and 4 to 5) follow a linear path that may have described a certain behavioral state. Those conditions that altered headspaces (1 and 6) shifted towards a new phase.

6.3 Initial Evaluation with Both Methane and Oxygen Pickup Rates as Inputs

Continuing with the evaluation of the current genome metabolic model, both specific methane and oxygen pickup rates were utilized as input values. With the paired substrate constraints there is no guarantee that the point will lie along the line of optimality (see Figures 37 and 38). The additional oxygen constraint compared to the previous section will reduce the solution space providing unique fluxes through the central carbon network. Carbon dioxide production rate and growth rates remain as the key outputs to be predicted and compared to experimental data. Model performance for both Case 1 and Case are illustrated below.

Cond.	Non-Growth Main	Biomass	% Growth Error	CO_2	% CO_2 Error
A	8.39	0.096	5.01	3.35	-11.40
	10.6	0.061	-32.45	2.69	-28.92
B	8.39	0.079	-8.76	2.90	-21.18
	10.6	0.045	-47.94	2.24	-39.17
C	8.39	0.101	10.80	3.60	-3.40
	10.6	0.076	-16.22	3.12	-16.21

Table 16: Prediction results for growth and CO_2 production rates with specific methane and oxygen pickup rates as inputs to the model for Case 1. The production rates of CO_2 are in units of mmol gDCW^{-1} h^{-1}. The non-growth maintenance term is in units of mmol ATP gDCW^{-1} h^{-1}.

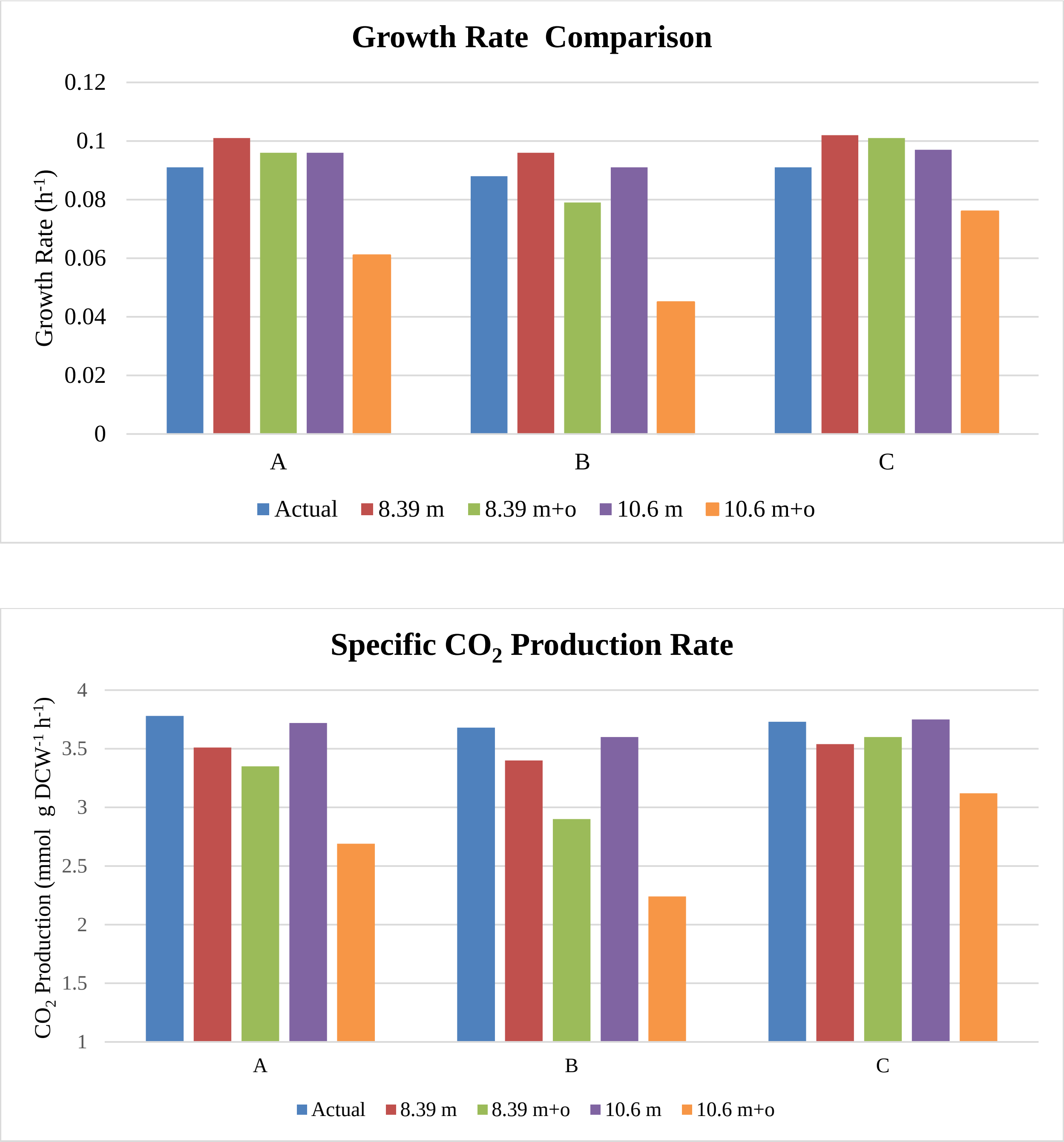

Figure 39: Growth and specific CO_2 production rates predicted for methane (m) or methane and oxygen (m + o) rates as inputs for Case 1. a) Growth rates b) Specific CO_2 production rate.

Due to the stoichiometric matrix, one molecule of oxygen is consumed per methane oxidized by pMMO. Thus, only a portion of the constrained oxygen pickup rate is destined for other intercellular pathways. Once that primary methane oxidation cost is met, >99% of all oxygen is used for the model's ATP generation. By restricting oxygen input into the model, one is essentially restricting the concentration of the electron acceptor in the model's ATP equation and thus the total energy the model can produce for other essential reactions. Data presented in Table 16 and Figure 39 indicate that an insufficient amount of energy is created and thus the predicted growth rates drop significantly when both methane and oxygen rates are constrained, especially with the larger non-growth maintenance. The predicted CO_2 production rate also drops by a significant amount. This curiously implies that the model is desperately attempting to make ATP in a way that clearly undercuts the carbon assimilation efficiency. This concept is further explored in the next section of this chapter.

Condition	Growth maintenance	Predicted Growth Rate	% Error Growth Rate	Predicted CO_2 Production	% Error CO_2 Production
1A	23	0.084	-0.67	3.48	0.47
1B	23	0.084	-1.00	3.46	-0.60
1C	23	0.083	-0.76	3.53	-0.78
2A	23	0.078	-7.69	4.45	6.21
2B	23	0.081	-5.09	4.45	6.69
2C	23	0.081	-4.24	4.40	6.63
3A	23	0.098	-6.75	5.46	11.76
3B	23	0.091	-13.63	5.42	14.81
3C	23	0.094	-11.48	5.33	11.08
4A	23	0.008	-92.18	2.19	-44.07
4B	23	0.039	-63.19	2.17	-44.99
4C	23	0.024	-77.33	2.19	-44.23

5A	23	0.054	-55.10	2.43	-46.28
5B	23	0.048	-60.15	2.48	-45.23
5C	23	0.036	-70.66	2.45	-45.87
6A	23	0.092	-24.88	4.12	-19.51
6B	23	0.074	-38.30	3.61	-30.19
6C	23	0.074	-39.23	3.59	-31.46
6D	23	0.081	-33.31	3.82	-24.60

Table 17: Prediction results for growth and CO_2 production rates with specific methane and oxygen pickup rates as inputs to the model for Case 2. The production rates of CO_2 are in units of mmol gDCW^{-1} h^{-1}. The non-growth maintenance term is in units of mmol ATP gDCW^{-1} h^{-1}.

As with Case 1, methane and oxygen pickup rates were constrained for Case 2 and the results are summarized in Figure 40 below. Condition 1, again, illustrated minimal errors with both methane and oxygen pickup rates as constraints. Conditions 2 and 3 exhibit comparable behavior relative to each other with over predictions occurring for growth rates and under predictions for carbon dioxide production. This suggests that the model is forced to send carbon to rid of the excess oxygen, a concept covered in later sections. Conditions 4 through 6 exhibit analogous negative errors for both predicted growth rates and carbon dioxide. For Conditions 4 and 5 where dissolved oxygen was nearly 0, this matches the behavior observed in Case 1 (Table 16), where oxygen limitation clearly disrupted ATP production. Curiously condition 6 follows the same behavior by possessing a lower O_2:CH_4 pickup rate than the other methane depleted sets (Condition 2 and 3). This is odd because during the experiment the DO was consistently over 8% where oxygen was clearly in abundance supply. A possible explanation would be that the mechanisms utilized in Conditions 4 and 5 were continued for Condition 6, suggesting that a relatively low DO may not offset the intracellular mechanisms utilized.

a)

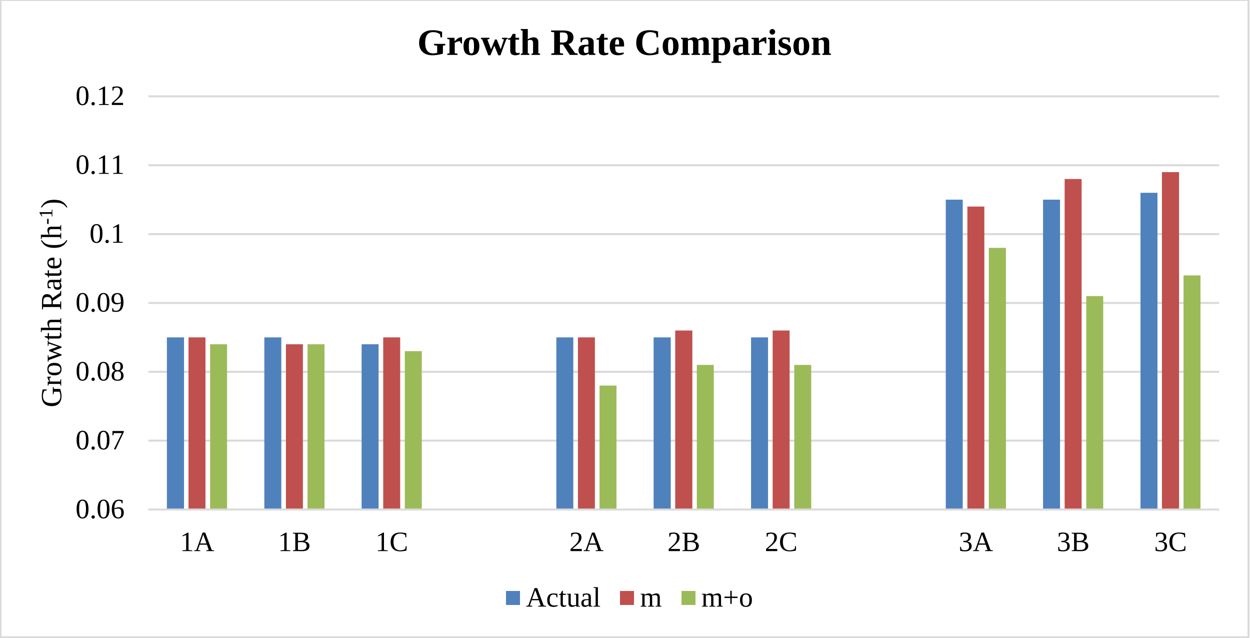

b)

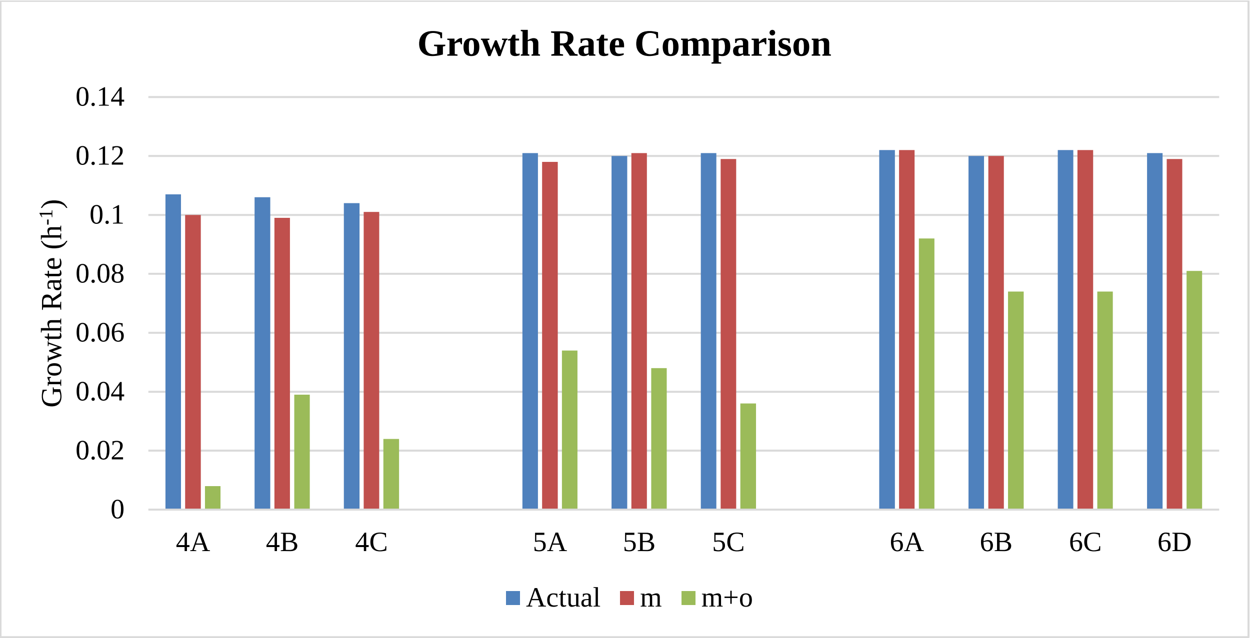

c)

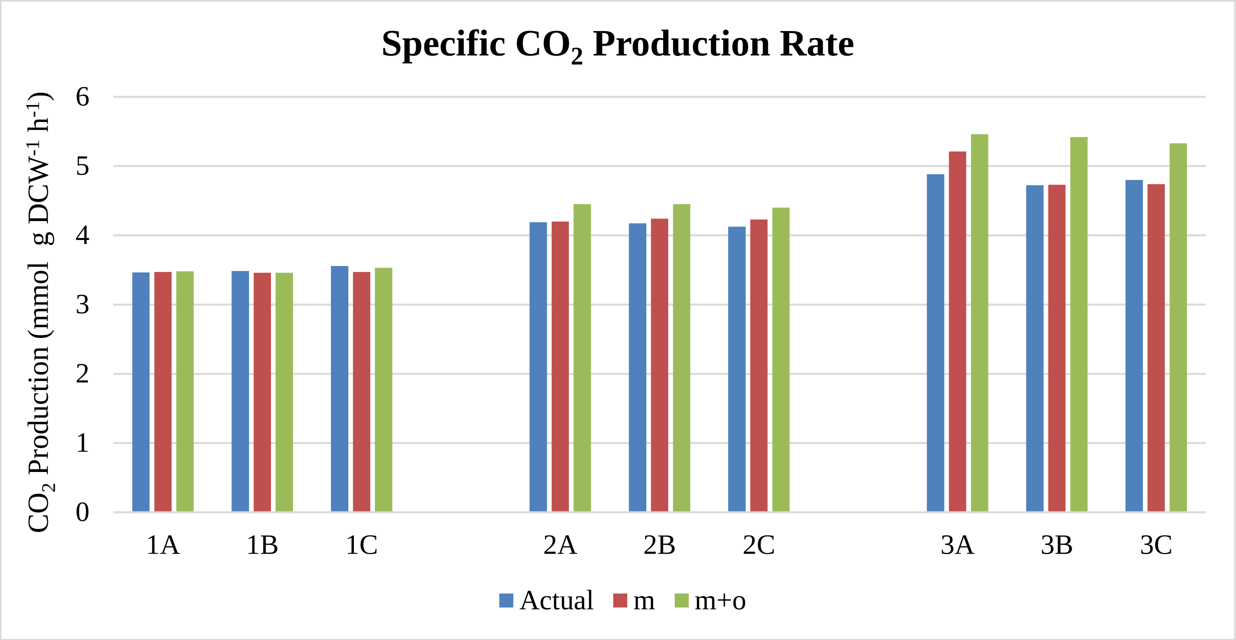

d)

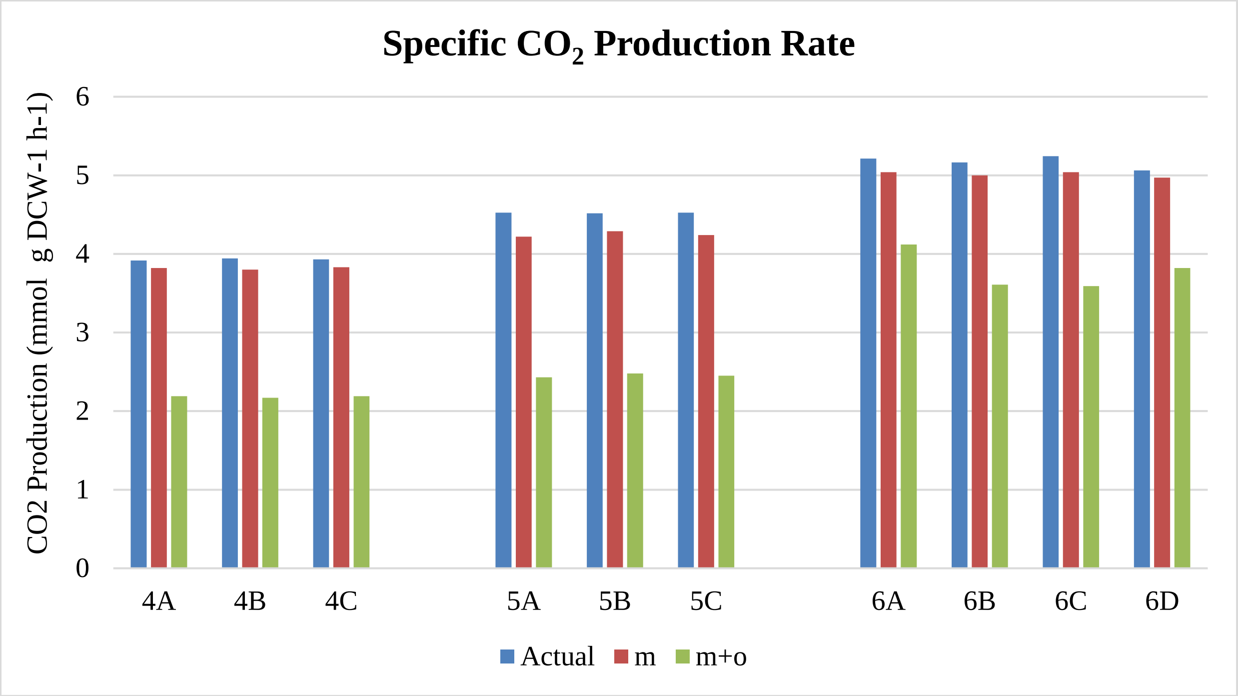

Figure 40: Growth and specific CO_2 production rates predicted for methane (m) or methane and oxygen (m + o) rates as inputs for Case 2. a) Growth rates for conditions 1-3 b) Growth rates for

Conditions 4-6 c) Specific CO_2 production rate for conditions 1-3. d) Specific CO_2 production rate for Conditions 4-6.

6.4 ATP Generation with Depleted Oxygen Conditions

Data in Table 17 for Conditions 4 and 5 indicates significantly lower fluxes for the two expected outlets, carbon dioxide and growth rates, indicating carbon is clearly distributed elsewhere. As stated previously, the limited oxygen is thought to affect the production of ATP which in turn affects the energetic feasibility that goes alongside carbon distribution. The reduced model utilized has 73 reactions that ATP is consume or produced. However, a few key reactions makeup a large portion of the fluxes and thus are listed in the Table 18 below for Condition 4a. Note that negative flux values refer to consumption of ATP, while positive values refer to production of ATP. From the table, the ATP production rate is dropped by half when both gaseous substrate act as inputs. Such a drop cannot possibly overcome the constrained costs of non-growth maintenance alone (10.6) and thus other production routes such as acetate kinase were sought after.

Rxn Name	Rxn Notes	Flux Value m+o input	Flux Value m input
'PHOSGLYPHOS__45__RXN'	EMP (1,3BPG → G3P)	1.938	1.794
'RXNN0B__45__31'	EMP (PEP → Pyruvate)	1.929	1.613
'_3__46__6__46__3__46__27__45__RXN'	ATP non-growth main	-10.6	-10.6
'RXNN0B__45__102'	ATP production	6.287	14.095
'SUCCCOASYN__45__RXN'	TCA Succ.-CoA → Succ.	-0.001	1.166
'ACETATEKIN__45__RXN'	Acetate Kinase Acetyl-P → Acetate	1.816	0

'RXNN0B__45__50'	Production of PPi	-0.644	-0.565
'TRANS__45__RXNN0B__45__8'	Active transport of NO_3^-	-0.386	-0.648
Biomass	Predicted Growth Rate	-0.271	-5.504

Table 18: ATP production and consumption routes for Condition 4a, Case 2 when methane (m) or methane and oxygen (m+o) pickup rates are inputs to the model. All terms are in units of mmol ATP g DCW^{-1}. Negative and positive values represent consumption and production of ATP, respectively.

Furthermore, FBA analysis was conducted to find where most carbon leaves the system via fluxes through the exchange reactions of the transferrable metabolites. Of those within the stoichiometric matrix, carbon is largely secreted from acetate and valine (see Table 19). Together these compounds account for about half of the carbon introduced to the model and over 75% with the addition of carbon dioxide.

Condition	Growth Maintenance	Pred. Acetate Production	Pred. Valine Production	Combined Carbon %	Carbon % with CO_2 + OC*
4A	23	1.81	0.32	67.58	95.74
4B	23	1.87	0.05	51.95	79.99
4C	23	1.85	0.02	48.83	76.90
5A	23	2.05	0.040	48.40	75.77
5B	23	2.06	0.11	51.80	79.08
5C	23	2.45	0.21	66.46	93.86

Table 19: Prediction results for acetate and valine production with specific methane and oxygen pickup rates as inputs to the model for Case 2. The production rates of acetate and valine are in

units of mmol g DCW^{-1} h^{-1}. The growth maintenance term is in units of mmol ATP g DCW^{-1}. OC* refers solely to the carbon amount from excreted acetate and valine.

Reactions for both acetate and valine production routes are demonstrated below. From these equations it is evident that acetate kinase serves as a route to produce ATP by sacrificing carbon for cellular energy. Valine production is indirectly related to the consumption of reducing power (NADPH) through the creation of the glutamate and ketoisovalerate. Together these reactions form a way to consume reducing power while also producing ATP, a behavior akin to the normal aerobic reaction within the model (see Equation 2). In essence, these reactions are the inefficient version of the aerobic respiration the model requires.

Acetate kinase

$$-1\,ADP + -1\,Acetylphosphate \rightarrow\ 1\,ATP\ + 1\,Acetate \tag{17}$$

Branched-chain amino acid aminotransferase for valine

$$\begin{aligned}-1\,Glutamate\ +\ -1\ 2\text{-}Ketoisovalerate \\ \rightarrow 1\,Alphaketoglutarate\ + 1\,Valine\end{aligned} \tag{18}$$

Glutamate dehydrogenase

$$\begin{aligned}-2\,Proton +\ -1\,NADPH +\ -1\,Ammonia +\ -1\ 2\text{-}Ketoglutarate \\ \rightarrow 1\,Water + 1\,NADP + 1\,Glutamate\end{aligned} \tag{19}$$

2-Ketoisovalerate production

$$\begin{aligned}-1\,Proton +\ -1\,NADPH +\ -1\,Alphaacetolactic\ acid \rightarrow \\ \rightarrow 1\,Water + 1\,NADP + 12\text{-}Ketoisovlaerate\end{aligned} \tag{20}$$

A typical flux network for Condition 4 (and inherently 5) is illustrated in Figure 41 where the central carbon network is noticeably affected by the lower oxygen constraint. Firstly, the flux from acetyl-phosphate to acetyl-CoA becomes a negative flux (as indicated by the red color of the arrow). This means that the flux does not follow the direction of the arrow as it would for optimal solutions but would go in the reverse direction where acetyl-CoA is converted to acetyl-phosphate, which is later converted to acetate. Secondly, the succinate to succinyl-CoA flux operates in the negative reaction, which consumes a small amount of ATP. Finally, the α-ketoglutarate dehydrogenase is completely shut off, which essentially prevents the typical completion of the TCA cycle. By the displacement of carbon to acetate and the shut off the TCA cycle, it become very apparent why the model predicted such low growth rates with methane and oxygen pickup rates as model inputs.

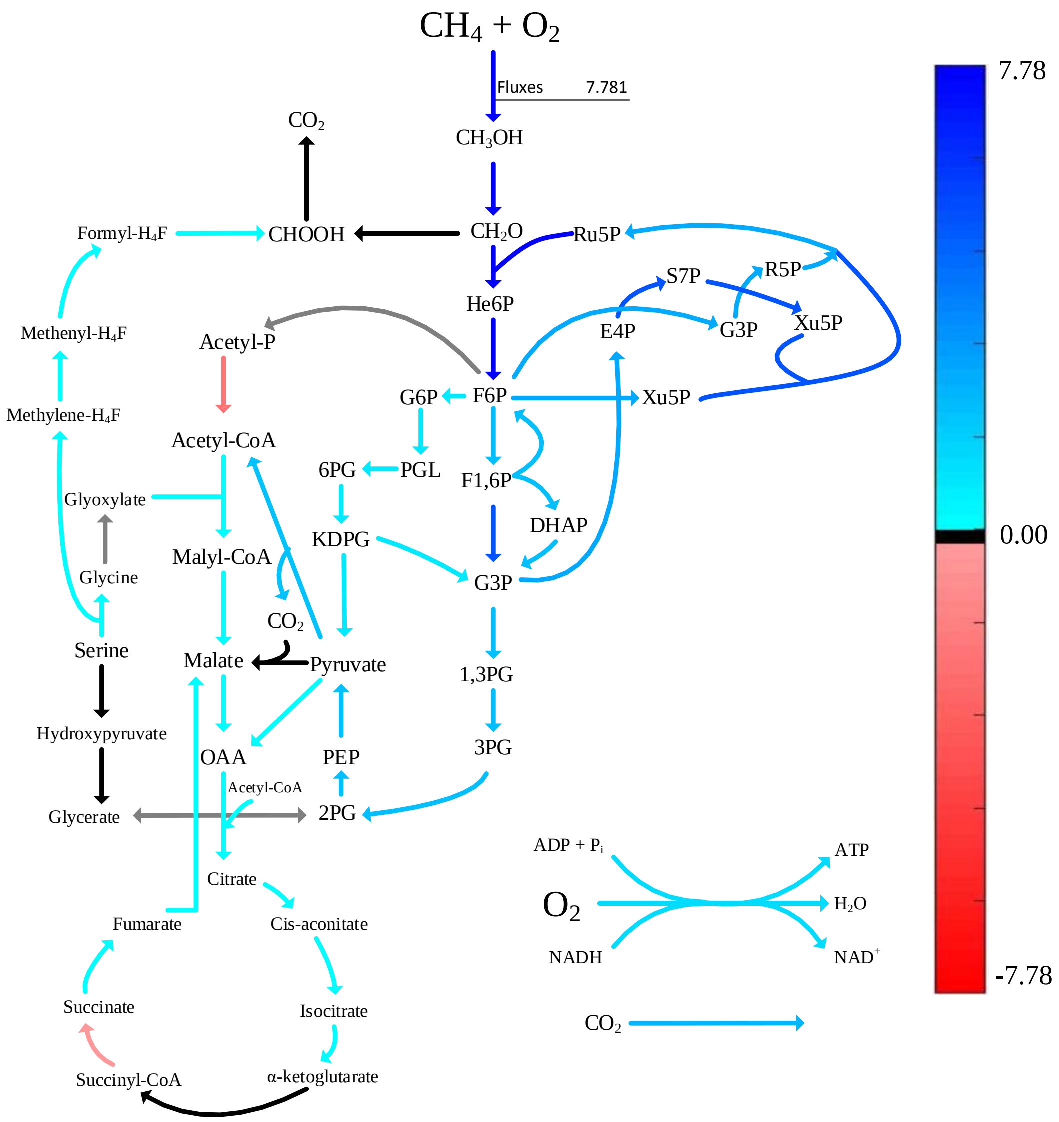

Figure 41: Flux map of *M. buryatense* 5GB1 with specific methane and oxygen pickup rates as inputs for Condition 4a. The blue indicates positive fluxes and the reaction proceeds in the direction of the arrow. Red fluxes (if any) would indicate flux flows opposite of the arrow direction. Black arrows carry no fluxes and grey arrows are outside of the model stoichiometric matrix. The direction of the arrows matches the forward reaction for optimal solutions. Values represent the fluxes predicted by FBA.

6.5 Evaluation of Aerobic ATP Fluxes with Depleted Oxygen Conditions

There are multiple mechanisms in which ATP consumption may be altered to further evaluate Conditions 4-6 with methane and oxygen pickup rates as inputs. As indicated by Table 18, such routes include the EMP/EDD variance, the restricted flux for non-growth maintenance, and the coefficients of ATP required for growth maintenance.

In 2013, Kalyuzhnaya et. al.[66] Summarized the pathways for pyruvate generation via the EDD and EMP routes. Pyruvate is a key component for creation of multiple metabolites for cell growth. From their analysis, the EDD pathway would consume ATP for pyruvate generation, while the ADP-EMP variant would actually create ATP during generation. Both pathways are in the model and pyruvate is produced at a 0.75/0.25 ratio from the EMP/EDD routes. To assess whether significant improvement would be possible with large fractions of pyruvate coming from the EMP (generating ATP), the ratio was steadily increased till EDD was completely off. The results of this alteration for growth and carbon dioxide outputs are illustrated in Figure 42.

a)

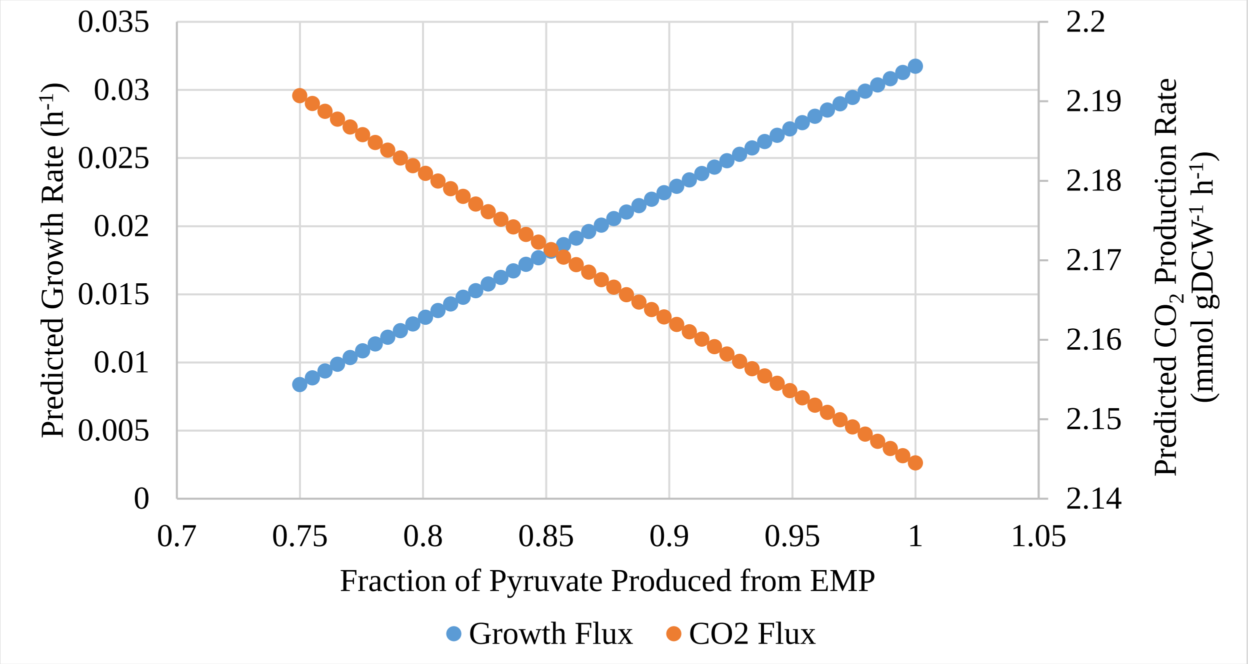

b)

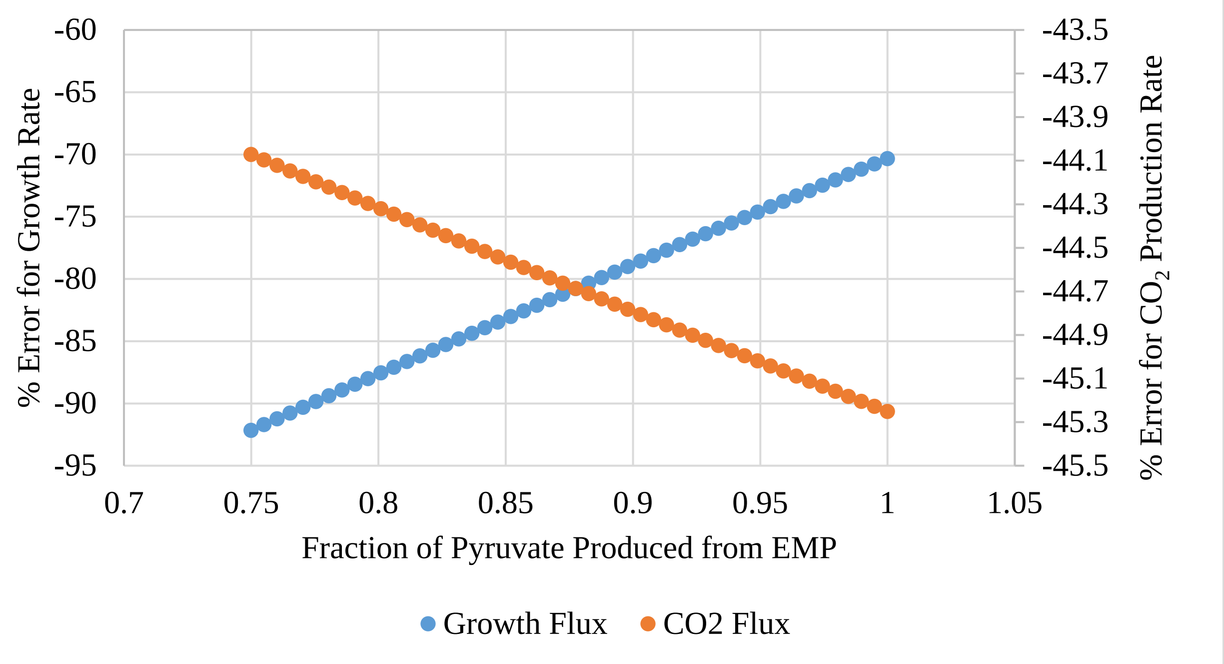

Figure 42: a) Predicted growth and specific CO_2 production rates for increasing pyruvate production from EMP for Condition 4a from Case 2. b) The associated % error from the predicted fluxes compared to measurements from Condition 4a in Case 2.

Despite the increase in energy production with inflated EMP fluxes, the predicted growth and specific CO_2 production rate remains far from the measured value for Condition 4a. Growth rate error improves linearly till errors are close to ~-70% while the CO_2 production rate worsens slightly to values of ~45.3% error. Thus, the EMP/EDD variant alone cannot cover the restrictions imposed on the aerobic respiration.

Growth ATP maintenance is set by the coefficient of ATP in the biomass equation. This value is often selected based off prediction errors on a specific output (often growth rate) [108].

For Conditions 4-6 of Case 2, where ATP is in need for growth, the values of the growth maintenance term was steadily decreased till the coefficient value was 1. By altering the coefficients, the fluxes for growth and specific CO_2 production rates are displayed in Figure 43.

a)

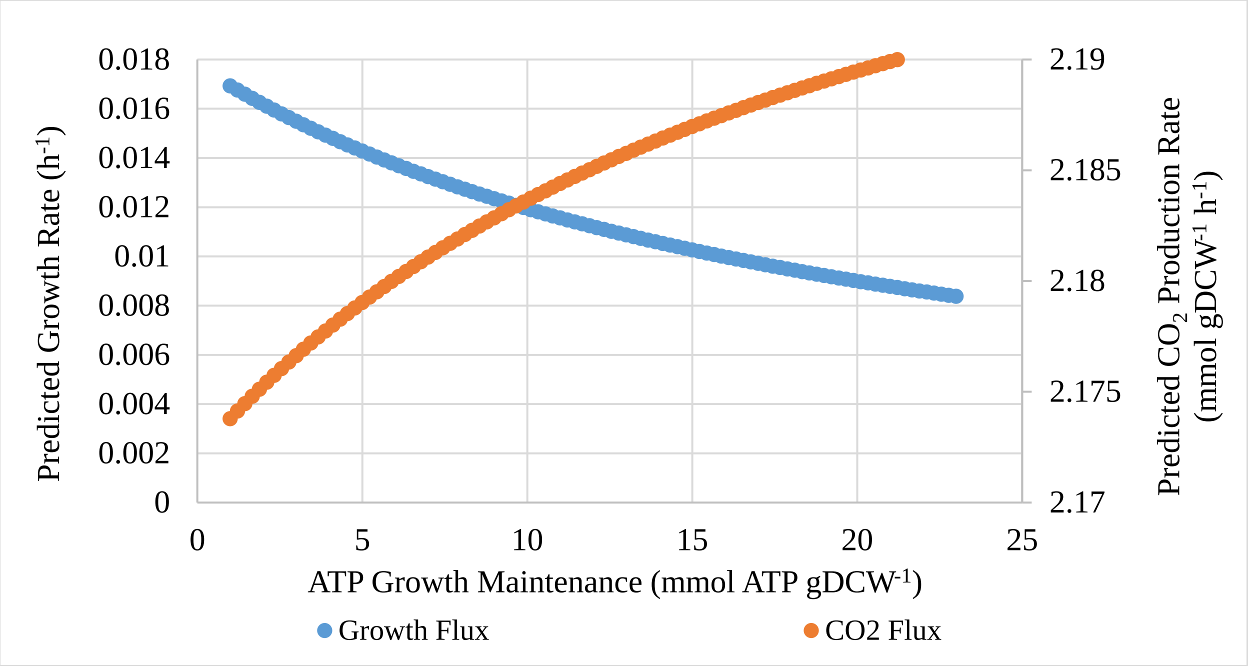

b)

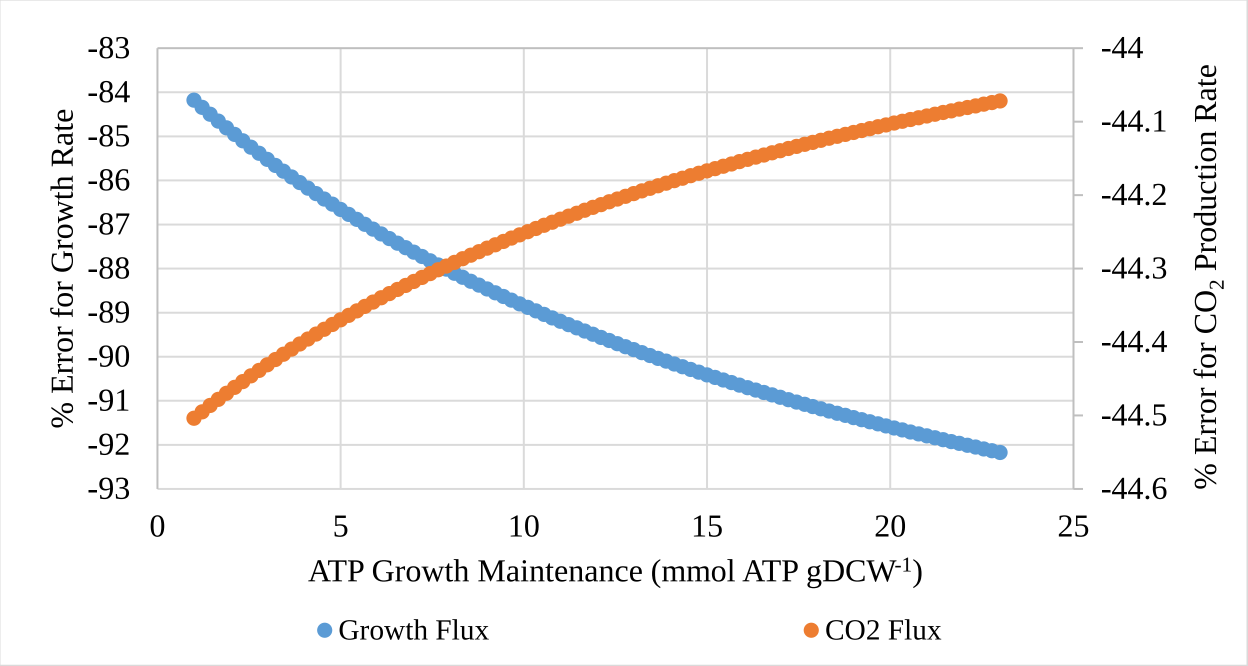

Figure 43: a) Predicted growth and specific CO_2 production rates associated with various ATP growth maintenance coefficients for Condition 4a from Case 2. b) The associated % error from the predicted fluxes compared to measurements from condition 4a in Case 2.

Regardless of the low ATP coefficient for growth maintenance, the predicted growth and specific CO_2 production rates remain largely under predicted when compared to measured values. Growth rate error improves till an error of -85% with maintenance values of 1 mmol g DCW^{-1}, while CO_2 error drops less than a percentage point. Thus, the ATP growth maintenance value has little to no impact on the energy issue at hand.

The flux value for the non-growth maintenance terms was calculated based off the assumption that 6 mol ATP are produce per mole of CH_4 [108].This assumption was applied on the intercept term of Figure 35 calculated by the measured data from Case 2. From this assumption a large amount of ATP is required that challenges the feasibility of aerobic respiration with the gas inputs. Thus, the non-growth maintenance term was varied in the model to evaluate the effect on predicted growth and specific CO_2 production rates, and in turn appraise the presumed ATP/CH_4 ratio. The results of this analysis are shown in Figure 44.

a)

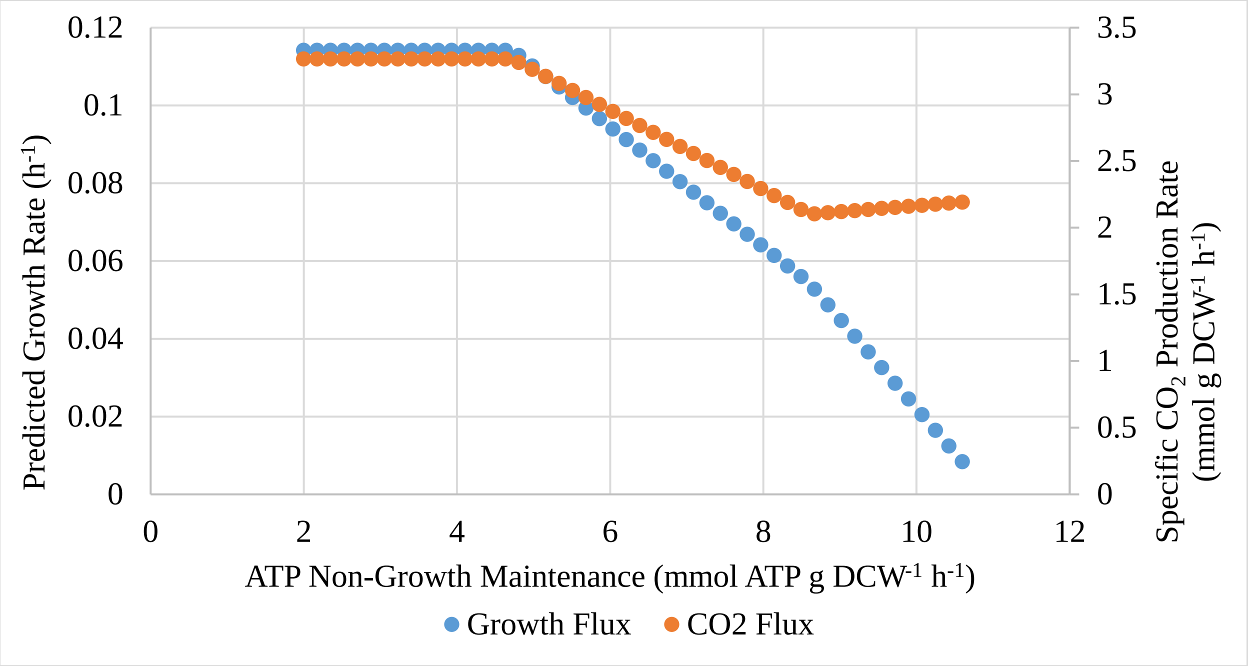

b)

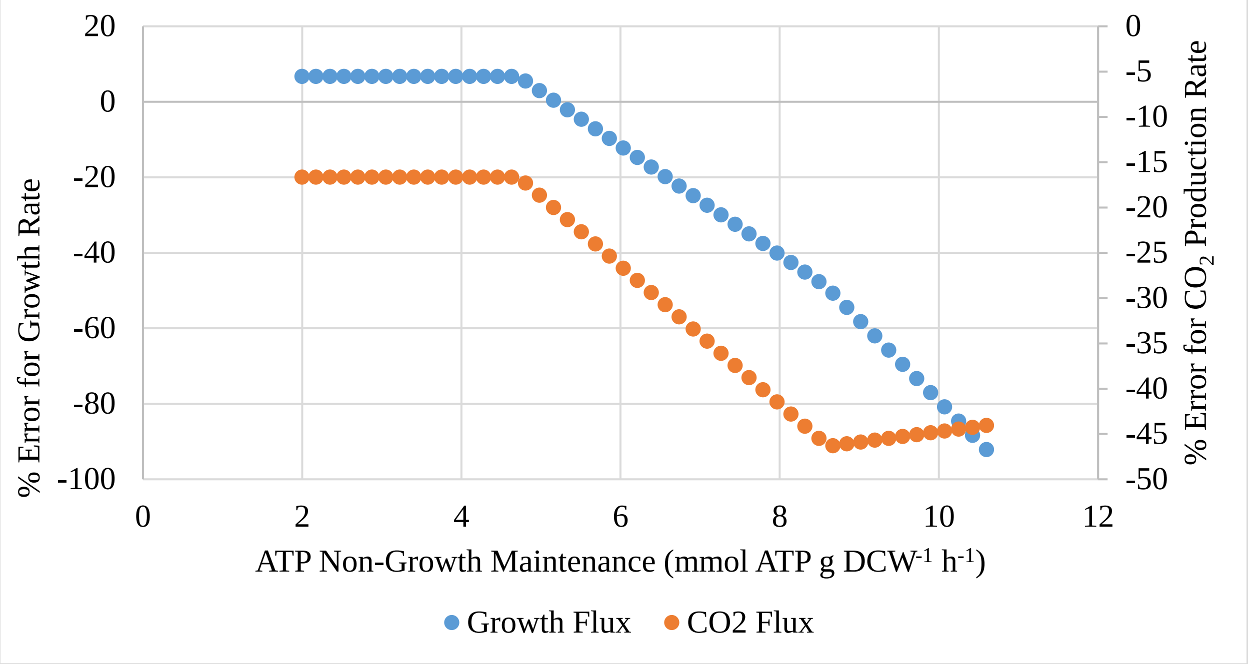

Figure 44: a) Predicted growth and specific CO_2 production rates from various ATP non-growth maintenance terms for Condition 4a from Case 2. b) The associated % error from the predicted fluxes compared to measurements from Condition 4a in Case 2.

As displayed in the figure above, the growth rates drastically increased with lower ATP non-growth maintenance. Values of 4.87-5.56 mmol ATP g DCW^{-1} h^{-1} would give within ± 5% error from measured values which would require the ATP/CH_4 yield to change from 6 to 2.76-3.15. The specific production rate of CO_2 increased to a new consistent flux value at which time the error remained about -17%. The same approach was conducted for the other days of steady state data for Conditions 4-6 and a similar conclusion can be drawn.

Condition	Non-Growth Maintenance for ± 5% Measured Growth Rate	Calculated ATP/CH_4 Yield Required for ± 5% Measured Growth Rate	Final % Error for Predicted CO_2
4a	4.87-5.56	2.76-3.15	-16.67
4b	2.00-6.78	1.13-3.84	-14.17

4c	5.65-6.26	3.20-3.54	-15.07
5a	6.00-6.78	3.34-3.84	-16.61
5b	5.91-6.60	3.35-3.74	-16.00
5c	5.30-6.08	3.00-3.44	-18.10
6a	2.00-13.89	0.77-5.37	-7.52
6b	12.11-12.93	4.68-5.00	-9.62
6c	11.98-12.80	4.63-4.95	-10.44
6d	2.00-13.34	0.77-5.15	-7.22

Table 20: Effect of ATP non-growth maintenance for Conditions 4-6 of Case 2.

Though no direct measurement of ATP/CH_4 ratio was completed in this study, a few questions remain about the validity of changing the original assumed methane to ATP yield. Recall in Tables 15 and 17, the previously assumed value of 6 brought forth excellent predictions for oxygen pickup, growth, and carbon dioxide production rates for Condition 1. This same condition was used alongside Conditions 4 and 5 in Figure 35 to obtain the original non-growth maintenance term. So why would the ratio change for only a portion of the points on the original line? Additionally, the non-growth maintenance change did not properly account for the CO_2 produced in any state (see Table 20), suggesting that the non-growth maintenance term is not the only one that may significantly affect the energy limitation and carbon flow within the genome scale metabolic model.

6.6 Installation of Nitrate as a Theoretical Electron Acceptor

Denitrification via hybrid respiration is the process of breaking down nitrate to gaseous nitrogen with electrons by the electron transport chain. Recent evidence of methanotrophs conducting these actions have been observed by Kit et. al [128]. With the hybrid respiration, methanotroph can use nitrate as an alternative terminal acceptor funneling their oxygen dependence largely to oxidize methane. Currently this respiration route has not been examined in literature for 5GB1. However, some proposed routes of the structure and efficiency with other microorganisms has been constructed [129].

Despite the lack of current genetic evidence of hybrid respiration in 5GB1, an attempt was made in this work to summarize the possible routes into an additional reaction in the stoichiometric matrix. In doing so, an *in silico* approach is adopted to evaluate whether the predictions for growth and carbon dioxide production rates would improve for Conditions 4-5 of Case 2 with the restrictions of methane and oxygen pickup rates.

To install this hybrid respiration route into the metabolic model two summary equations were developed based on the stoichiometry of denitrification (see Appendix C). Both routes include the use of nitrate reductase (NAR), nitrite reductase (NIR), and nitric oxide reductase (NOR). What differentiates the two routes considered is the last enzyme of denitrification. The first includes nitrous oxide reductase (NOS) that breaks down nitric oxide to diatomic nitrogen, while the second contains nitric oxide dismutase (NOD) that creates both nitrogen and one-half molecule of oxygen. The latter, generates a feed-back loop for further aerobic respiration or methane oxidation. In doing so, the following summarized equations were formulated (with key assumptions covered in Appendix C).

NAR->NOS-> ATP

$$\begin{aligned} 2NO_3 + 48H_c^+ + 5NADH + 10.9\,ADP + 10.9\,P_i \\ \rightarrow N_2 + 6H_2O + 36\,H_c^+ + 10.9\,ATP \end{aligned} \tag{22}$$

NAR->NOD-> ATP

$$\begin{aligned} 2NO_3 + 40H_c^+ + 4NADH + 9.1\,ADP + 9.1\,P_i \\ \rightarrow N_2 + 0.5O_2 + 5H_2O + 30\,H_c^+ + 9.1\,ATP \end{aligned} \tag{23}$$

After implementing either Equation 22 or 23, the same methane and oxygen pickup rates for Conditions 4-6 from Case 2 were inputted into the modified model. It should be noted that non-growth maintenance was set based off the conditions in Figure 35, growth maintenance was low (coefficient of 23), and the yield for aerobic respiration remained untouched. The numerical results are listed in Table 21 and illustrated in Figure 45. From the tables below, the predicted growth rates for either routes of hybrid respiration improved significantly, reducing error to -13.3 to -2% error. The corresponding carbon dioxide flux also approached measured values with errors reducing to within 6%.

a)

	Typical Aerobic Respiration		NAR to NOD		NAR to NOS		Measured
	Growth Flux	% error	Growth Flux	% error	Growth Flux	% error	Growth Rate
4a	0.008	-92.52	0.095	-11.44	0.093	-13.30	0.107
4b	0.039	-63.21	0.095	-10.05	0.094	-11.47	0.106
4c	0.024	-76.92	0.096	-7.86	0.094	-9.56	0.104
5a	0.054	-55.37	0.114	-6.01	0.112	-7.34	0.121
5b	0.048	-60.00	0.116	-3.20	0.114	-4.67	0.120
5c	0.036	-70.25	0.114	-6.04	0.112	-7.64	0.121
6a	0.092	-24.59	0.120	-1.72	0.115	-5.47	0.122
6b	0.074	-38.33	0.117	-2.43	0.116	-3.44	0.120
6c	0.074	-39.34	0.119	-2.66	0.118	-3.68	0.122
6d	0.081	-33.06	0.116	-3.86	0.119	-1.57	0.121

b)

	Typical Aerobic Respiration		NAR to NOD		NAR to NOS		Measured
	CO_2 Flux	% error	CO_2 Flux	% error	CO_2 Flux	% error	CO_2 Rate
4a	2.19	-44.06	4.03	2.92	4.11	4.94	3.92
4b	2.17	-44.99	3.96	0.51	4.02	2.02	3.94
4c	2.19	-44.22	4.02	2.22	4.09	4.00	3.93
5a	2.43	-46.27	4.39	-2.92	4.46	-1.51	4.53
5b	2.48	-45.22	4.47	-0.98	4.54	0.57	4.52
5c	2.45	-45.86	4.44	-1.79	4.52	-0.12	4.53
6a	4.12	-20.91	5.13	-1.69	5.16	-1.09	5.21

6b	3.61	-30.11	5.13	-0.65	5.18	0.28	5.17
6c	3.59	-31.46	5.18	-1.28	5.23	-0.34	5.24
6d	3.82	-24.60	5.08	0.36	5.12	1.14	5.06

Table 21: Results with methane and oxygen pickup rates constrained with hybrid and aerobic respiration. a) Growth rates (h^{-1}) predicted and comparison. b) Carbon dioxide production rates (mmol $gDCW^{-1}$ h^{-1}) predicted and comparison

a)

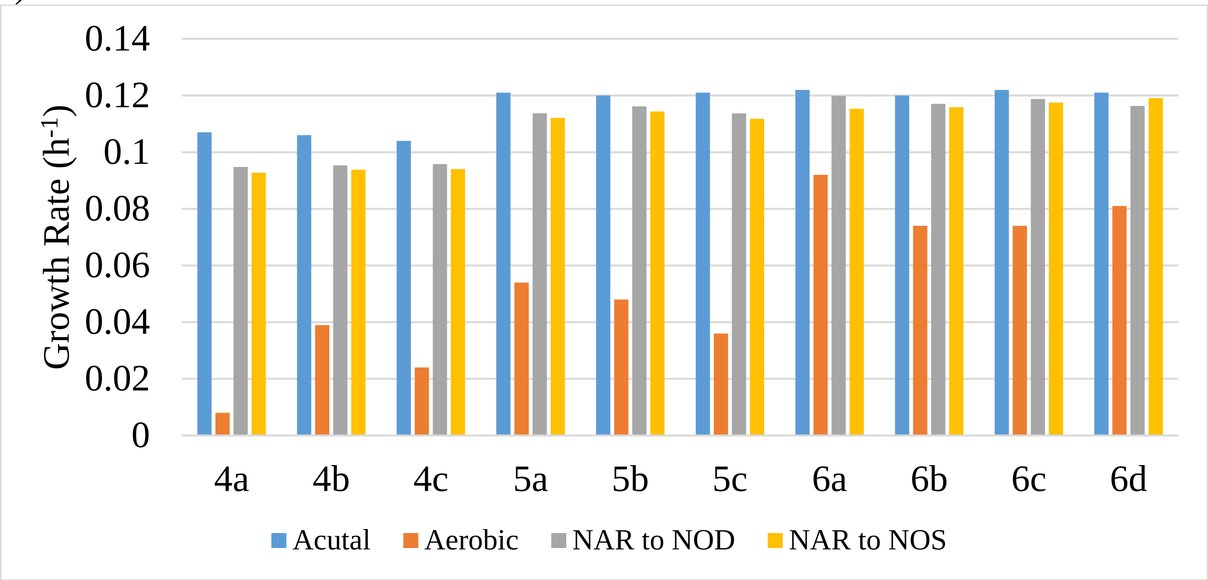

b)

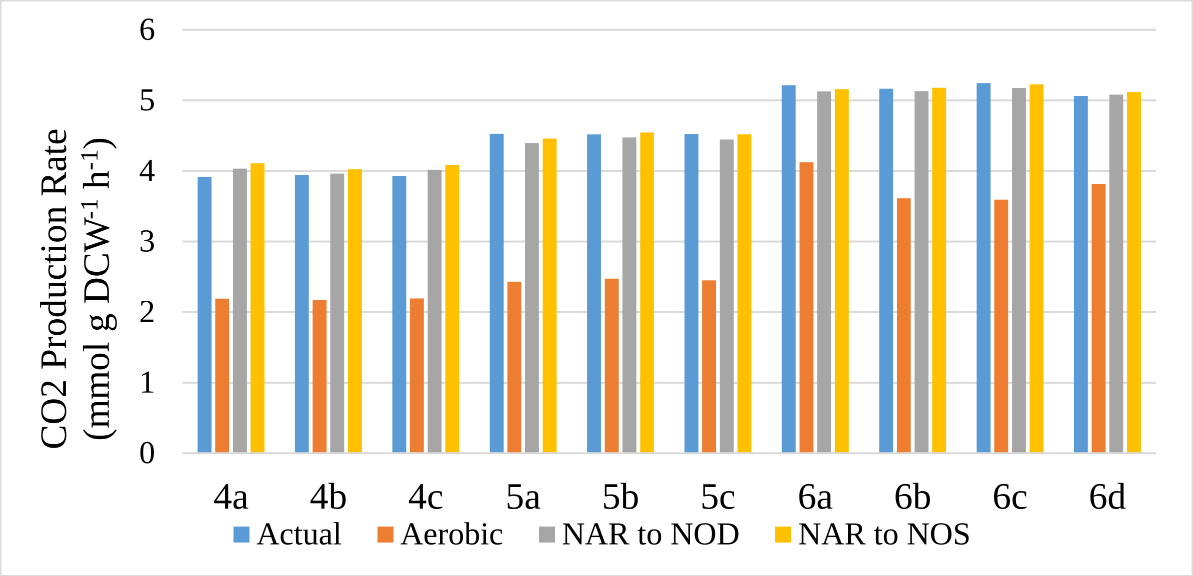

Figure 45: Results with methane and oxygen pickup rates constrained with hybrid and aerobic respiration. a) Growth rates (h^{-1}) predicted and comparison. b) Carbon dioxide production rates (mmol $gDCW^{-1}$ h^{-1}) predicted and comparison.

With the improved accuracy in models due to the installed hybrid respiration, flux analysis of the whole network was conducted to evaluate if flux values vary drastically from optimal solutions (i.e. when methane is the only input). Comparison of reaction fluxes that utilize ATP are listed in Table 22 for Conditions 4a and 5a.

a)

Rxn Notes	Optimal Solution (M Input)	Aerobic M+O Input	NAR to NOD M +O Input	NAR to NOS M+O Input
Aerobic ATP Production	11.230	6.286	7.636	6.264
Nitrification/ATP	-	-	4.163	4.592
Succinyl-CoA synthetase	1.041	-0.001	1.124	1.155
Acetate Kinase	0	1.811	0	0
Acetyl CoA Carboxylase	-0.260	-0.022	-0.246	-0.241
Pyruvate Carboxylase	-0.255	-0.021	-0.241	-0.236
Nitrate Transporter	-0.705	-0.386	-1.583	-1.663
Non-Growth Maintenance	-10.6	-10.6	-10.6	-10.6
Growth	-2.303	-0.193	-2.180	-2.134

b)

Rxn Notes	Optimal Solution (M Input)	Aerobic M+O Input	NAR to NOD M +O Input	NAR to NOS M+O Input
Aerobic ATP Production	11.553	7.558	8.651	7.542
Nitrification/ATP	-	-	3.363	3.709
Succinyl-CoA synthetase	1.134	-0.010	1.201	1.226
Acetate Kinase	0	2.052	0	0

Acetyl CoA Carboxylase	-0.307	-0.141	-0.296	-0.291
Pyruvate Carboxylase	-0.301	-0.138	-0.290	-0.286
Nitrate Transporter	-0.832	-0.423	-1.540	-1.605
Non-Growth Maintenance	-10.6	-10.6	-10.6	-10.6
Growth	-2.715	-1.250	-2.616	-2.579

Table 22: Influential reactions that generate or consume ATP for a) Condition 4a and b) Condition 5a. Methane (M) alone or methane and oxygen (M +O) pickup rates were inputted to the model.

Production of ATP in the hybrid routes (i.e. the sum of the first two rows of column 4 or 5 for the above tables) closely matched those of the optimal solution in the original model (i.e. the first row of the second column). Additionally, the flux values of intermediate reactions, such as succinyl-CoA synthetase, acetyl CoA carboxylase, and pyruvate carboxylase, were similar to those of the optimal solution. The key difference being the nitrate transporter, which would be required for the new hybrid respiration to work. The other reactions in the model, not listed in the table above (>400) do alter slightly from the optimal solution fluxes by 7-10% with hybrid respiration. Despite this difference, the central carbon network in flux map below in Figure 46 is similar to the optimal solution map in Figure 36.

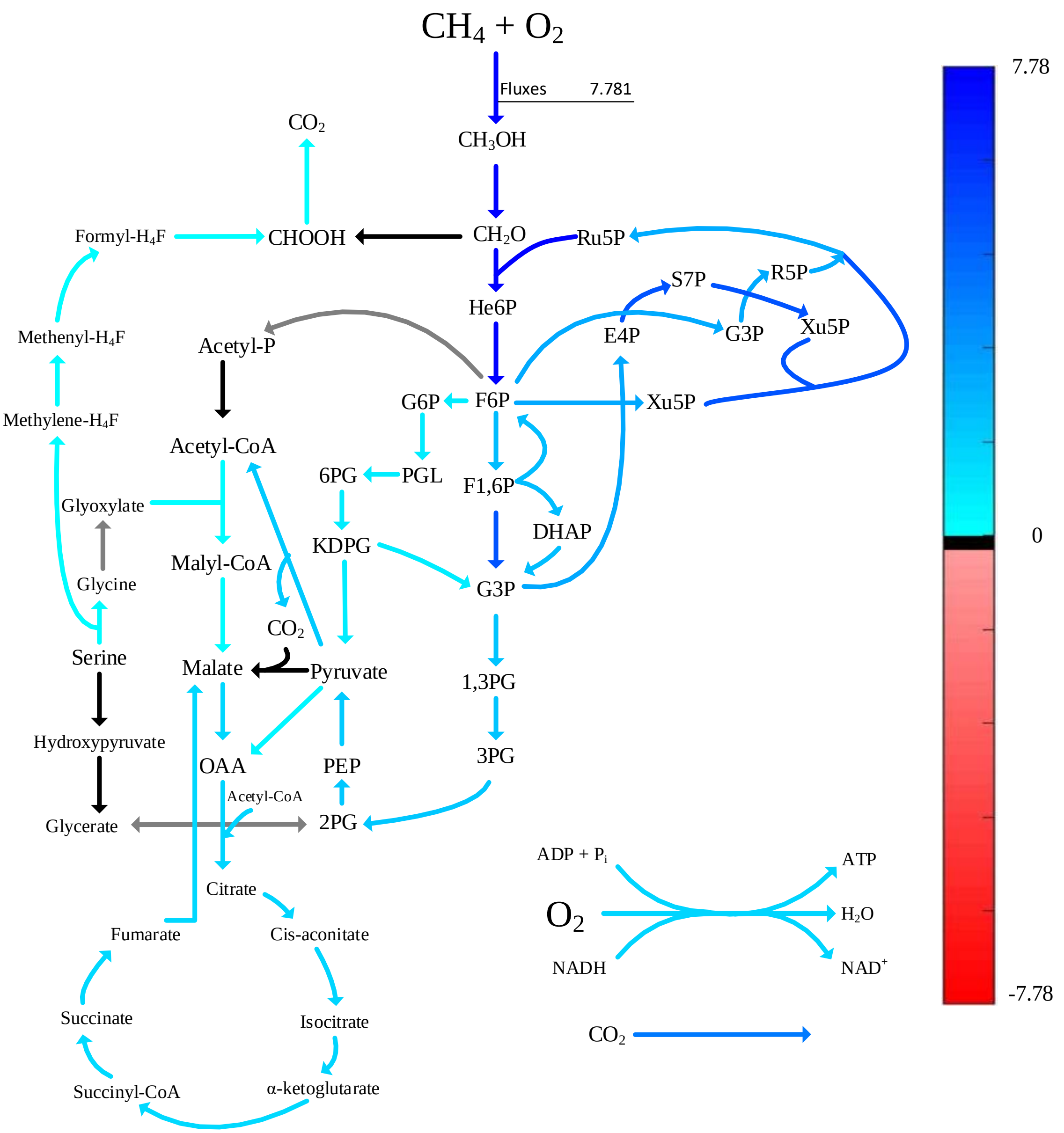

Figure 46: Sample flux map of NAR-> NOD for hybrid respiration for Condition 4a from Case 2. The blue indicates positive fluxes and the reaction proceeds in the direction of the arrow. Red fluxes (if any) would indicate flux flows opposite of the arrow direction. Black arrows carry no fluxes and grey arrows are outside of the model stoichiometric matrix.

Finally, a small note should be taken that this hybrid respiration was also applied to Condition 6 where dissolved oxygen was not zero as it was in Conditions 4 and 5. Instead, the dissolved oxygen levels was measurable and remained close to 8% for over five days. If this alternative respiration was possible for Condition 6, it would suggest that the enzymes for denitrification has some level of oxygen tolerance [133]. This makes Condition 6 unique from the other methane deprived conditions (Conditions 2 and 3) where no denitrification was required to improve prediction accuracies. The reason it may exist solely for Condition 6, may be due to genetic carry over from Condition 5 that was not possible in Condition 2 or 3. Recall, Conditions 2 and 3 are cells that transitioned from Condition 1 that exhibited minimal prediction errors with the use of typical aerobic respiration and thus, showing ample energy production.

6.7 Assessment of Model Performance with Abundance of Oxygen

Table 15 illustrated that with methane depleted Conditions 2 and 3, a difference in carbon distribution occurs when compared to measurable values, i.e. more carbon was directed towards CO_2 production (positive errors) than growth (negative errors). To evaluate the overall flux distribution difference, the central core carbon network was plotted in Figure 47. The map shows a significant amount of carbon is diverted away from the RuMP cycle, TCA cycle, or the EMP/EDD pathways. Instead it is immediately converted to formate via formaldehyde oxidation from the H_4MPT pathway producing a lot of reducing power that then becomes carbon dioxide. This suggests that the abundance of oxygen relates to a reducing power requirement. As stated before, any oxygen leftover after methane oxidation is almost entirely consumed by the aerobic respiration that in turn requires a certain supply of NADH. FBA was done to gauge how influential this aerobic reaction was on reducing power consumption and the results are listed in Table 23.

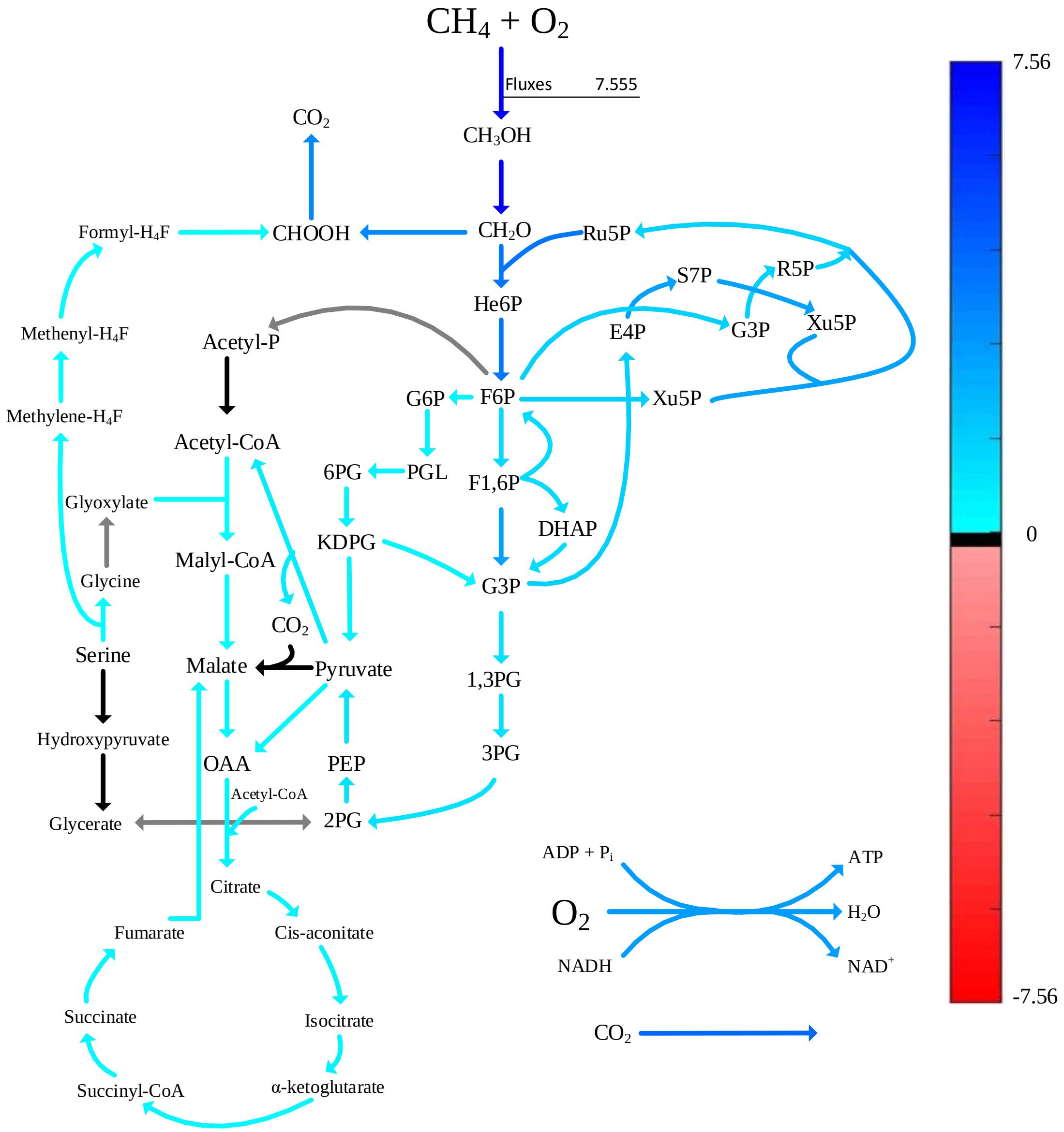

Figure 47: The central carbon network for Condition 2a. The blue indicates positive fluxes and the reaction proceeds in the direction of the arrow. Red fluxes (if any) would indicate flux flows opposite of the arrow direction. Black arrows carry no fluxes and grey arrows are outside of the model stoichiometric matrix.

Rxn Name	Rxn Notes	Flux Value m+o input	Flux Value m input
'RXN__45__2883'	Formaldehyde H_4MPT pathway	3.481	0.000
'_1__46__2__46__1__46__2__45__RXN'	Formate Dehydrogenase	3.495	0.015
'GAPOXNPHOSPHN__45__RXN'	EMP (GAP to DPG)	0.889	1.749
'RXNN0B__45__102'	ATP Equation	-5.847	-5.111
'RXNN0B__45__29'	Pyruvate to Acetyl CoA	0.535	1.630
'MALATE__45__DEH__45__RXN'	TCA (Malate to OAA)	0.182	1.249
'FUMARATE__45__REDUCTASE__45__NADH__45__RXN'	TCA (Succ. to Fum.)	0.163	1.228
'_2OXOGLUTARATEDEH__45__RXN'	TCA (α-keto. to Succ. CoA)	0.155	1.220
'_1__46__6__46__1__46__2__45__RXN'	NADH to NADPH reaction	-0.571	0.699

Table 23: Key reactions responsible for the majority of NADH consumption and production for Condition 2a of Case 2. Methane (m) or methane and oxygen (m +o) pickup rates were constrained.

With the restriction of methane and oxygen, the ATP equation generated a flux that required 57.4% of all NADH compared to the previous 51.67% when methane was the sole input. Consequently, more CO_2 is formed with fluxes that involve direct reducing power generation, increasing the accumulated positive flux from 4.245 to 4.489. A similar trend is observed with the other steady state data sets for Conditions 2 and 3, where the percent of reducing power and the fluxes associated with carbon dioxide production increase (see Table 24). Thus, for Conditions 2 and 3, the additional methane and oxygen constraints increased NADH consumption for ATP production and in turn increased the associated CO_2 flux.

	Total Flux of NADH Consumed		% NADH Required for ATP Production		CO_2 Flux Associated with NADH	
Condition	M Input	M + O Input	M Input	M+O Input	M Input	M+O Input
2a	9.89	10.19	51.66	57.38	4.22	4.47
2b	9.98	10.08	51.32	57.18	4.26	4.47
2c	9.96	9.74	51.40	57.75	4.25	4.42
3a	11.37	14.61	46.47	48.59	4.87	5.95
3b	11.11	14.28	47.29	51.26	4.76	5.88
3c	11.13	14.21	47.21	49.33	4.77	5.81

Table 24: Comparison of reducing power and associated carbon dioxide production for results from methane input only (M) and methane and oxygen (M + O) inputs. All fluxes are in units of mmol gDCW^{-1} h^{-1}.

With the current model, it is unclear how carbon distribution with the excess oxygen could be manipulated to match experimental values. An attempt to alter EMP/EDD ratios would only create the same reducing power requirement and thus would have minimal effect (data not shown) [66]. One attempt to restrict oxygen in the respiration equation for Condition 2a sent excess oxygen to other carbon costly avenues that in turn created a drastic decrease in predicted growth rate generating a large error (~-25%), though carbon dioxide flux dropped to within 3% of the measured values. Thus, other routes should be introduced into the model that removes excess oxygen in a way that limits carbon loss. Such routes may relate to hydrogen peroxide production where no carbon is spent. However, hydrogen peroxide is often harmful to cell viability and this mechanism is currently not stated within the covered literature.

6.8 Discussion and Conclusions from Genome Scale Metabolic Modelling

In this chapter the reduced metabolic model was assessed with chemostat data from Cases 1 and 2 covered in Chapter 5. Results from i*n silico* experiments that were constrained with methane pickup alone, could not match measured growth, oxygen pickup, and carbon dioxide production rates. Analysis of the phenotype phase plane for Case 2 demonstrates that two fluxes are necessary to plot the location of actual data points since they are not positioned on the line of optimality, regardless if methane or oxygen is the deprived substrate.

With both methane and oxygen restricted, two types of errors were found. Conditions 4-6 experienced a significant lack of energy production due to limited oxygen supply. Varying the yield of ATP from methane allowed the non-growth maintenance term to be adjusted. This influential flux value significantly improved the predictions on growth rate, however the change in carbon dioxide production rate plateaued leaving errors over >10% for most conditions. However, a theoretical hybrid respiration with nitrate improved not only the predicted growth rate, but also the carbon dioxide production rates (usually < 10% error). Despite this progress, there is no evidence in current literature that suggests the mechanisms exist and biological research is necessary for validation.

Conditions 2 and 3 experience issues that are relatively opposite in behavior. With the measured excess oxygen, a larger demand for NADH utilized for ATP production was created. The uptick in necessary NADH increased flux values to CO_2, diverting carbon away from the biomass equation. The current model does not have internal mechanisms that dispose of this oxygen without loss of carbon and alterations are required to efficiently rid of the excess oxygen. However, there is currently a lack of biological information to implement any solutions.

Chapter 7 : Overview of Conclusions and Closing Remarks

7.1 Final Observations Noted and Objectives Completed

Methylomicrobium buryatense 5GB1 is considered a promising industrial methanotroph strain because of its rapid growth, versatile productivity, and ability to thrive in harsh environments. In this study a systematic characterization on growth and carbon distribution was constructed for batch and continuous systems. Specifically, the objectives were to: 1) Investigate the effects of methane and oxygen on cellular behavior. 2) Provide data on carbon distributions for cultures under oxygen or methane deprived conditions in both batch and continuous systems. 3) Perform *in silico* analysis with the reduced genome scale metabolic model based off data accumulated with the continuous chemostat.

Completion of these objectives required both tool development, such as the gas mixing system, and accurate evaluation of the gaseous headspace. For batch cultures, a vacuum would exist in the final state after considerable bacteria growth and withdrawn liquid samples. Re-pressurization with nitrogen proved to be an efficient way to measure the three gas components of interest (methane, oxygen, and carbon dioxide) and was thus used for vial culture analysis. Additionally, effluent gas streams are noticeably reduced when sparged through a continuous chemostat. Accurate measurement of the gas flow was obtained through a simple mass balance of helium that acted as an inert standard within the gas stream. In doing so, careful carbon balances were conducted for two case studies with multiple days of steady state.

With detailed analysis of vial cultures, it was observed that oxygen concentration, rather than methane concentration, can influence both growth and carbon distributions. In general, the increasing oxygen levels led to decreasing peak growth rates, though high biomass was still achieved by stationary phase. Additionally, the calculated carbon conversion efficiencies remain relatively consistent till oxygen tension becomes overbearing and an obvious change in phenotype occurred. Beyond this exception, the carbon yields to biomass remained close to 46% and carbon dioxide close to 50%.

Continuous chemostat runs with the use of helium as an internal standard were operated at both methane and oxygen deprived conditions. Within this experiment, it was observed that a degree of metabolic versatility for methanotrophs exist as exhibited by the pickup ratios for the gaseous substrates. From the data, it appears that gas presence alone does not dictate behavior but also the genetics of the cells from the previous experimental state. This adds a degree of complexity that was not observed with typical gas fermentation theory and thus may explain why conversion rates did not change in the proportional manner expected. Despite everything, the carbon conversion efficiencies for all conditions ranged between 47-51%, which is analogous to vial cultures.

In silico assessment of the genome metabolic model with methane and oxygen constraints matched the versatility observed with continuous cultures. Phenotype phase plane analysis confirmed that pickup rates do not position along the line of optimality, but tend to deviate pending on the oxygen pickup behavior. Conditions that lacked oxygen suffered from restricted ATP production, creating an inefficient pathway for energy generation at the cost of carbon for biomass growth. However, alterations of the non-growth maintenance flux or installation of a theoretical hybrid respiration route improved predictions for both growth and carbon dioxide production rates. However, biological evidence is required to prove the viability of either notion. On the other hand, excess oxygen utilized for ATP production via aerobic respiration, created a larger demand for NADH that in turn, funneled more carbon to CO_2 and away from biomass. It was determined that the current model does not have internal mechanisms that dispose of this oxygen in an efficient carbon-based manner.

7.2 Recommendations for Future Work and Closing Statement

Future progress can continue on both the biological and process system sides of methane bioconversion via methanotrophs. On the biological front, future experimentation can be done to explore the metabolic shift observed when adjusting from oxygen deprived to methane deprived conditions. Of particular interest, is the identification of the intercellular mechanisms that produce energy when cells undergo higher dilution rates with a severely limited oxygen supply. Does a hybrid respiration chain exist for 5GB1? Many answers could possibly be found through transcriptomic studies from cell samples of systems analyzed and controlled by mechanisms proposed in this study. Specifically, organisms can be harvested while under two steady state conditions and the transition period in between. Additionally, analysis of fatty acid composition would be especially beneficial, as genetic engineering methods are currently being sought to improve the yields [38].

For process considerations, the most important goal is to increase the solubility of methane and oxygen to methanotrophs within the liquid broth. In Case 2 of Chapter 5, about 14-22% of all carbon introduced to the system was assimilated. This could be improved with enhanced bioreactor design, or with the addition of promoting agents, as discussed in Chapter 1. It should be noted, only 8-11% of assimilated carbon is distributed to lipids for potential biodiesel production [14,29]. In this study, about ~45-50% of the assimilated carbon was sent to biomass, thus ~5% of the assimilated carbon and 0.7-1.1% of the fed carbon could possibly go towards lipid production. Thus, improving gas transfer would increase the carbon flux not only to lipids for biodiesel production but also to processes that use methanotrophs for single cell protein [23].

For environmental abatement or removal of methane, methanotrophs could serve as potential biocatalysts as long as the process enhances gas transfer or implement gas recycling. If the data achieved here could be scaled appropriately, about half of all methane would be removed to biomass, while the other half is released as a less impactful greenhouse gas, CO_2. Thus, the global warming potential of the influent gas stream is dropped dramatically. To improve conversion efficiencies, genetic engineering could be utilized to redirect carbon towards biomass or organic production. Others have also attempted to move the methane assimilating pathways to efficient model organisms such as, *E. coli* or yeast, but progress thus far has been limited [20].

Considering the amount of carbon directed to carbon dioxide, 70-80% are easily accessible in the liquid phase, processes that utilize the effluent gas and/or liquid carbonate would add value to methanotroph systems. Two such processes include co-culture biocatalysts and mineralization methods.

Recently, promising research have paired methanotrophs to algae/cyanobacteria in an effort to improve yields and increase productivity capabilities [134–136]. The relationship works well as carbon dioxide is a natural product of methanotrophs that can be assimilated by the photosynthetic organisms. In return, algae/cyanobacteria can provide oxygen to the methanotrophs in a dissolved format that avoids problems with gas transfer that currently plague the single organism system. This opens the possibility of fully utilizing the carbon in renewable biogas in a symbiotic biological process. However, the research published thus far was completed under continuous illumination, and there has not been any systematic study on the factors (such as headspace composition or specific strain pairing) that could affect the stability and performance of the co-cultures. Additional factors of interest include inoculation ratio, gas phase composition, and illumination regimes. These systems bring further challenges, such as how to quantify single cell concentrations and their individual pickup and production rates. This remains a complex problem, though some work on the first half was conducted with a novel sensor approach that was developed and explained in Appendix D [137].

As another avenue, recent literature suggests that biotechnology can be applied for cement manufacturing. Thus, a conceivable process can be developed from carbonate byproducts of methanotrophs. Carbonate can be mineralized, such as with calcium, to form precipitants valued by the cement and aggregate industry as those process with ureolytic bacteria [138,139]. Through biotechnological mineralization, calcium carbonate from methanotrophs can become a sustainable source of precipitants for cement to build infrastructure around the world [140].

By use of these proposed processes, methane abatement could potentially become an economic drive towards sustainability. Instead of focusing on the 50% of carbon captured for biomass and organic products, while inherently dealing with 50% carbon loss, a potential system could be developed to utilize 90% of the assimilated carbon.

Advanced research has elevated carbon monoxide fermentation from bench scale experimentation to profitable industrial biotechnology [141] and could serve as a role model for future success of methanotroph based systems. In doing so, progress will be required from both biological and process perspectives to create a path forward that will guide methane fermentation from the realm of ideas to one of practicality.

Appendix A: Notes Regarding Inoculum/DO ratio

This section serves as a note on observed behavior regarding the sensitivity of the cells to the initial biomass/DO ratio for chemostats. From the experiences generated in this study, two bioreactor runs outside of Case 1 and 2 were completed. These experiments allowed for standardization of equipment and sample protocol.

Once inoculated, the cells are operated in a batch mode and in doing so, are expected to follow a traditional exponential growth curve. However, it was observed during one run that with excess oxygen and lower biomass amount, cells are thrown from a typical growth and enter a new phenotype in which large amounts of organic carbon matter are created (presumably EPS). For example, when the cells were inoculated with conditions of 1.29 mmol O_2 $gDCW^{-1}$ a typical growth curve is observed (shown in Figure A1) with peak specific growth rates of 0.2 h^{-1} and a stationary growth phase reached at ~23 hours. However, when cells were inoculated with conditions at 2.4 mmol O_2 $gDCW^{-1}$, peak growth rates were only 0.07 h^{-1} and a much slower biomass growth seen (Figure A2).

Figure A1

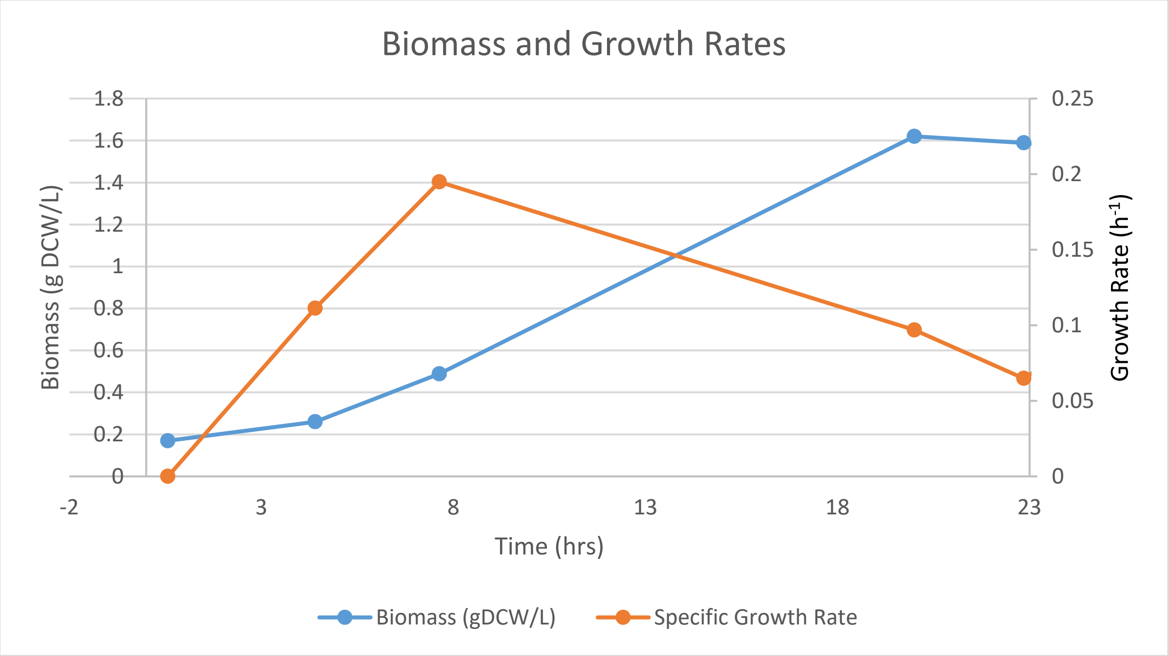

Figure A2

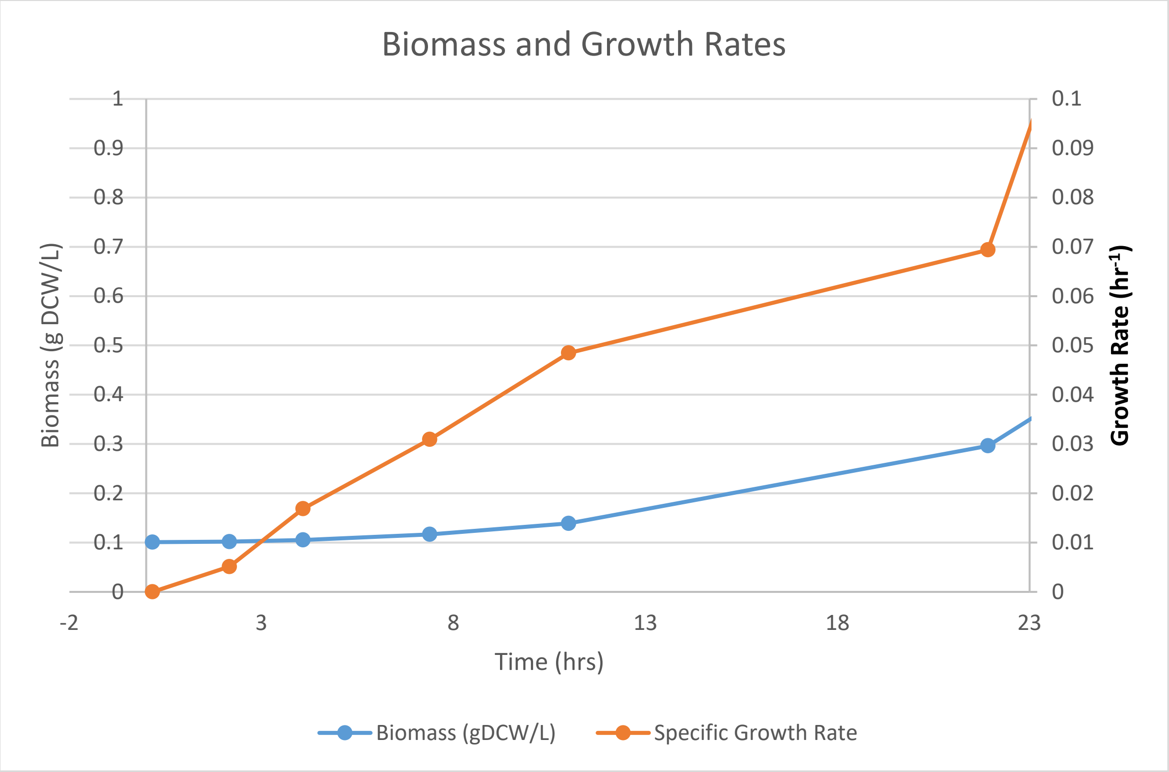

Upon observing the slower growth rate, oxygen supply was decreased and dilution rate increased slowly. However, the cells continued to grow slowly and accompanied a larger than normal organic carbon production (see Figure A3 and A4). In doing so, large foaming would occur over night, leading to frequent manual injections of antifoam. The organic carbon produced reached peak levels of 1g/L before a transition from the cells caused by the increased stress of higher dilution rates and lower oxygen content started to increase inorganic carbon production. Unfortunately, the pH loop malfunctioned at about 100 hours and the experiment was ceased.

Figure A3

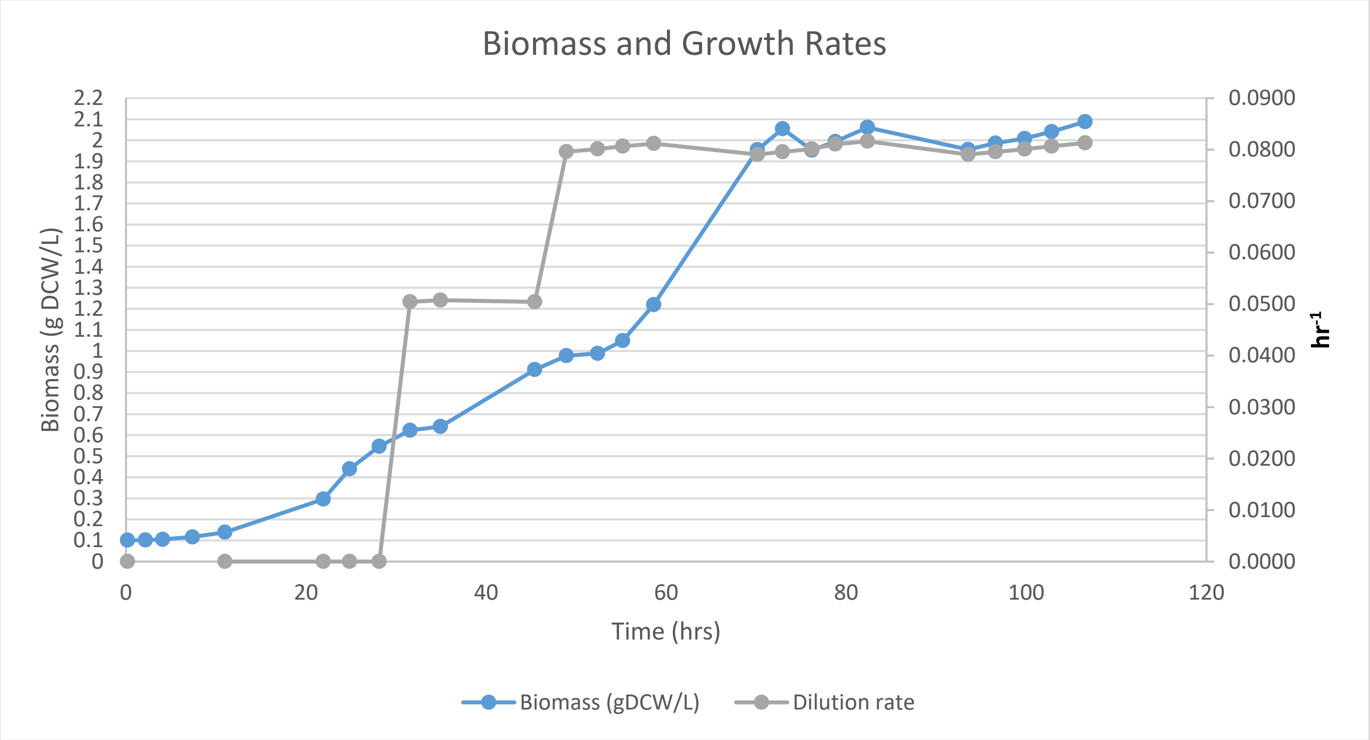

Figure A4

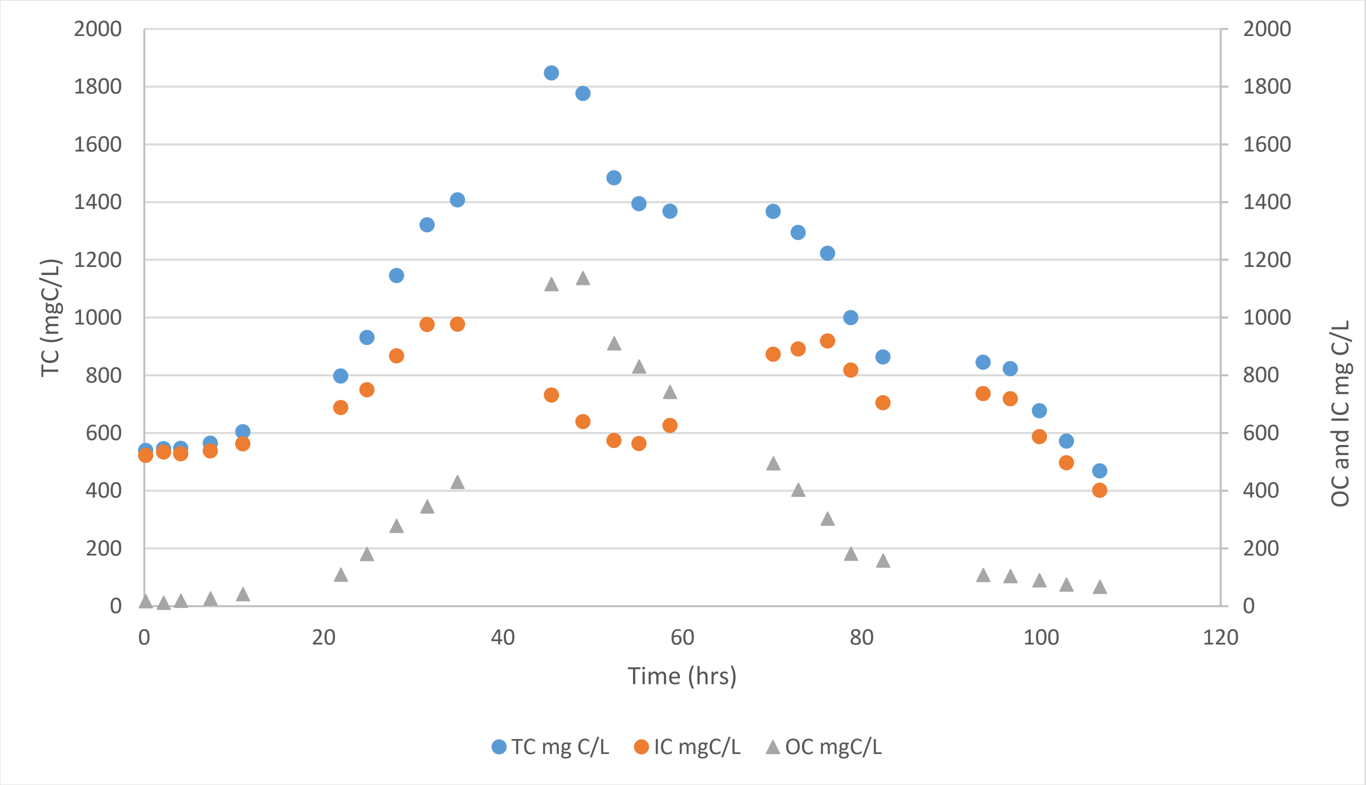

Figure A5

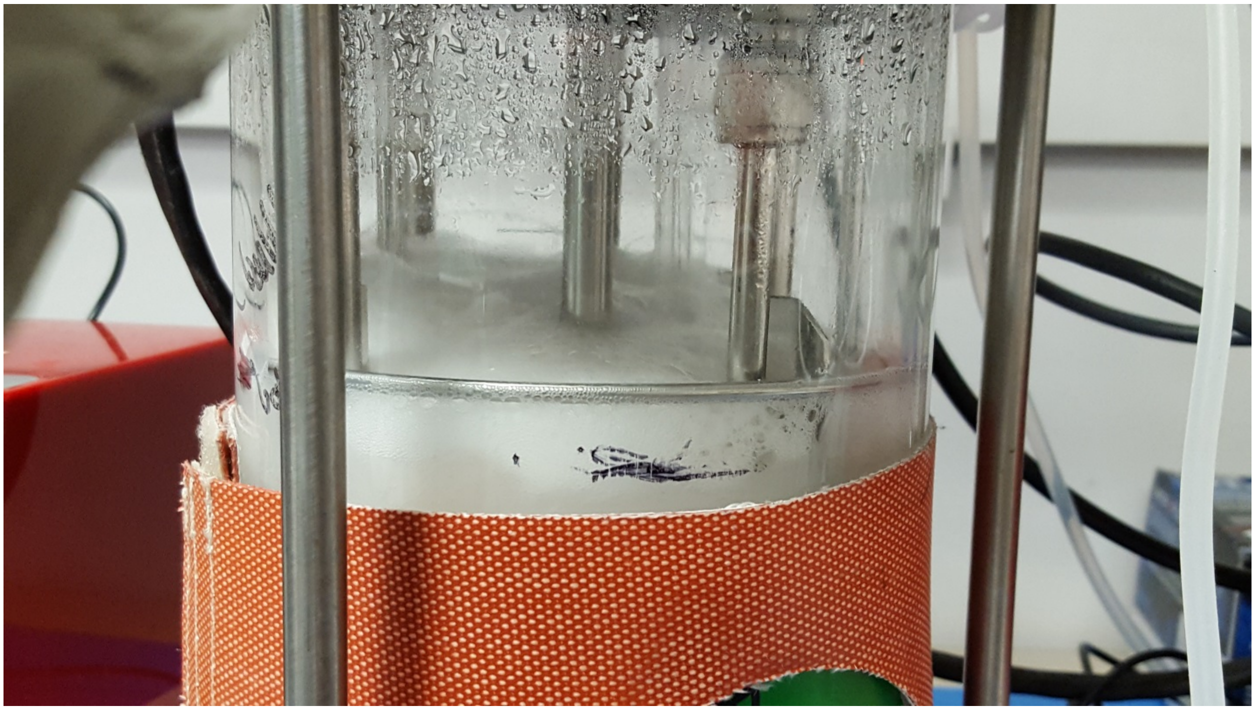

Appendix B: Carbon Balance for Chemostat Cases

The carbon balance is achieved through direct measurement of headspace, liquid carbon, and biomass. Below is the summary of the system of equations used to properly account for the carbon produced and consumed by the system.

Flow into bioreactor

$$F_{in} = Total\ Gas\ Flow\ \left(\frac{smL}{min}\right) * \left(\frac{P}{RT}\right)$$

Where P and T are values from standard conditions, 1 atm and 25°C, respectively, and R is the universal gas constant. Flow rate is in mmol/min.

Effluent flow from bioreactor

$$F_{out} = \frac{y_{He_{in}} * F_{in}}{y_{He_{out}}}$$

$$y_{He_{out}} = \left(\frac{n}{V}\right)\frac{R * T_{meas}}{P}$$

The concentration (n/V) of helium is determined by the GC. The temperature is measured from the gas stream out of the condenser and pressure is atmospheric. Again, flow rate is in mmol/min.

Gaseous methane balance

$$F_{in} * y_{CH_{4in}} * (t_2 - t_1) - F_{out} * y_{CH_{4out}} * (t_2 - t_1) - V_{Headspace} * \Delta C_{CH4} = CH_4 consumed$$

The mole fraction of methane into the system is defined by the fraction (in smL/min) of the total flow rate and set by the mass flow meter in the mixing system. The mole fraction of methane in the effluent stream is measured by GC and is calculated analogous to helium. The outlet mole fraction applied to the equation is the average of the effluent concentration between time point 1 and 2. The change in concentration of methane for the accumulation term is also found by the difference between concentrations of time points 1 and 2 (t_1 and t_2). Dissolved methane is considered negligible and not considered for this study. Total gas consumed would be in units of mmol. Oxygen balance follows the same format of the equations above for methane.

Carbon dioxide balance

$$F_{out} * y_{CO_{2out}} * (t_2 - t_1) + V_{Headspace} * \Delta C_{CO2} + V_{Liquid} * \Delta\, C_{IC} + F_L * C_{IC} * (t_2 - t_1) = CO_2 Produced$$

The flow rate (F_L) for liquid phase is the same for medium inlet and outlet as the volume in the reactor was maintained at the same level throughout the study. The change in concentration of inorganic carbon (IC) is measured as covered in Chapter 3. For outflow, the mole fraction of the gaseous CO_2 and the concentration of IC in the liquid flow is averaged between measured values over time points 1 and 2. The total carbon dioxide produced would be in units of mmol.

Total liquid carbon balance

$$V_{Liquid} * \Delta\, C_{TC} + F_L * C_{TC} * (t_2 - t_1) - F_L * C_{anti} * (t_2 - t_1) = TC\ Produced$$

The total liquid carbon balance is constructed by the measured total carbon and except for accounts for the carbon in the antifoam introduced over the same time points. For outflow, the concentration of TC in the liquid flow is averaged between measured values over time points 1 and 2. As before, the units of total carbon are in mmol. Total organic carbon (OC) production is simply the difference between liquid TC and IC.

Biomass

$$\left(\Delta X * V_{Liquid} + X * F_L * (t_2 - t_1)\right) * 39.3 \frac{mmol\ C}{g\ DCW} = Carbon\ in\ Biomass$$

Biomass is represented by X and is in units of gDCW L^{-1}. For outflow, the concentration of biomass in the liquid flow is averaged between measured values over time points 1 and 2. The amount of carbon associated with biomass is found from the biomass equation in de la Torre et. al. [106].

Complete carbon balance

$$Carbon\ Prod. = \ Carbon\ in\ Biomass + \ TC\ Produced + F_{out} * y_{CO_{2out}} * (t_2 - t_1) + V_{Headspace} * \Delta C_{CO2}$$

The total carbon produced is from biomass, total liquid carbon, and carbon dioxide in the headspace.

$$\frac{Carbon\ Produced}{Carbon\ Consumed} * 100\% = \%\ of\ carbon\ accounted\ for$$

Specific gas pickup and production rates (methane used as example)

$$\frac{CH_4 consumed}{X_2 * V_L * (t_2 - t_1)} = Specific\ methane\ pickup\ (mmol\ gDCW^{-1}\ h^{-1})$$

Where the cell concentration at the time of measurement (2 in this example) is used. This equation shows that only the cells behavior in the reactor is considered. At steady state there is minimal variation in cell concentration so the specific pickup rate should remain relative constant, as demonstrated in results of Chapter 5.

Appendix C: Development of Summarized Hybrid Respiration with Denitrification

Both routes will consider nitrate reductase (NAR), nitrite reductase (NIR), and nitric oxide reductase (NOR). It should be noted that only nitrate reductase is NAR is considered which allows for two hydrogen per nitrate to be pumped across the membrane. Another form does exist (NAP) but does not generate protons that could be useful for ATP production. What differentiates the two routes built here is the use of nitrous oxide reductase (NOS) or nitric oxide dismutase (NOD).

The following reactions are in line with these enzymes:

NAR

$$2NO_3^- + \ 8H_c^+ + 4\,e^- \rightarrow 2NO_2^- + 2H_2O + 4H_p^+$$

NIR

$$2NO_2^- + \ 4H_p^+ + 2\,e^- \rightarrow 2NO + 2H_2O$$

NOR

$$2NO + 2\,H_p^+ + 2e^- \rightarrow N_2O + \ H_2O$$

NOS

$$N_2O + \ 2H_p^+ + 2\,e^- \rightarrow N_2 + H_2O$$

NOD

$$N_2O \rightarrow N_2 + 0.5\,O_2$$

Summarizing equations above

NAR-> NOS

$$2NO_3 + 8H_c^+ + 4H_p^+ + 10e^- \rightarrow N_2 + 6H_2O$$

NAR-> NOD

$$2NO_3 + 8H_c^+ + 2H_p^+ + 8e^- \rightarrow N_2 + 5H_2O + 0.5O_2$$

Assuming that complex I, complex III, and ATP synthase are still active from typical aerobic respiration and electrons are efficiently transported for denitrification, the following portion of typical aerobic respiration is considered:

$$NADH + 8H_c^+ + xADP + xP_i \rightarrow NAD^+ + 8H_p^- + x\ ATP$$

Where the fraction of ADP, P_i, and ATP are dependent on the total amount of hydrogens that would be pumped back across the membrane to the cytoplasm from ATP synthase. Combining the partial aerobic respiration to the summarized nitrification equations and assuming 3.3 H^+ per ATP produced, the following equations were implemented into the model:

NAR->NOS-> ATP

$$2NO_3 + 48H_c^+ + 5NADH + 10.9\ ADP + 10.9\ P_i \rightarrow N_2 + 6H_2O + 36\ H_c^+ + 10.9\ ATP$$

NAR->NOD-> ATP

$$2NO_3 + 40H_c^+ + 4NADH + 9.1\ ADP + 9.1\ P_i \rightarrow N_2 + 0.5O_2 + 5H_2O + 30\ H_c^+ + 9.1\ ATP$$

Note that H_c^+ is on both sides of the equation. This is to show the hydrogens pumped across the membrane from electron transport chain and back via ATP synthase. There are less hydrogens pumped back to the cytoplasm because of the hydrogens consumed for denitrification. For the later equation of NAR-> NOD-> ATP, the total ATP production with the aerobic oxidation of the half molecule of oxygen would provide the following equation (not used in the model):

$$2NO_3 + 50\ H_c^+ + 5\ NADH + 12.1\ ADP + 12.1\ P_i \rightarrow\ N_2 + 6H_2O + 40\ H_c^+ + 12.1\ ATP$$

This shows that with the same reducing power, the cells with NOD are able to make significantly more ATP compared to those with NOS, as long as reducing power is available.

By summarizing the above equations and I presume 1) That nitrification exists with these known enzymes. No current literature supports that such enzymes are expressed with 5GB1 at this current time. 2) The electrons and hydrogen ions pumped are not negatively affected by any inefficiencies or leakage. Meaning that once NADH transfers electrons to NADH dehydrogenase there are mechanisms for cells to continue the electron flow to denitrification enzymes without a problem and hydrogens are pumped in the same amounts as theoretically expected. 3) The complex I, complex III, and ATP synthase are still active and remain efficient throughout hybrid respiration.

Appendix D: Summary of Soft Sensor Development

The following appendix is a brief summary of the published work “A novel soft sensor approach for estimating individual biomass in mixed cultures” that excludes details regarding methodology and comparison to cell counting techniques [137].

Figure B1 illustrates the unique absorbance spectrum of different organisms suspended in DI water over a range of wavelengths. This occurs because of the different cellular compositions and structures such as intracellular membranes or organelles. Upon mixing these organisms at different concentrations, unique OD scanning spectra over a range of wavelengths would be obtained. This mixed behavior leaves a sort of unique fingerprint that allows for the complete determination of the individual cell concentrations in the mixed culture.

Figure B1

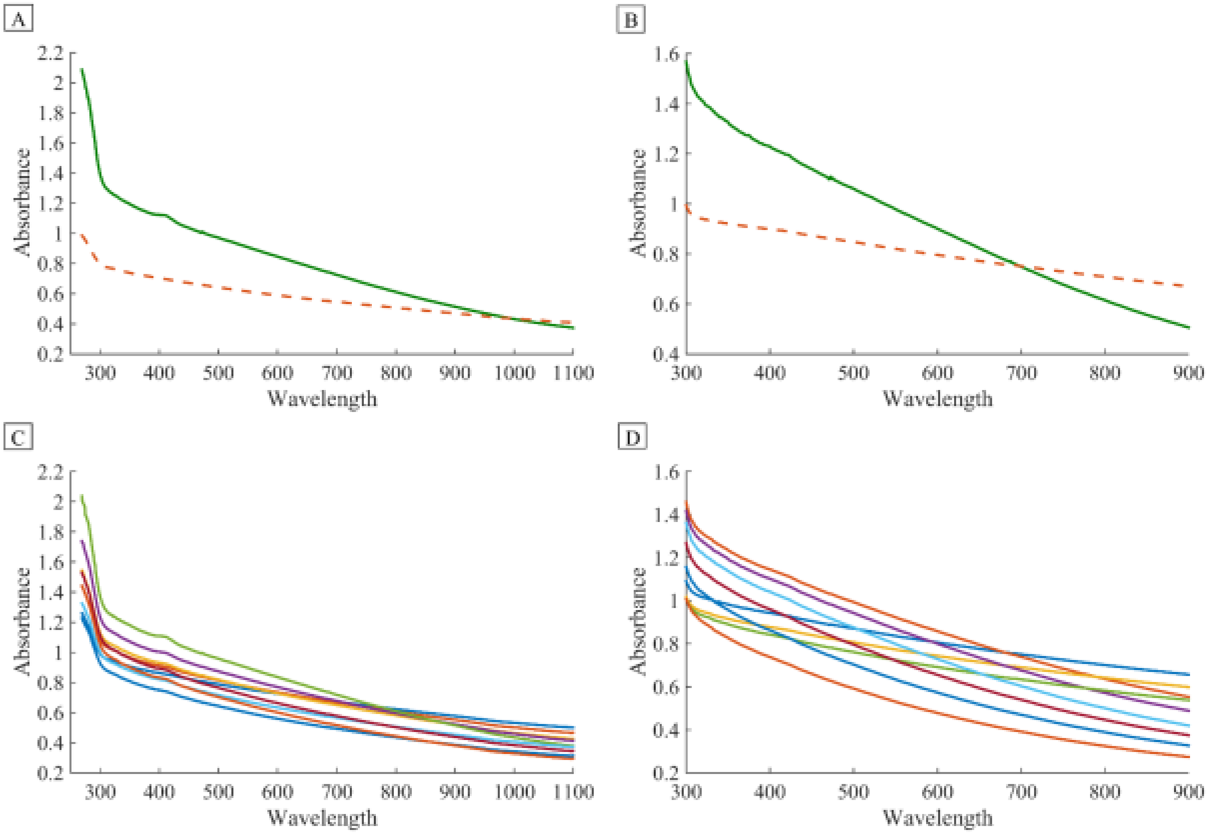

(a) OD spectra of pure *M. buryatense* (solid line) and *S. stipitis* (dashed line) over the wavelength of 269–1100 nm. (b) OD spectra of pure *E. coli* (solid line) and *S. cerevisiae* (dashed line) over the wavelength of 300–900 nm. (c) OD spectra of nine different mixed cultures of *M. buryatense* and *S. stipitis* over the wavelength of 269–1100 nm. (d) OD spectra of nine different mixed cultures of *E. coli* and *S. cerevisiae* over the wavelength of 300–900 nm.

In this study, partial least squares (PLS) is used to build the soft sensor model that correlates the mixture sample's OD scanning spectrum to individual cell concentration. Two case studies (Cases 1 and 2) were conducted to examine the performance of the proposed soft sensor approach. Case 1 uses *M. buryatense* and *S. stipites,* while Case 2 uses *E. coli* KO11 and *S. cerevisiae*.

After building the model and evaluating the performance with 100 Monte Carlo simulations a PLS soft sensor model was built to correlate the OD spectra with each individual cell concentration (i.e., two models were built for Case 1 and Case 2, respectively). The number of principal components was selected based on cross validation. For Case 1, four PCs were chosen for predicting *M. buryatense* concentration, while three PCs were chosen for predicting *S. stipitis*. For Case 2, four PCs were chosen for predicting both *E. coli* and *S. cerevisiae*. For Case 1, the average percentage errors for the 100 testing sets were 1.69% for *M. buryatense* and 3.97% for *S. stipitis*. For Case 2, the average percentage errors for the 100 testing sets were 3.23 and 1.92% for *E. coli* and *S. cerevisiae*, respectively. The results are summarized in Figure B2.

Figure B2

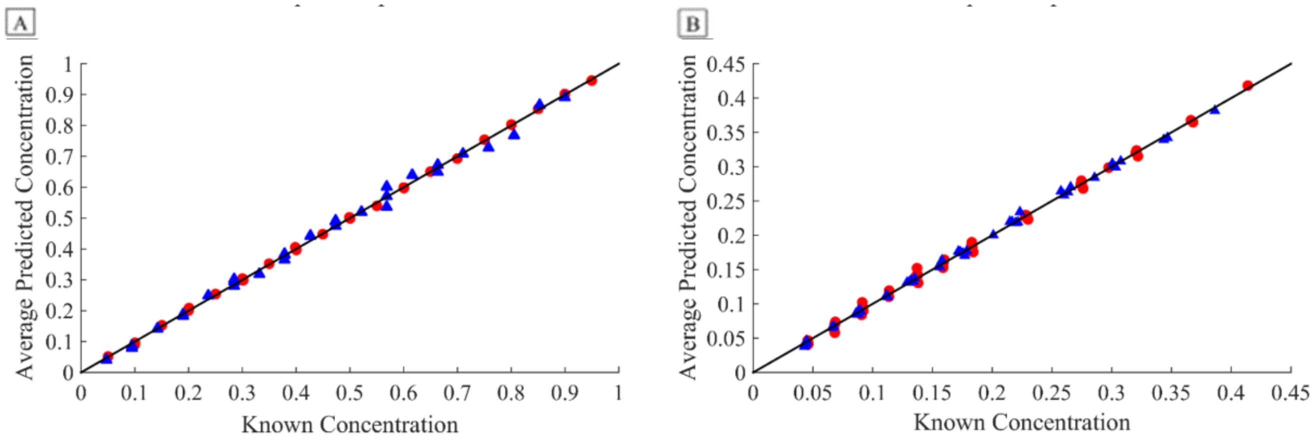

The diagonal line represents the case where predicted and known concentrations are the same. (A) Comparison of soft sensor prediction and know concentrations for Case 1. The filled dots (●) represent *M. buryatense* and the filled triangles (▲) represent *S. stipitis*. (B) Comparison of soft sensor predictions and known concentrations for Case 2. The filled dots (●) represent *E. coli* and the filled triangles (▲) represent *S. cerevisiae*.

References

[1] US EIA, Frequently Asked Questions-Natural Gas, (n.d.). https://www.eia.gov/tools/faqs/faq.php?id=58&t=8 (accessed May 1, 2017).

[2] US EIA, Natural Gas- U.S. Dry Natural Gas Production, (n.d.). https://www.eia.gov/dnav/ng/hist/n9070us2A.htm (accessed May 1, 2017).

[3] USDSA, USEPA, USDOE, Biogas Opportunities Roadmap, (2014).

[4] Environmental Protection Agency/USA, Overview of Greenhouse Gases, (2017). https://www.epa.gov/ghgemissions/overview-greenhouse-gases#methane (accessed May 1, 2017).

[5] E.I.A. USA, Natural Gas Gross Withdrawlas and Production, (n.d.) Vented and Flared. https://www.eia.gov/dnav/ng/ng_prod_sum_a_EPG0_VGV_mmcf_a.htm (accessed May 1, 2017).

[6] J.M. Estrada, R. Lebrero, G. Quijano, R. Pérez, I. Figueroa-González, P.A. García-Encina, R. Muñoz, Methane abatement in a gas-recycling biotrickling filter: Evaluating innovative operational strategies to overcome mass transfer limitations, Chem. Eng. J. 253 (2014) 385–393. doi:10.1016/j.cej.2014.05.053.

[7] A.J. Pieja, M.C. Morse, A.J. Cal, Methane to bioproducts: the future of the bioeconomy?, Curr. Opin. Chem. Biol. 41 (2017) 123–131. doi:10.1016/j.cbpa.2017.10.024.

[8] Y. Trotsenko, J.C. Murrell, Metabolic aspects of aerobic obligate methanotrophy., Adv. Appl. Microbiol. 63 (2008) 183–229. doi:10.1016/S0065-2164(07)00005-6.

[9] H. Dalton, The Leeuwenhoek Lecture 2000 the natural and unnatural history of methane-oxidizing bacteria., Philos. Trans. R. Soc. Lond. B. Biol. Sci. 360 (2005) 1207–22. doi:10.1098/rstb.2005.1657.

[10] R.S. Hanson, T.E. Hanson, Methanotrophic bacteria., Microbiol. Rev. 60 (1996) 439–71. http://www.pubmedcentral.nih.gov/articlerender.fcgi?artid=239451&tool=pmcentrez&rendertype=abstract.

[11] J.D. Semrau, A. a DiSpirito, S. Yoon, Methanotrophs and copper., FEMS Microbiol. Rev. 34 (2010) 496–531. doi:10.1111/j.1574-6976.2010.00212.x.

[12] L. Chistoserdova, M.G. Kalyuzhnaya, M.E. Lidstrom, The expanding world of methylotrophic metabolism., Annu. Rev. Microbiol. 63 (2009) 477–99. doi:10.1146/annurev.micro.091208.073600.

[13] R. Whittenbury, K.C. Phillips, J.F. Wilkinson, Enrichment, isolation and some properties of methane-utilizing bacteria., J. Gen. Microbiol. 61 (1970) 205–18. http://www.ncbi.nlm.nih.gov/pubmed/5476891.

[14] Q. Fei, M.T. Guarnieri, L. Tao, L.M.L. Laurens, N. Dowe, P.T. Pienkos, Bioconversion of natural gas to liquid fuel: opportunities and challenges., Biotechnol. Adv. 32 (2014) 596–614. doi:10.1016/j.biotechadv.2014.03.011.

[15] D. Park, J. Lee, Biological conversion of methane to methanol, Korean J. Chem. Eng. 30 (2013) 977–987. doi:10.1007/s11814-013-0060-5.

[16] T. Smith, H. Dalton, Biocatalysis by methane monooxygenase and its implications for the petroleum industry, Stud. Surf. Sci. Catal. (2004) 177–192. http://www.sciencedirect.com/science/article/pii/S0167299104801472/pdf?md5=bbbb457

c87ecafbeec262705c0b183c0&pid=1-s2.0-S0167299104801472-main.pdf&_valck=1 (accessed July 13, 2014).

[17] A.S. Hakemian, A.C. Rosenzweig, The biochemistry of methane oxidation., Annu. Rev. Biochem. 76 (2007) 223–41. doi:10.1146/annurev.biochem.76.061505.175355.

[18] G.E. Kenney, A.C. Rosenzweig, Chemistry and biology of the copper chelator methanobactin., ACS Chem. Biol. 7 (2012) 260–8. doi:10.1021/cb2003913.

[19] K. Chidambarampadmavathy, K. Obulisamy P., K. Heimann, Role of copper and iron in methane oxidation and bacterial biopolymer accumulation, Eng. Life Sci. 15 (2015) 387–399. doi:10.1002/elsc.201400127.

[20] M.G. Kalyuzhnaya, A.W. Puri, M.E. Lidstrom, Metabolic engineering in methanotrophic bacteria, Metab. Eng. 29 (2015) 142–152. doi:10.1016/j.ymben.2015.03.010.

[21] J.D. Semrau, Bioremediation via Methanotrophy: Overview of Recent Findings and Suggestions for Future Research., Front. Microbiol. 2 (2011) 209. doi:10.3389/fmicb.2011.00209.

[22] H. Jiang, Y. Chen, P. Jiang, C. Zhang, T.J. Smith, J.C. Murrell, X.-H. Xing, Methanotrophs: Multifunctional bacteria with promising applications in environmental bioengineering, Biochem. Eng. J. 49 (2010) 277–288. doi:10.1016/j.bej.2010.01.003.

[23] P.J. Strong, S. Xie, W.P. Clarke, Methane as a Resource: Can the Methanotrophs Add Value?, Environ. Sci. Technol. 49 (2015) 4001–4018. doi:10.1021/es504242n.

[24] P.J. Strong, M. Kalyuzhnaya, J. Silverman, W.P. Clarke, A methanotroph-based biorefinery: Potential scenarios for generating multiple products from a single fermentation, Bioresour. Technol. 215 (2016) 314–323. doi:10.1016/j.biortech.2016.04.099.

[25] O.P. Karthikeyan, K. Chidambarampadmavathy, S. Cirés, K. Heimann, Review of Sustainable Methane Mitigation and Biopolymer Production, Crit. Rev. Environ. Sci. Technol. 45 (2014) 1579–1610. doi:10.1080/10643389.2014.966422.

[26] Y. a. Trotsenko, N. V. Doronina, V.N. Khmelenina, Biotechnological Potential of Aerobic Methylotrophic Bacteria: A Review of Current State and Future Prospects, Appl. Biochem. Microbiol. 41 (2005) 433–441. doi:10.1007/s10438-005-0078-5.

[27] X. Ge, L. Yang, J.P. Sheets, Z. Yu, Y. Li, Biological conversion of methane to liquid fuels: Status and opportunities., Biotechnol. Adv. 32 (2014) 1460–1475. doi:10.1016/j.biotechadv.2014.09.004.

[28] M. Ladisch, E. Ximenes, A. Engelberth, N. Mosier, Biological Engineering and the Emerging Cellulose Ethanol Industry, Chem. Eng. Prog. 110 (2014) 59–62.

[29] T. Dong, Q. Fei, M. Genelot, H. Smith, L.M.L. Laurens, M.J. Watson, P.T. Pienkos, A novel integrated biorefinery process for diesel fuel blendstock production using lipids from the methanotroph, Methylomicrobium buryatense, Energy Convers. Manag. 140 (2017) 62–70. doi:10.1016/j.enconman.2017.02.075.

[30] A. Hakemian, K. Kondapalli, J. Telser, B. Hoffman, T. Stemmler, A. Rosenzweig, The Metal Centers of Particulate Methane Monooxygenase from Methylosinus trichosporium OB3b†‡, Biochemistry. (2008) 6793–6801. http://pubs.acs.org/doi/abs/10.1021/bi800598h (accessed July 31, 2013).

[31] T.J. Lawton, A.C. Rosenzweig, Methane-Oxidizing Enzymes: An Upstream Problem in Biological Gas-to-Liquids Conversion, J. Am. Chem. Soc. 138 (2016) 9327–9340. doi:10.1021/jacs.6b04568.

[32] A. Gilman, Development of a Promising Methanotrophic Bacterium as an Industrial

Biocatalyst, University of Washington, 2017. http://hdl.handle.net/1773/39973.

[33] A.A. DiSpirito, J.D. Semrau, J.C. Murrell, W.H. Gallagher, C. Dennison, S. Vuilleumier, Methanobactin and the Link between Copper and Bacterial Methane Oxidation, Microbiol. Mol. Biol. Rev. 80 (2016) 387–409. doi:10.1128/MMBR.00058-15.

[34] C.W. Knapp, D.A. Fowle, E. Kulczycki, J.A. Roberts, D.W. Graham, Methane monooxygenase gene expression mediated by methanobactin in the presence of mineral copper sources, Proc. Natl. Acad. Sci. 104 (2007) 12040–12045. doi:10.1073/pnas.0702879104.

[35] J.D. Semrau, S. Jagadevan, A.A. DiSpirito, A. Khalifa, J. Scanlan, B.H. Bergman, B.C. Freemeier, B.S. Baral, N.L. Bandow, A. Vorobev, D.H. Haft, S. Vuilleumier, J.C. Murrell, Methanobactin and MmoD work in concert to act as the “copper-switch” in methanotrophs, Environ. Microbiol. (2013) n/a-n/a. doi:10.1111/1462-2920.12150.

[36] A. Gilman, L.M. Laurens, A.W. Puri, F. Chu, P.T. Pienkos, M.E. Lidstrom, Bioreactor performance parameters for an industrially-promising methanotroph Methylomicrobium buryatense 5GB1, Microb. Cell Fact. 14 (2015) 182. doi:10.1186/s12934-015-0372-8.

[37] J. Silverman, Single Cell Protein: A sustainable approach to meeting the growing protein demand, Aquafeed. 7 (2015) 10–14.

[38] A. Demidenko, I.R. Akberdin, M. Allemann, E.E. Allen, M.G. Kalyuzhnaya, Fatty Acid Biosynthesis Pathways in Methylomicrobium buryatense 5G(B1), Front. Microbiol. 7 (2017). doi:10.3389/fmicb.2016.02167.

[39] C. Duan, M. Luo, X. Xing, High-rate conversion of methane to methanol by Methylosinus trichosporium OB3b., Bioresour. Technol. 102 (2011) 7349–53. doi:10.1016/j.biortech.2011.04.096.

[40] P. Mehta, S. Mishra, T. Ghose, Methanol accumulation by resting cells of Methylosinus trichosporium, J. Gen. Appl. …. 229 (1987) 221–229. http://cat.inist.fr/?aModele=afficheN&cpsidt=8376696 (accessed March 23, 2014).

[41] J.-S. Han, C.-M. Ahn, B. Mahanty, C.-G. Kim, Partial oxidative conversion of methane to methanol through selective inhibition of methanol dehydrogenase in methanotrophic consortium from landfill cover soil., Appl. Biochem. Biotechnol. 171 (2013) 1487–99. doi:10.1007/s12010-013-0410-0.

[42] H.G. Kim, G.H. Han, S.W. Kim, Optimization of lab scale methanol production by Methylosinus trichosporium OB3b, Biotechnol. Bioprocess Eng. 15 (2010) 476–480. doi:10.1007/s12257-010-0039-6.

[43] S.G. Lee, J.H. Goo, H.G. Kim, J.-I. Oh, Y.M. Kim, S.W. Kim, Optimization of methanol biosynthesis from methane using Methylosinus trichosporium OB3b., Biotechnol. Lett. 26 (2004) 947–50. http://www.ncbi.nlm.nih.gov/pubmed/15269546.

[44] M. Takeguchi, T. Furuto, D. Sugimori, I. Okura, Optimization of methanol biosynthesis byMethylosinus trichosporium OB3b: An approach to improve methanol accumulation, Appl. Biochem. Biotechnol. 68 (1997). http://link.springer.com/article/10.1007/BF02785987 (accessed September 14, 2014).

[45] T. Furuto, M. Takeguchi, I. Okura, Semicontinuous methanol biosynthesis by Methylosinus trichosporium OB3b, J. Mol. Catal. A Chem. (1999) 257–261. http://www.sciencedirect.com/science/article/pii/S1381116999000072 (accessed March 4, 2013).

[46] J. Xin, J. Cui, J. Niu, S. Hua, C. Xia, S. Li, L. Zhu, Production of methanol from methane by methanotrophic bacteria, Biocatal. Biotransformation. 22 (2004) 225–229.

doi:10.1080/10242420412331283305.

[47] Z. Su, X. Ge, W. Zhang, L. Wang, Z. Yu, Y. Li, Methanol Production from Biogas with a Thermotolerant Methanotrophic Consortium Isolated from an Anaerobic Digestion System, Energy & Fuels. 31 (2017) 2970–2975. doi:10.1021/acs.energyfuels.6b03471.

[48] J.P. Sheets, K. Lawson, X. Ge, L. Wang, Z. Yu, Y. Li, Development and evaluation of a trickle bed bioreactor for enhanced mass transfer and methanol production from biogas, Biochem. Eng. J. 122 (2017) 103–114. doi:10.1016/j.bej.2017.03.006.

[49] S.K.S. Patel, P. Mardina, S.-Y. Kim, J.-K. Lee, I.-W. Kim, Biological Methanol Production by a Type II Methanotroph Methylocystis bryophila, J. Microbiol. Biotechnol. 26 (2016) 717–724. doi:10.4014/jmb.1601.01013.

[50] J.A. Asenjo, J.S. Suk, Microbial Conversion of Methane into poly-β-hydroxybutyrate (PHB): Growth and intracellular product accumulation in a type II methanotroph, J. Ferment. Technol. 64 (1986) 271–278. doi:10.1016/0385-6380(86)90118-4.

[51] K. Khosravi-Darani, Z.-B. Mokhtari, T. Amai, K. Tanaka, Microbial production of poly(hydroxybutyrate) from C(1) carbon sources., Appl. Microbiol. Biotechnol. 97 (2013) 1407–24. doi:10.1007/s00253-012-4649-0.

[52] F. Rahnama, E. Vasheghani-Farahani, F. Yazdian, S.A. Shojaosadati, PHB production by Methylocystis hirsuta from natural gas in a bubble column and a vertical loop bioreactor, Biochem. Eng. J. 65 (2012) 51–56. doi:10.1016/j.bej.2012.03.014.

[53] A. Anderson, E. Dawes, Occurrence, metabolism, metabolic role, and industrial uses of bacterial polyhydroxyalkanoates., Microbiol. Rev. 54 (1990) 450–472. http://mmbr.asm.org/content/54/4/450.short (accessed December 16, 2014).

[54] D.G. Lundgren, R. Alper, C. Schnaitman, R.H. Marchessault, Different Bacteria Characterization of Poly-β3-Hydroxybutyrate Extracted from Different Bacteria, J. Bacteriol. 89 (1965) 245–251.

[55] K.-D. Wendlandt, U. Stottmeister, J. Helm, B. Soltmann, M. Jechorek, M. Beck, The potential of methane-oxidizing bacteria for applications in environmental biotechnology, Eng. Life Sci. (2010) NA-NA. doi:10.1002/elsc.200900093.

[56] K.-D. Wendlandt, W. Geyer, G. Mirschel, F. Al-Haj Hemidi, Possibilities for controlling a PHB accumulation process using various analytical methods., J. Biotechnol. 117 (2005) 119–29. doi:10.1016/j.jbiotec.2005.01.007.

[57] Y. Zhang, J. Xin, L. Chen, H. Song, C. Xia, Biosynthesis of poly-3-hydroxybutyrate with a high molecular weight by methanotroph from methane and methanol, J. Nat. Gas Chem. 17 (2008) 103–109. doi:10.1016/S1003-9953(08)60034-1.

[58] J. Helm, K.-D. Wendlandt, M. Jechorek, U. Stottmeister, Potassium deficiency results in accumulation of ultra-high molecular weight poly-beta-hydroxybutyrate in a methane-utilizing mixed culture., J. Appl. Microbiol. 105 (2008) 1054–61. doi:10.1111/j.1365-2672.2008.03831.x.

[59] N.N. Shah, M.L. Hanna, R.T. Taylor, Batch cultivation of Methylosinus trichosporium OB3b: V. Characterization of poly-beta-hydroxybutyrate production under methane-dependent growth conditions., Biotechnol. Bioeng. 49 (1996) 161–71. doi:10.1002/(SICI)1097-0290(19960120)49:2<161::AID-BIT5>3.0.CO;2-O.

[60] C. Zuñiga, M. Morales, S. Revah, Polyhydroxyalkanoates accumulation by Methylobacterium organophilum CZ-2 during methane degradation using citrate or propionate as cosubstrates., Bioresour. Technol. 129 (2013) 686–9. doi:10.1016/j.biortech.2012.11.120.

[61] M. Vecherskaya, C. Dijkema, A. Stams, Intracellular PHB conversion in a Type II methanotroph studied by 13C NMR, J. Ind. Microbiol. …. (2001) 15–21. http://link.springer.com/article/10.1038/sj.jim.7000086 (accessed December 15, 2014).

[62] K. Wendlandt, M. Jechorek, Producing poly-3-hydroxybutyrate with a high molecular mass from methane, J. Biotechnol. 86 (2001) 127–133. http://www.sciencedirect.com/science/article/pii/S0168165600004089 (accessed December 4, 2014).

[63] K. Chidambarampadmavathy, O.P. Karthikeyan, K. Heimann, Biopolymers made from methane in bioreactors, Eng. Life Sci. 15 (2015) 689–699. doi:10.1002/elsc.201400203.

[64] A.J. Cal, W.D. Sikkema, M.I. Ponce, D. Franqui-Villanueva, T.J. Riiff, W.J. Orts, A.J. Pieja, C.C. Lee, Methanotrophic production of polyhydroxybutyrate- co -hydroxyvalerate with high hydroxyvalerate content, Int. J. Biol. Macromol. 87 (2016) 302–307. doi:10.1016/j.ijbiomac.2016.02.056.

[65] T. García-Pérez, J.C. López, F. Passos, R. Lebrero, S. Revah, R. Muñoz, Simultaneous methane abatement and PHB production by Methylocystis hirsuta in a novel gas-recycling bubble column bioreactor, Chem. Eng. J. 334 (2018) 691–697. doi:10.1016/j.cej.2017.10.106.

[66] M.G. Kalyuzhnaya, S. Yang, O.N. Rozova, N.E. Smalley, J. Clubb, A. Lamb, G.A.N. Gowda, D. Raftery, Y. Fu, F. Bringel, S. Vuilleumier, D.A.C. Beck, Y.A. Trotsenko, V.N. Khmelenina, M.E. Lidstrom, Highly efficient methane biocatalysis revealed in a methanotrophic bacterium, Nat. Commun. 4 (2013). doi:10.1038/ncomms3785.

[67] C.A. Henard, H. Smith, N. Dowe, M.G. Kalyuzhnaya, P.T. Pienkos, M.T. Guarnieri, Bioconversion of methane to lactate by an obligate methanotrophic bacterium, Sci. Rep. 6 (2016) 21585. doi:10.1038/srep21585.

[68] A.S. Reshetnikov, V.N. Khmelenina, I.I. Mustakhimov, M. Kalyuzhnaya, M. Lidstrom, Y.A. Trotsenko, Diversity and phylogeny of the ectoine biosynthesis genes in aerobic, moderately halophilic methylotrophic bacteria, Extremophiles. 15 (2011) 653–663. doi:10.1007/s00792-011-0396-x.

[69] A.S. Reshetnikov, V.N. Khmelenina, Y.A. Trotsenko, Characterization of the ectoine biosynthesis genes of haloalkalotolerant obligate methanotroph “Methylomicrobium alcaliphilum 20Z,” Arch. Microbiol. 184 (2006) 286–297. doi:10.1007/s00203-005-0042-z.

[70] S. Cantera, R. Lebrero, S. Rodríguez, P.A. García-Encina, R. Muñoz, Ectoine bio-milking in methanotrophs: A step further towards methane-based bio-refineries into high added-value products, Chem. Eng. J. 328 (2017) 44–48. doi:10.1016/j.cej.2017.07.027.

[71] S. Cantera, R. Lebrero, E. Rodríguez, P.A. García-Encina, R. Muñoz, Continuous abatement of methane coupled with ectoine production by Methylomicrobium alcaliphilum 20Z in stirred tank reactors: A step further towards greenhouse gas biorefineries, J. Clean. Prod. 152 (2017) 134–141. doi:10.1016/j.jclepro.2017.03.123.

[72] V.N. Khmelenina, V.G. Sakharovskii, A.S. Reshetnikov, Y.A. Trotsenko, Synthesis of osmoprotectants by halophilic and alkaliphilic methanotrophs, Microbiology. 69 (2000) 381–386. doi:10.1007/BF02756759.

[73] K.A. Stone, M. V. Hilliard, Q.P. He, J. Wang, A mini review on bioreactor configurations and gas transfer enhancements for biochemical methane conversion, Biochem. Eng. J. 128 (2017) 83–92. doi:10.1016/j.bej.2017.09.003.

[74] P. Strong, B. Laycock, S. Mahamud, P. Jensen, P. Lant, G. Tyson, S. Pratt, The

Opportunity for High-Performance Biomaterials from Methane, Microorganisms. 4 (2016) 11. doi:10.3390/microorganisms4010011.
[75] A.L. Damiani, M.H. Kim, J. Wang, An improved dynamic method to measure kL a in bioreactors., Biotechnol. Bioeng. 111 (2014) 2120–5. doi:10.1002/bit.25258.
[76] C. Boulart, D.P. Connelly, M.C. Mowlem, Sensors and technologies for in situ dissolved methane measurements and their evaluation using Technology Readiness Levels, TrAC Trends Anal. Chem. 29 (2010) 186–195. doi:10.1016/j.trac.2009.12.001.
[77] F. Yazdian, S.A. Alsadati, M. Nosrati, M. Abbas, K. Khosravi, On-Line Measurement of Dissolved Methane Concentration During Methane Fermentation in a Loop Bioreactor., Iran. J. Chem. Chem. Eng. 28 (2009) 85–93.
[78] C. Boulart, M.C. Mowlem, D.P. Connelly, J.-P. Dutasta, C.R. German, A novel, low-cost, high performance dissolved methane sensor for aqueous environments, Opt. Express. 16 (2008) 12607. doi:10.1364/OE.16.012607.
[79] Y. Liu, K.R. Sharma, M. Fluggen, K. O'Halloran, S. Murthy, Z. Yuan, Online dissolved methane and total dissolved sulfide measurement in sewers, Water Res. 68 (2015) 109–118. doi:10.1016/j.watres.2014.09.047.
[80] E.L. Cussler, Diffusion: Mass Transfer in Fluid Systems, 3rd ed., Cambridge University Press, New York, USA, 2009.
[81] Y. Yu, J. Ramsay, B. Ramsay, On-line estimation of dissolved methane concentration during methanotrophic fermentations, Biotechnol. …. (2006). doi:10.1002/bit.
[82] R. Lebrero, L. Hernández, R. Pérez, J.M. Estrada, R. Muñoz, Two-liquid phase partitioning biotrickling filters for methane abatement: Exploring the potential of hydrophobic methanotrophs, J. Environ. Manage. 151 (2015) 124–131. doi:10.1016/j.jenvman.2014.12.016.
[83] M. Cáceres, A.D. Dorado, J.C. Gentina, G. Aroca, Oxidation of methane in biotrickling filters inoculated with methanotrophic bacteria, Environ. Sci. Pollut. Res. 24 (2017) 25702–25712. doi:10.1007/s11356-016-7133-z.
[84] A. Avalos Ramirez, J.P. Jones, M. Heitz, Methane treatment in biotrickling filters packed with inert materials in presence of a non-ionic surfactant, J. Chem. Technol. Biotechnol. 87 (2012) 848–853. doi:10.1002/jctb.3811.
[85] P.C. Munasinghe, S.K. Khanal, Biomass-derived syngas fermentation into biofuels: Opportunities and challenges., Bioresour. Technol. 101 (2010) 5013–22. doi:10.1016/j.biortech.2009.12.098.
[86] E. Dumont, H. Delmas, Mass transfer enhancement of gas absorption in oil-in-water systems: a review, Chem. Eng. Process. Process Intensif. 42 (2003) 419–438. doi:10.1016/S0255-2701(02)00067-3.
[87] A.-I. Galaction, D. Cascaval, C. Oniscu, M. Turnea, Enhancement of oxygen mass transfer in stirred bioreactors using oxygen-vectors. 1. Simulated fermentation broths, Bioprocess Biosyst. Eng. 26 (2004). doi:10.1007/s00449-004-0353-5.
[88] G. Quijano, M. Hernandez, S. Villaverde, F. Thalasso, R. Muñoz, A step-forward in the characterization and potential applications of solid and liquid oxygen transfer vectors, Appl. Microbiol. Biotechnol. 85 (2010) 543–551. doi:10.1007/s00253-009-2146-x.
[89] K.G. Clarke, L.D.C. Correia, Oxygen transfer in hydrocarbon–aqueous dispersions and its applicability to alkane bioprocesses: A review, Biochem. Eng. J. 39 (2008) 405–429. doi:10.1016/j.bej.2007.11.020.
[90] J. Rocha-Rios, G. Quijano, F. Thalasso, S. Revah, R. Muñoz, Methane biodegradation in a

two-phase partition internal loop airlift reactor with gas recirculation, J. Chem. Technol. Biotechnol. 86 (2011) 353–360. doi:10.1002/jctb.2523.

[91] C. Kennelly, S. Gerrity, G. Collins, E. Clifford, Liquid phase optimisation in a horizontal flow biofilm reactor (HFBR) technology for the removal of methane at low temperatures, Chem. Eng. J. 242 (2014) 144–154. doi:10.1016/j.cej.2013.12.071.

[92] A.J. Daugulis, N.G. Boudreau, Solid-liquid two-phase partitioning bioreactors for the treatment of gas-phase volatile organic carbons (VOCs) by a microbial consortium, Biotechnol. Lett. 30 (2008) 1583–1587. doi:10.1007/s10529-008-9721-6.

[93] B.G. Amsden, J. Bochanysz, A.J. Daugulis, Degradation of xenobiotics in a partitioning bioreactor in which the partitioning phase is a polymer, Biotechnol. Bioeng. 84 (2003) 399–405. doi:10.1002/bit.10804.

[94] G. Quijano, J. Rocha-Ríos, M. Hernández, S. Villaverde, S. Revah, R. Muñoz, F. Thalasso, Determining the effect of solid and liquid vectors on the gaseous interfacial area and oxygen transfer rates in two-phase partitioning bioreactors, J. Hazard. Mater. 175 (2010) 1085–1089. doi:10.1016/j.jhazmat.2009.10.020.

[95] K.. Ruthiya, J. van der Schaaf, B.F.. Kuster, J.. Schouten, Mechanisms of physical and reaction enhancement of mass transfer in a gas inducing stirred slurry reactor, Chem. Eng. J. 96 (2003) 55–69. doi:10.1016/j.cej.2003.08.005.

[96] J. V. Littlejohns, A.J. Daugulis, Oxygen transfer in a gas–liquid system containing solids of varying oxygen affinity, Chem. Eng. J. 129 (2007) 67–74. doi:10.1016/j.cej.2006.11.002.

[97] E.B. Larsen, U-shape and/or nozzle U-loop fermentor and method of carrying out a fermentation process, US6492135 B1, 2002.

[98] Q. Fei, Benefits and hurdles for biological methane upgrading, in: Sustain. Chem. Plast. Adopt. Appl. Summit Methane Bioeng. Summit, 2015.

[99] B.Ø. Palsson, Systems Biology: Properties of Reconstructed Networks, 1st ed., Cambridge University Press, 2006.

[100] R. Agren, L. Liu, S. Shoaie, W. Vongsangnak, I. Nookaew, J. Nielsen, The RAVEN Toolbox and Its Use for Generating a Genome-scale Metabolic Model for Penicillium chrysogenum, PLoS Comput. Biol. 9 (2013) e1002980. doi:10.1371/journal.pcbi.1002980.

[101] J. Schellenberger, R. Que, R.M.T. Fleming, I. Thiele, J.D. Orth, A.M. Feist, D.C. Zielinski, A. Bordbar, N.E. Lewis, S. Rahmanian, J. Kang, D.R. Hyduke, B.Ø. Palsson, Quantitative prediction of cellular metabolism with constraint-based models: the COBRA Toolbox v2.0, Nat. Protoc. 6 (2011) 1290–1307. doi:10.1038/nprot.2011.308.

[102] J.D. Orth, I. Thiele, B.Ø. Palsson, What is flux balance analysis?, Nat. Biotechnol. 28 (2010) 245–248. doi:10.1038/nbt.1614.

[103] R. Ramakrishna, J.S. Edwards, A. McCulloch, B.O. Palsson, Flux-balance analysis of mitochondrial energy metabolism: consequences of systemic stoichiometric constraints, Am. J. Physiol. Integr. Comp. Physiol. 280 (2001) R695–R704. doi:10.1152/ajpregu.2001.280.3.R695.

[104] A. Damiani, Control Engineering Perspective on Genome-Scale Metabolic Modeling, Auburn University, 2015.

[105] A. Damiani, Q.P. He, J. Wang, A System Identification Based Framework for Genome-Scale Metabolic Model Validation and Refinement, IFAC-PapersOnLine. 50 (2017) 12502–12507. doi:10.1016/j.ifacol.2017.08.2058.

[106] A. de la Torre, A. Metivier, F. Chu, L.M.L. Laurens, D.A.C. Beck, P.T. Pienkos, M.E.

Lidstrom, M.G. Kalyuzhnaya, Genome-scale metabolic reconstructions and theoretical investigation of methane conversion in Methylomicrobium buryatense strain 5G(B1), Microb. Cell Fact. 14 (2015) 188. doi:10.1186/s12934-015-0377-3.

[107] A. Gilman, Y. Fu, M. Hendershott, F. Chu, A.W. Puri, A.L. Smith, M. Pesesky, R. Lieberman, D.A.C. Beck, M.E. Lidstrom, Oxygen-limited metabolism in the methanotroph Methylomicrobium buryatense 5GB1C, PeerJ. 5 (2017) e3945. doi:10.7717/peerj.3945.

[108] I.R. Akberdin, M. Thompson, R. Hamilton, N. Desai, D. Alexander, C.A. Henard, M.T. Guarnieri, M.G. Kalyuzhnaya, Methane utilization in Methylomicrobium alcaliphilum 20ZR: a systems approach, Sci. Rep. 8 (2018) 2512. doi:10.1038/s41598-018-20574-z.

[109] M. Kaluzhnaya, V. Khmelenina, B. Eshinimaev, N. Suzina, D. Nikitin, A. Solonin, J.-L. Lin, I. McDonald, C. Murrell, Y. Trotsenko, Taxonomic Characterization of New Alkaliphilic and Alkalitolerant Methanotrophs from Soda Lakes of the Southeastern Transbaikal Region and description of Methylomicrobium buryatense sp.nov., Syst. Appl. Microbiol. 24 (2001) 166–176. doi:10.1078/0723-2020-00028.

[110] A.W. Puri, S. Owen, F. Chu, T. Chavkin, D.A.C. Beck, M.G. Kalyuzhnaya, M.E. Lidstrom, Genetic Tools for the Industrially Promising Methanotroph Methylomicrobium buryatense, Appl. Environ. Microbiol. 81 (2015) 1775–1781. doi:10.1128/AEM.03795-14.

[111] X. Yan, F. Chu, A.W. Puri, Y. Fu, M.E. Lidstrom, Electroporation-Based Genetic Manipulation in Type I Methanotrophs, Appl. Environ. Microbiol. 82 (2016) 2062–2069. doi:10.1128/AEM.03724-15.

[112] C.A. Henard, H.K. Smith, M.T. Guarnieri, Phosphoketolase overexpression increases biomass and lipid yield from methane in an obligate methanotrophic biocatalyst, Metab. Eng. 41 (2017) 152–158. doi:10.1016/j.ymben.2017.03.007.

[113] J. Butler, Carbon Dioxide Equilibria and Their Applications, CRC Press, 1991.

[114] W. Burne, 5. Aqueous phase chemistry, (n.d.). https://www.ems.psu.edu/~brune/m532/m532_ch5_aqueous_phase.htm.

[115] R. Sander, Compilation of Henry’s law constants (version 4.0) for water as solvent, Atmos. Chem. Phys. 15 (2015) 4399–4981. doi:10.5194/acp-15-4399-2015.

[116] C.-B. Leng, J.E. Roberts, G. Zeng, Y.-H. Zhang, Y. Liu, Effects of temperature, pH, and ionic strength on the Henry’s law constant of triethylamine, Geophys. Res. Lett. 42 (2015) 3569–3575. doi:10.1002/2015GL063840.

[117] Y. MORINAGA, S. YAMANAKA, M. YOSHIMURA, K. TAKINAMI, Y. HIROSE, Methane metabolism of the obligate methane-utilizing bacterium, Methylomonas flagellata, in methane-limited and oxygen-limited chemostat culture., Agric. Biol. Chem. 43 (1979) 2453–2458. doi:10.1271/bbb1961.43.2453.

[118] R.J. Conrado, R. Gonzalez, Envisioning the Bioconversion of Methane to Liquid Fuels, Science (80-.). 343 (2014) 621–623. doi:10.1126/science.1246929.

[119] J.H. Wilshusen, J.P.A. Hettiaratchi, A. De Visscher, R. Saint-Fort, Methane oxidation and formation of EPS in compost: effect of oxygen concentration, Environ. Pollut. 129 (2004) 305–314. doi:10.1016/j.envpol.2003.10.015.

[120] W. Chiemchaisri, J.S. Wu, C. Visvanathan, Methanotrophic production of extracellular polysaccharide in landfill cover soils, Water Sci. Technol. 43 (2001) 151 LP-159. http://wst.iwaponline.com/content/43/6/151.abstract.

[121] I.Y. Oshkin, D.A. Beck, A.E. Lamb, V. Tchesnokova, G. Benuska, T.L. McTaggart, M.G.

Kalyuzhnaya, S.N. Dedysh, M.E. Lidstrom, L. Chistoserdova, Methane-fed microbial microcosms show differential community dynamics and pinpoint taxa involved in communal response, ISME J. 9 (2015) 1119–1129. doi:10.1038/ismej.2014.203.

[122] X.-M. Wei, R. He, M. Chen, Y. Su, R.-C. Ma, Conversion of methane-derived carbon and microbial community in enrichment cultures in response to O2 availability, Environ. Sci. Pollut. Res. 23 (2016) 7517–7528. doi:10.1007/s11356-015-6017-y.

[123] X.-M. Wei, Y. Su, H.-T. Zhang, M. Chen, R. He, Responses of methanotrophic activity, community and EPS production to CH4 and O2 concentrations in waste biocover soils, Waste Manag. 42 (2015) 118–127. doi:10.1016/j.wasman.2015.04.005.

[124] L. Chistoserdova, Methylotrophs in natural habitats: current insights through metagenomics, Appl. Microbiol. Biotechnol. 99 (2015) 5763–5779. doi:10.1007/s00253-015-6713-z.

[125] N. Schill, W.M. van Gulik, D. Voisard, U. von Stockar, Continuous cultures limited by a gaseous substrate: Development of a simple, unstructured mathematical model and experimental verification with Methanobacterium thermoautotrophicum, Biotechnol. Bioeng. 51 (2000) 645–658. doi:10.1002/(SICI)1097-0290(19960920)51:6<645::AID-BIT4>3.0.CO;2-H.

[126] M. Liang, M.H. Kim, Q.P. He, J. Wang, Impact of pseudo-continuous fermentation on the ethanol tolerance of Scheffersomyces stipitis, J. Biosci. Bioeng. 116 (2013) 319–326. doi:10.1016/j.jbiosc.2013.03.016.

[127] K.D. Kits, D.J. Campbell, A.R. Rosana, L.Y. Stein, Diverse electron sources support denitrification under hypoxia in the obligate methanotroph Methylomicrobium album strain BG8, Front. Microbiol. 6 (2015). doi:10.3389/fmicb.2015.01072.

[128] K.D. Kits, M.G. Klotz, L.Y. Stein, Methane oxidation coupled to nitrate reduction under hypoxia by the Gammaproteobacterium M ethylomonas denitrificans , sp. nov. type strain FJG1, Environ. Microbiol. 17 (2015) 3219–3232. doi:10.1111/1462-2920.12772.

[129] J. Chen, M. Strous, Denitrification and aerobic respiration, hybrid electron transport chains and co-evolution, Biochim. Biophys. Acta - Bioenerg. 1827 (2013) 136–144. doi:10.1016/j.bbabio.2012.10.002.

[130] M. Hilliard, J. Wang, Q.P. He, Elucidating the Meaning of Alternative Optimal Solutions in Flux Balance Analysis, in: AIChE Annu. Meet., 2016.

[131] A.L. Damiani, Q.P. He, T.W. Jeffries, J. Wang, Comprehensive evaluation of two genome-scale metabolic network models for Scheffersomyces stipitis, Biotechnol. Bioeng. 112 (2015) 1250–1262. doi:10.1002/bit.25535.

[132] J.S. Edwards, R. Ramakrishna, B.O. Palsson, Characterizing the metabolic phenotype: A phenotype phase plane analysis, Biotechnol. Bioeng. 77 (2002) 27–36. doi:10.1002/bit.10047.

[133] K. Kits, Denitrification and the Hypoxic Response in Obligate Aerobic Methane-Oxidizing Bacteria, University of Alberta, 2016.

[134] D. van der Ha, B. Bundervoet, W. Verstraete, N. Boon, A sustainable, carbon neutral methane oxidation by a partnership of methane oxidizing communities and microalgae, Water Res. 45 (2011) 2845–2854. doi:10.1016/j.watres.2011.03.005.

[135] D. van der Ha, L. Nachtergaele, F.-M. Kerckhof, D. Rameiyanti, P. Bossier, W. Verstraete, N. Boon, Conversion of Biogas to Bioproducts by Algae and Methane Oxidizing Bacteria, Environ. Sci. Technol. 46 (2012) 13425–13431. doi:10.1021/es303929s.

[136] E.A. Hill, W.B. Chrisler, A.S. Beliaev, H.C. Bernstein, A flexible microbial co-culture platform for simultaneous utilization of methane and carbon dioxide from gas feedstocks, Bioresour. Technol. 228 (2017) 250–256. doi:10.1016/j.biortech.2016.12.111.

[137] K.A. Stone, D. Shah, M.H. Kim, N.R.M. Roberts, Q.P. He, J. Wang, A novel soft sensor approach for estimating individual biomass in mixed cultures, Biotechnol. Prog. 33 (2017) 347–354. doi:10.1002/btpr.2453.

[138] N.K. Dhami, M.S. Reddy, A. Mukherjee, Biomineralization of calcium carbonates and their engineered applications: a review, Front. Microbiol. 4 (2013). doi:10.3389/fmicb.2013.00314.

[139] V. Ivanov, J. Chu, V. Stabnikov, Basics of Construction Microbial Biotechnology, in: Biotechnol. Biomimetics Civ. Eng., Springer International Publishing, Cham, 2015: pp. 21–56. doi:10.1007/978-3-319-09287-4_2.

[140] M.S. Imbabi, C. Carrigan, S. McKenna, Trends and developments in green cement and concrete technology, Int. J. Sustain. Built Environ. 1 (2012) 194–216. doi:10.1016/j.ijsbe.2013.05.001.

[141] A.A. Raghoebarsing, A.J.P. Smolders, M.C. Schmid, W.I.C. Rijpstra, M. Wolters-Arts, J. Derksen, M.S.M. Jetten, S. Schouten, J.S. Sinninghe Damsté, L.P.M. Lamers, J.G.M. Roelofs, H.J.M. Op den Camp, M. Strous, Methanotrophic symbionts provide carbon for photosynthesis in peat bogs, Nature. 436 (2005) 1153–1156. doi:10.1038/nature03802.